Dynamic stall models applied to airfoils in deep stall

Martijn Steven Jorissen

Dynamic stall models applied to airfoils in deep stall

By

Martijn Steven Jorissen

Master of Science thesis

To obtain the degree of Master of Science
at the Delft University of Technology
to be defended on Monday May 8 2023

Student number: 4574869
Profile and track: Aerodynamics & Wind Energy, Aerodynamics
Supervisors: Dr. C. J. Simao Ferreira
Dr. G. J. Schepers
Dr. W. Yu

Acknowledgements

Despite most communication with my supervisors being online, I believe I have had an great team to support me in this work. I would like to firstly express my gratitude to Dr. Gerard Schepers. He has been an excellent supervisor during this thesis as well the internship preceding it. Additionally, I would like to thank him for providing me with the opportunity of this research project at TNO. Next, I would like to thank Dr. Wei Yu for her support and incredibly useful feedback throughout this project's many weekly meetings. Finally, Dr. Carlos Ferreira has been very helpful by providing new insight into my work every time I spoke to him.

Apart from my academic supervisors I have to show my appreciation for my friends and family who have been a tremendous support throughout this process. I especially want to thank my parents who have always provided a helping hand and a listening ear throughout the entirety of my studies. Without them I would never be where I am today. I am incredibly grateful for my aunt and uncle who have been nothing but supportive during my entire academic career. I also want to express my appreciation for Daan and our many conversations as roommates. These definitely have helped make my Master's as enjoyable as it has been. Finally, I would like to thank Echica, at whose kitchen table much of this report was written, for her continued words of support. They have been a great motivation in completing this project.

Abstract

Wind turbines experience a variety of different operating conditions during their operation. As a result, sections of their blades experience a range of angles of attack. Additionally, several commonly used modelling methods use the sectional loading of the blade directly. To adapt this sectional loading for higher angles of attack dynamic stall models are often used. However, these models are generally based in empirical results from pitching airfoils at moderate angles of attack. In this context moderate angles of attack are considered to be below 30 degrees. As a result, their applicability to stationary airfoils at much larger angles of attack is not known. Placing an airfoil at such angles causes it to enter deep stall conditions. During deep stall, vortex shedding becomes a dominant effect on the loading of the airfoil. This behaviour can greatly affect the loading on the turbine and thus should be modelled accurately.

Based on these observations, the presented work aims to investigate the applicability of current dynamic stall models to deep stall conditions. Additionally, an adapted dynamic stall models is created. This model was designed to improve the prediction of the vortex shedding frequencies for stationary airfoils in deep stall. In this process, three different experiments were used for comparison to experimental results.

Three previously developed dynamic stall models were considered, which all showed different responses in terms of vortex shedding. These responses ranged from being completely aperiodic to undamped oscillations. However, none of the models was able to accurately predict the vortex shedding frequencies of the considered experiments. Therefore, the current dynamic stall models were found not to be applicable to the deep stall regime.

Therefore, an adapted model was constructed and calibrated based on the experimental results. This model greatly improves the prediction of vortex shedding frequencies in all considered experiments. Additionally, the accuracy of this model when applied to pitching airfoils at moderate angles of attack was examined. When applied to those conditions the model performed only slightly worse compared to a reference dynamic stall model. Hence, the presented models shows promising results for extending current dynamic stall models to the deep stall conditions.

Finally, it should be noted that the general validity of the adapted model remains to be investigated further. For this purpose, more experiments are to be considered. However, the approach outlined in this research has been shown to provide good results for creating a dynamic stall model which includes vortex shedding in deep stall conditions. Therefore, the presented method can be used to develop a validated dynamic stall model for such conditions provided more experimental results are available.

Contents

Acknowledgements **i**

Abstract **ii**

List of Figures **vi**

List of Tables **ix**

1 Introduction **1**

2 Literature Review **3**
2.1 Aerodynamic models for turbine performance 3
2.1.1 Blade element method 3
2.1.2 Vortex Wake method 6
2.1.3 CFD simulations 8
2.2 Dynamic stall in airfoils 9
2.2.1 Typical dynamic stall behaviour 10
2.2.2 Vortex shedding 11
2.2.3 Necessity dynamic stall modelling 12
2.3 Overview of dynamic stall models 14
2.3.1 Beddoes-Leishman 14
2.3.2 ONERA 16
2.3.3 Snel 17
2.3.4 IAG adapted model 19
2.3.5 Overview of discussed models 20
2.4 Current state of research 21
2.4.1 Airfoil state-of-the-art 21
2.4.2 Turbine state-of-the-art 22
2.5 Research plan 23
2.5.1 Research plan 23
2.6 Optimisation of model parameters 25
2.6.1 Theoretical basis 25
2.6.2 UQLAB tool applications 26
2.6.3 Applicability in current research 26

3 Wind tunnel experiments for different airfoils and operating conditions 28
3.1 DNW-HPG experiment . . . 28
3.1.1 DNW-HPG experiment description . . . 28
3.1.2 Results of the DNW experiment . . . 30
3.1.3 Blockage effects of DNW experiment . . . 37
3.1.4 Initiation of vortex shedding . . . 40
3.2 TU Delft experiment . . . 41
3.2.1 TU Delft experiment description . . . 41
3.2.2 Results TU Delft experiment . . . 42
3.2.3 Blockage corrections TU Delft experiment . . . 43
3.3 NACA 4412 experiment . . . 45
3.3.1 Description of NACA 4412 experiment . . . 45
3.3.2 Results of the NACA 4412 experiment . . . 45
3.4 Comparison of all experiments . . . 47

4 Existing dynamic stall models for stationary airfoils in deep stall 49
4.1 Selected dynamic stall models . . . 49
4.2 Extraction frequencies . . . 50
4.3 Common dynamic stall models for stationary airfoils . . . 51
4.3.1 Vortex shedding predictions of the Snel model . . . 51
4.3.2 Vortex shedding predictions of the Adema model . . . 52
4.3.3 Vortex shedding prediction of the IAG model . . . 54
4.3.4 Effect of Reynolds number . . . 58

5 Development adapted model for vortex shedding frequencies 59
5.1 Adapted model for stationary airfoils . . . 59
5.1.1 Adapting definitions for deep stall angles . . . 59
5.1.2 Identifying potential adaptations of the model coefficients . . . 63
5.1.3 Adapting the Adema model . . . 63
5.1.4 Further considerations . . . 66
5.2 Time domain results . . . 67
5.2.1 Shedding results adapted model in time . . . 67
5.2.2 Time responses for reference pitching airfoil cases . . . 69
5.2.3 Adapting the vortex shedding model for pitching airfoil cases . . . 71
5.3 Performance adapted model . . . 74

6 Model calibration using uncertainty quantification tool 80
6.1 Sensitivity analysis . . . 80
6.2 Calibration procedure . . . 85
6.2.1 Surrogate modelling . . . 86
6.2.2 Calibration settings . . . 88
6.3 Calibration results individual experiments . . . 89
6.4 Final calibration . . . 94

7 Conclusions and recommendations 97

Appendices 102

A Other results DNW experiment **103**
A.1 Unsteady balance data analysis 103

B Verification dynamic stall models **108**
B.1 Original Snell model 108
B.2 Improved Snell model 109
B.3 IAG model 111

C Adapting the Adema model, an alternative option **114**

D CFD comparison for stationary airfoil **117**
D.1 CFD 117

Bibliography **120**

List of Figures

2.1 Annulus definitions for BEM method from Jenkins et al. [2001] 4
2.2 Angle definition for BEM method from Jenkins et al. [2001] 5
2.3 Shedding of vorticity from a blade from Jenkins et al. [2001] 7
2.4 Helical vortex shedding typical for the turbine wake from Jenkins et al. [2001] 8
2.5 Stages of dynamic stall from Khan [2018] 11

3.1 Overview of the wind tunnel layout used in the DNW experiment 29
3.2 Side view of the test section that is used in the DNW experiment 29
3.3 Location of the pressure taps placed on the DU00W212 airfoil used in the experiment 30
3.4 Airfoil polar from DNW experiment 31
3.5 Examples of unsteady and steady pressure distributions from measurements 32
3.6 Projected Strouhal numbers present for different angles of attack in both loading directions 33
3.7 FFT values for the different unsteady sensors at -51 degrees angle of attack . . 34
3.8 FFT values for the different unsteady sensors at 75 degrees angle of attack . . 35
3.9 FFT values for the different unsteady sensors at 31 degrees angle of attack . . 36
3.10 Frequency responses in both measurements 37
3.11 Selected projected Strouhal numbers based on discussed approach 38
3.12 Effect of different corrections on the projected Strouhal number 40
3.13 Base pressure coefficient variation from Fallahpour et al. [2022] 41
3.14 Base pressure coefficient variation from DNW experiment 42
3.15 Setup of the TU Delft experiment, Xu et al. [2023] 43
3.16 Frequency results of the TU Delft experiment, Xu et al. [2023] 44
3.17 Effect of blockage correction on the projected Strouhal number of the TU Delft experiment 44
3.18 Setup and measurement locations from Fallahpour et al. [2022] 46
3.19 Polar from NACA 4412 airfoil as found by Fallahpour et al. [2022] 46
3.20 Strouhal number resulting from the experiment described by Fallahpour et al. [2022] 47
3.21 Comparison of Strouhal number between experiments 48

4.1 Example of a damped response of the dynamic stall model, IAG model applied to a stationary DU-00-W-212 airfoil at -38 degrees 50

4.2 Effect of the window considered in the determination of the frequency response . . . 51
4.3 Frequency response Snel model compared to both experiments . . . 52
4.4 Time response comparison at 41 degrees of base Snel model and DNW experiment . . . 52
4.5 Frequency response Adema model compared to both experiments . . . 53
4.6 Time response comparison at 41 degrees of Adema model and DNW experiment . . . 53
4.7 Frequency response IAG model results compared to both experiments . . . 54
4.8 Different responses of the IAG model . . . 55
4.9 Frequency response IAG model results when only the first quarter of the signal is excluded . . . 56
4.10 Projected Strouhal numbers predicted by Adema model if absolute value is taken for $\Delta C_{L,pot}$ . . . 57
4.11 Effect of Reynolds number on the vortex shedding frequencies of the Adema model . . . 58

5.1 Comparison of steady polars to newly defined potential for both experiments 61
5.2 Effect of newly defined potential loading on shedding frequencies . . . 62
5.3 Shedding frequencies from the second option of the adapted model . . . 66
5.4 Comparison of shedding response of new model in time . . . 68
5.5 Adapted model response to OSU reference conditions . . . 70
5.6 Effect of new frequency term . . . 72
5.7 Adapted model response to OSU reference conditions . . . 73
5.8 Determination of critical and shedding angle for the NACA 4415 airfoil . . . 74
5.9 Error comparison of different model in terms of shedding frequencies . . . 75
5.10 Error comparison of different model for a moving S809 airfoil . . . 77
5.11 Error comparison of different model for a moving NACA 4415 airfoil . . . 78

6.1 Correlation coefficients for the DNW experiment using varying amounts of samples . . . 83
6.2 Sensitivity analysis comparison between experiments . . . 84
6.3 Convergence of the surrogate models for the DNW experiment . . . 87
6.4 Convergence of the surrogate models for the other experiments . . . 88
6.5 Calibration results for the DNW experiment . . . 90
6.6 Effect of calibration on DNW experiment . . . 90
6.7 Calibration results for the TU Delft experiment . . . 91
6.8 Effect of calibration on TU Delft experiment . . . 91
6.9 Calibration results for the NACA 4412 experiment . . . 92
6.10 Effect of calibration on NACA 4412 experiment . . . 92
6.11 Application of the combined calibration to all experiments . . . 95

A.1 Calibration matrix from DNW experiment . . . 103
A.2 Average voltage from each of the strain gauges . . . 104
A.3 Initial comparison of extract CL and CD . . . 105
A.4 Lift and drag coefficient . . . 105
A.5 Normal and tangential coefficient comparison . . . 106

A.6 Verification of the wind tunnel correction 107

B.1 Original Snell model verification 108
B.2 Variations of original Snell model around steady polar 109
B.3 Improved Snell model verification 109
B.4 Comparison of adapted Adema model to reference implementation 110
B.5 Comparison of the two versions of the Adema model to reference data (k = 0.0711 with a mean AoA of 18.4^o and a variation of 10.7^o) 111
B.6 Effect of increasing the inviscid lift curve slope 112
B.7 Comparison IAG implementation to reference 112
B.8 Comparison different time integration methods 113

C.1 Shedding frequencies from the first option of the adapted model 116

D.1 Simulated Strouhal number (circles) and projected Strouhal number (triangles) for the S809 airfoil, Pellegrino and Meskell [2013] 118
D.2 Comparison of the proposed dynamic stall model to CFD results from Pellegrino and Meskell [2013] 119

List of Tables

2.1 Overview of different dynamic stall models 21

5.1 Comparison of L_2 errors for the considered models in terms of predicting the shedding frequency 75
5.2 Comparison of L_2 errors for the considered models applied to a moving NACA 4415 airfoil 76
5.3 Operating conditions used for all references in OSU database 77

6.1 Description of parameters for sensitivity analysis 81
6.2 Settings for calibration procedure UQLAB 88
6.3 Description of prior used for the Bayesian inversion 89
6.4 MAP estimate for each of the experiments 93
6.5 Errors produced by different version of the adapted model 96

Chapter 1

Introduction

In recent years the market for wind turbines, especially large wind turbines, has grown significantly, Holierhoek et al. [2013]. Turbines tend to operate in unsteady environments and in a large variety of conditions, Leishman [2002]. Therefore, many different flow phenomena can be observed during their operation. One of these are vortex induced vibrations, which result from the periodic changes of the loading in time on a stalled turbine blade. This research in particular aims to focus on the vortex induced vibrations occurring in idling or standstill conditions, which have been observed by for example Stettner et al. [2016].

There are several methods available for modelling this behaviour. The first is to apply CFD to several operating conditions that are of interest and solve for the solution in time. This has been shown to provide reasonably accurate results in the past by Heinz et al. [2016]. However, this approach is computationally expensive and as a result is not applicable for design purposes, Khan [2018]. The alternative to CFD is to apply a dynamic stall model to commonly used, faster lifting line methods such as Blade Element Momentum models. Apart from this method, Vortex Wake models are also applied if more physically accurate results are required. These dynamic stall models modify the local loading coefficients that are used by the overarching models.

In the development of common dynamic stall models, wind tunnel experiments that use pitching airfoils at relatively moderate angles of attack are typically used. In this context moderate angles refers to angles below 30 at which vortex shedding is not generally present. As a result, the applicability to stationary surfaces at a high angle of attack, at which deep stall occurs, is not explored. In such cases, the airfoil can produce self-induced vortex shedding behaviour, which leads to an unsteady aerodynamic response even for a stationary airfoil. These conditions do occur in the life-cycle of wind turbines, for example during standstill or idling conditions. This can lead to excessive load excursions, Stettner et al. [2016]. Based on this, the first aim of this report is to examine the applicability of commonly used dynamic stall models for such conditions. In this report, the performance is examined in a two dimensional sense using airfoil experiments. Hence, a method is devised to compare the results of three different airfoil experiments to the response of three dynamic stall models.

The second objective of the currently presented research is to investigate potential improvements of the dynamic stall models for the discussed operating conditions. This objective is pursued through the experimental results from wind tunnel testing. Based on this

several adaptations are suggested. The suggested adaptations of the dynamic stall models are examined for a variety of operating conditions and airfoils in order to fully investigate the value of the proposed changes.

To accomplish the objectives described in this introduction the current literature is first reviewed in chapter 2. In this chapter the research plan is also outlined. Next, the experimental results that are available for the discussed conditions are described in chapter 3. After, the application of existing dynamic stall models to stationary airfoils in deep stall conditions is considered in chapter 4. Based on the observations made, an adapted dynamic stall model is presented in chapter 5. Next, in chapter 6, both a sensitivity study and calibration are performed on this model using the uncertainty quantification tool UQLAB. Finally, in chapter 7 the conclusions and recommendations for future work are presented.

Chapter 2

Literature Review

In this chapter the theoretical background required for this project is examined. Firstly, the models that are typically used to determine turbine performance are examined in section 2.1. Next, the phenomena that are the cause of these vortex-induced vibrations are examined in section 2.2. After which the commonly used methods for modelling this behaviour are discussed in section 2.3. Next, the experimental results from the past that are relevant for this research are discussed in section 2.4. This section also aims to develop the main research questions that result from the current state of the research on this topic. Following the research questions, section 2.5 defines the proposed method for answering these questions. In addition, it outlines the experiments that are to be used for the proposed project. Finally, the statistical method that could be used for the calibration of the model parameters is discussed in section 2.6.

2.1 Aerodynamic models for turbine performance

In order to provide insight in the general modelling of wind turbines, some of the models that are used in their simulation are explored first. This is done by showcasing the two most prevalent methods that are used in wind turbine design; the Blade Element Momentum (BEM) method and the Vortex Wake (VW) method. Both of these methods use the sectional loading on blade sections in their approach. Apart from these common methods, the effects of using CFD to discuss turbine performance relating to vortex induced vibrations is also briefly discussed.

2.1.1 Blade element method

The first simulation method that will be discussed is the Blade Element Momentum (BEM) method. This method aims to solve the loading distribution over a wind turbine by separating the flow tube through the turbine in radial and azimuthal directions. This discretizes both the turbine blades and the flow tube. For each of these sections, two perspectives are considered. Firstly, for each of these separate streamtubes, the conservation laws of mass and momentum are applied. Which results in a distribution of the induced velocity over the rotor. From the induced velocities and the free stream values the inflow angles at each section can be determined. Based on this, the second element of the method can be ap-

plied, which uses the discretisation of the blade. For each section the force coefficients are determined based on the airfoil characteristics and the local inflow angle. This step uses the steady polar of the local airfoil shape. Using the new loading in each streamtube, the conservation laws can be re-evaluated. This process is repeated until a steady solution is obtained. In this section the exact formulation of this method is outlined in more detail.

The first step of applying the BEM method to a rotor is to divide the streamtube associated with the rotor into multiple smaller streamtubes. It is assumed that each of these tubes is independent of the adjacent tubes. In order for this assumption to remain valid, the theory is usually applied in an axial flow case, where this assumption is more supported. However, it is also possible to apply this approach to yawed flow cases, Schepers [2012]. Additionally, models have been developed that allow for the inclusion of these yawed conditions by adapting the induced velocity as a result of the skewed wake, as is shown by Schepers [1999]. If the model is applied to these yawed conditions, the streamtubes are also separated in azimuthal direction. The discretisation of the streamtubes in axial case is shown in Figure 2.1.

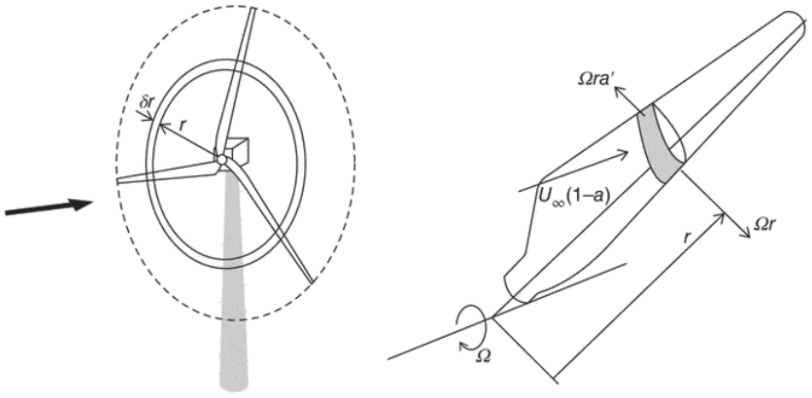

Figure 2.1: Annulus definitions for BEM method from Jenkins et al. [2001]

The next step in the process is to apply the conservation of mass and momentum to each of these streamtubes. In this step, the rotor plane is assumed to act as an actuator exacting a force of the flow. The equations that result from the application of the conservation laws are shown in Equation 2.1 and Equation 2.2. Based on the force applied by the rotor plane a decrease in velocity is expected at the rotor and in the wake of the turbine. The decrease is velocity in both of these locations is represented by the induction factor, which is defined as $a = \frac{u_{induced}}{V_\infty}$. The resulting velocities at the rotor and in the wake are shown in Equation 2.3.

$$\dot{m} = \rho A_\infty V_\infty = constant \tag{2.1}$$

$$(p_{front} - p_{rear}) A_D = (U_D - U_\infty)\dot{m} \tag{2.2}$$

$$U_{D,actuator} = (1-a)U_\infty \qquad U_{D,wake} = (1-2a)U_\infty \tag{2.3}$$

Having determined how the induced velocity from the turbine forces affects conservation equations, the actual loading on the rotor can be expressed as a function of this induction. This can be separated into two contributions, axial loading perpendicular to

the rotor plane and tangential loading to the rotor plane. Each of these contributions have their own induction factor. The resulting equations for the axial case at each annulus are shown in Equation 2.4 and Equation 2.5. From these equations, the performance parameters from the turbine can also be extracted. The definitions are shown in Equation 2.6 and Equation 2.7.

$$T = (p_{front} - p_{rear}) A_D = 2\rho A D U_\infty^2 a(1-a) \tag{2.4}$$

$$P = T U_D = 2\rho A D U_\infty^3 a(1-a)^2 \tag{2.5}$$

$$C_T = 4a(1-a) \tag{2.6}$$

$$C_P = 4a(1-a)^2 \tag{2.7}$$

Apart from the axial loading described above, the conservation laws can also be applied to consider the torque generated by the rotor. This is done by considering the induction factor for the azimuthal induced velocity, a'. This induction factor is defined as $a' = \frac{U_{azimuthal}}{r\Omega}$. From this definition the torque related to a small annulus can be obtained through the conservation of angular momentum. This process results in Equation 2.8.

$$\delta Q = r\delta\dot{m}(2r\Omega a') = 4\rho\pi r^3 U_\infty a'(1-a)\Omega\delta r \tag{2.8}$$

In the previous equations, the loading on the turbine is expressed from the perspective of the flow passing through the streamtubes. This definition focuses on the conservation laws and only considers the turbine as an actuator. To include the effects of the geometry of the turbine blade, the geometry is linked to the actuating force of the turbine. This can be done by assuming the loading on each blade section can be represented by the local lift and drag coefficients. The local lift and drag coefficients are obtained from the steady polars and the local inflow angle. The inflow angle is constructed from the free stream velocities, the rotation of the blade and the local induction factors. Since this part of the model considers the loading coefficients of an airfoil directly, this is where the link to dynamic stall models is integrated. The dynamic stall models are able to modify the local loading coefficients based on unsteady effects. These steps result in the loading as described in Equation 2.9 and Equation 2.10. The angle definitions that are used to obtain the sectional loading are shown in Figure 2.2.

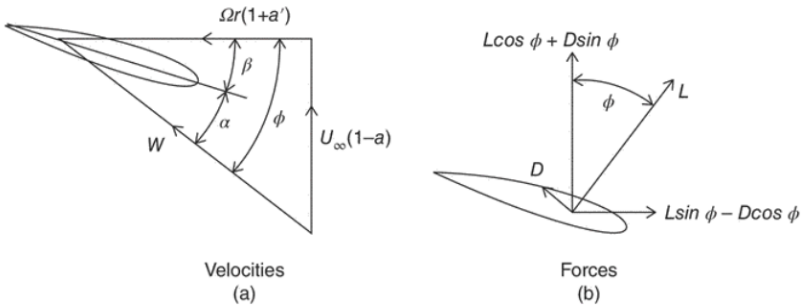

Figure 2.2: Angle definition for BEM method from Jenkins et al. [2001]

$$\delta T = \frac{1}{2}\rho W^2 Bc(C_l cos(\phi) + C_d sin(\phi))\delta r \tag{2.9}$$

$$\delta Q = \frac{1}{2}\rho W^2 Bcr(C_l sin(\phi) - C_d cos(\phi))\delta r \tag{2.10}$$

Having defined the loading from both the blade element and momentum perspective, the definitions can be equated as the same turbine loading is described. Based on which the final set of equations of this method can be constructed, Equation 2.11 and Equation 2.12. These equations are solved by applying iterations to find a converged value of the induced velocities.

$$\frac{W^2}{U_\infty^2} BcRC_x = 8\pi a(1-a)\mu \tag{2.11}$$

$$\frac{W^2}{U_\infty^2} BcRC_y = 8\pi\lambda a'(1-a)\mu^2 \tag{2.12}$$

In the described method several important limitations should be discussed. The first is the assumption that the streamtubes are independent, which was already mentioned. This assumption is not entirely true as different 3D effects can affect the flow on a wind turbine. Additionally, the method is not valid for heavily loaded rotors, as the flow would reverse in the wake as a result of such loading. However, a correction has been created for this, Glauert [1935]. Thirdly, is should be noted that the sectional loading coefficients use the 2D airfoil polar. This polar would be altered slightly by 3D effects present in the flow around a turbine. Additionally, it is important to note that the steady coefficients are used. The modifications for including dynamic loading are described at a later stage. Finally, a correction is introduced near the ends of the blade to account for the losses in these regions.

Finally, as discussed the BEM method does use the sectional lift coefficient for each section. Therefore, it is possible to apply the dynamic stall models that are outlined in this report to each of these values. This allows for direct integration of the described models, as these make use of a 2D lift coefficient.

2.1.2 Vortex Wake method

The BEM method is commonly used because it is able to provide results quickly and with reasonable accuracy. However, a lot of assumptions are made in the creation of the model. These assumptions limit the reliability and applicability of the model. Therefore, another approach is also often used, the Vortex Wake (VW) method. In this approach the shedding of vorticity is modelled explicitly based on the current estimate of the lift at each time step. The influence of this shed vorticity on the velocity field is then examined based on the Biot-Savart law, Equation 2.13. This law describes the influence of a vortex or filament of vorticity on the velocity at any point in space. Therefore, it can be used to compute the effect the shed vorticity has on the flow field at the rotor.

$$\bar{v}_i = \frac{\Gamma}{4\pi}\int \frac{d\bar{l}(\bar{r}_0 - \bar{r}_1)}{|\bar{r}_0 - \bar{r}_1|^3} \tag{2.13}$$

As discussed the VW method chooses the model the effect of the turbine on the incoming flow by considering the shed vorticity. This done by discretising the blades along their length. At each radial position, the inflow velocity is determined based on the inflow conditions, the rotor orientation and the effect of the previously shed vorticity. Having determined the inflow angle the loading on each section can be determined. Several methods can be used for this. The most simple approach is to use the steady lift polar of that section similarly to the BEM model. However, other methods could also be implemented, such as panel methods. The consideration of the local blade section is the area where dynamic stall models are implemented. Especially if the steady polar is used for the loading, the dynamic stall model is implemented similarly to the BEM model. For each time step, the change in loading determines how much vorticity is being shed by a specific section. As a result of this process, a sheet of vorticity is shed by each blade with varying strengths. This shedding can be depicted as in Figure 2.3.

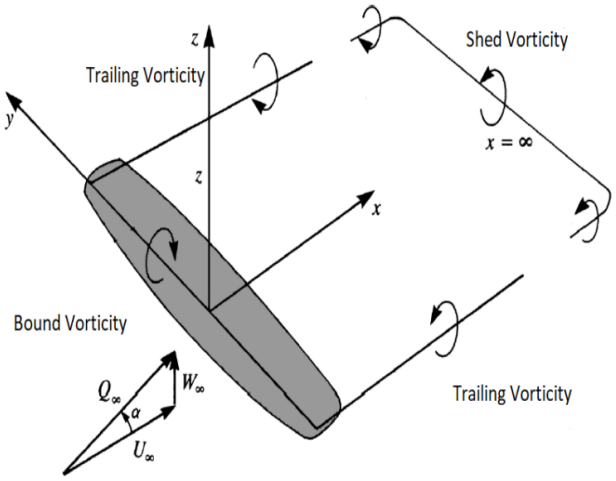

Figure 2.3: Shedding of vorticity from a blade from Jenkins et al. [2001]

The depiction of the vortex shedding as shown above is the effect of the vortex shedding from a single blade. However, in the VW method the blade is represented by small sections with bound vorticity. This results in each sectional shedding of vorticity as is shown in Figure 2.3. The shedding occurs according to the Helmholtz theorem, which states that the vortex filaments cannot start or end is space. As a result of this, a vortex sheet is created behind the rotor. In the VW model the vortex sheet also deforms based on the rotation of the rotor and therefore creates a helical pattern in the wake, Figure 2.4.

Since this method chooses to also model the wake and not just the rotor plane like the BEM method, the progression of the wake is important to consider. There are two options for the movement of the wake. This first option, the frozen wake, considers only the inflow conditions and the rotor geometry. As such, this method does not consider the effect of the shed vorticity on the movement of the wake. The second approach, the free wake, does consider this effect. This choice does increase the accuracy of the simulation, but greatly increases the computational cost required for each time step.

The choice to model the wake does eliminate a lot of the additional models that was

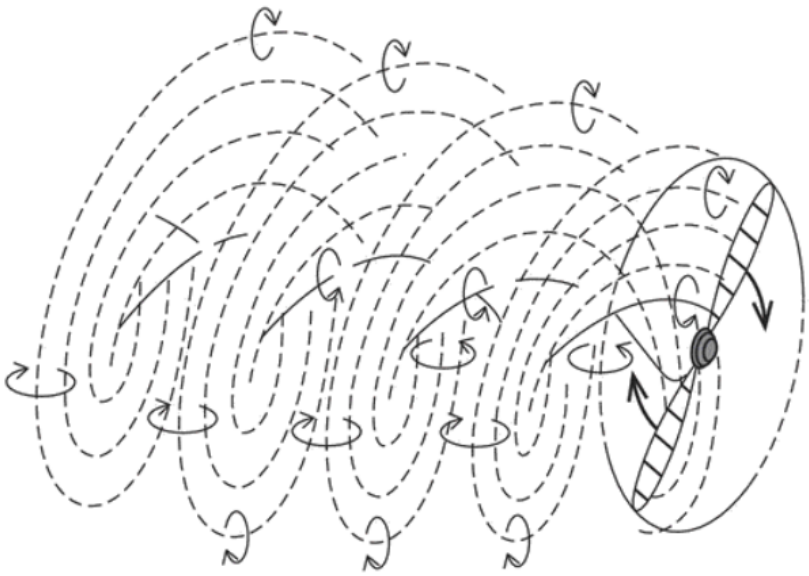

Figure 2.4: Helical vortex shedding typical for the turbine wake from Jenkins et al. [2001]

present in the BEM method, Hauptmann et al. [2014]. For example, the losses near the tip of the blades are now modelled intrinsically by the choice of model. As such, this model contains much less assumptions and corrections for specific conditions. Additionally, it will cover the prediction of the induction more accurately in general as the wake is actually modelled.

Finally, this method can use several methods to determine the local force coefficients. For example it is possible to link a panel method or simply use the steady lift coefficients. When the lift coefficients are considered, it is possible to simply implement the dynamic stall models to modify these. This results in a direct determination of the force coefficients of each section including an adaptation for the dynamic stall.

2.1.3 CFD simulations

In the previous two sections the models that are most commonly used to determine the loading on wind turbines are discussed. However, another option for modelling the aerodynamics of wind turbines is also available, namely Computational Fluid Dynamics (CFD). This method of simulation aims to solve a version of the Navier-Stokes equations numerically. These equations, Equation 2.14 and Equation 2.15, represent the conservation laws for mass and momentum. In the complete set of equations a conservation equation is also determined for the energy, however that equation tends to be used less in the simulation of wind turbines, Khan [2018].

$$\frac{\partial \rho}{\partial t} + \vec{\nabla} \cdot (\rho \vec{u}) = 0 \tag{2.14}$$

$$\frac{\partial \vec{u}}{\partial t} + (\vec{u} \cdot \vec{\nabla}) \vec{u} = -\frac{1}{\rho} \vec{\nabla} p + \vec{F} + \mu \rho \vec{\nabla}^2 \vec{u} \tag{2.15}$$

There are several different methods for solving these equations, that have varying degrees of accuracy and computational cost. Firstly, there is the most commonly used method, Reynolds Average Navier Stokes (RANS). This method only solves the time averaged solution directly and superimposes the effect of turbulence through a separate model. This method has been applied to solve for example the vortex induced vibrations present in a wind turbine blade by Heinz et al. [2016] or in the tower of a turbine by Viré et al. [2020].

A second, typically more accurate, method is that of Large Eddy Simulations (LES). This method chooses to not average the solution in time, but filter out the smaller scales relating to the structures in the flow. The idea being that these small scales are relatively independent on the flow structure. As such, they can be modelled more easily. Since this method resolves quite a large number of scales, the computational cost related to this approach is typically higher. This method has also been used to simulate wind turbine performance by Revaz and Porté-Agel [2021], as well as vortex induced vibrations by Horcas et al. [2020].

Finally, Direct Numerical Simulation (DES), chooses to neglect none of the scales present in the flow and instead refines the mesh sufficiently to resolve all scales. This does increase the computational cost dramatically causing it to only be applicable in a very small set of problems. Therefore, the application of this method on turbines is not a feasible option.

It should be noted that in order to solve these equations numerically, a significantly larger computational cost is associated with each simulation when compared to the previously discussed methods. This is the case regardless of the solution method chosen. Therefore, since multiple operating conditions and configurations are to be considered during the design, none of these methods is currently a suitable alternative to the models that have been presented in the previous sections.

The application of CFD is not required to simulate the entire turbine. It is possible to include simulations for parts of the problem. For example, the flow interaction with the blade can be simulated using CFD, but the not the induction. The inverse is also possible. As such, the use CFD can be applied to several areas. A similar distinction can be made to the one presented in the BEM approach, where the momentum and blade contributions are considered separately as well.

A final comment on alternative computational methods should be made. This being that another method that is sometimes used in wind turbine simulations, a vortex lattice method, is also not applicable. This method uses the Euler equations, which are inviscid versions of the Navier-Stokes, Jenkins et al. [2001]. As such, this model cannot be used as the problem of dynamic stall is highly viscous.

2.2 Dynamic stall in airfoils

The phenomena and effects occurring dynamically in a stalling airfoil have been extensively documented. Typically, these effects are considered to be a 2D phenomenon and as such airfoils are considered. The sectional loading of these airfoils is often used in the common models for wind turbines, as was shown in section 2.1. In this section a general description of typical dynamic stall behaviour is first provided. Next, the dynamic stall phenomena causing this behaviour are explored in more detail. Thirdly, the shedding of vorticity and the effect on the loading of airfoils is discussed. This topic is treated separately as it is relevant for the vortex induced vibrations considered in this research and is typically not included in the common dynamic stall models. Finally, some observations

from the considered research are used to establish the gaps in the knowledge for this topic.

2.2.1 Typical dynamic stall behaviour

The onset and behaviour of dynamic stall has been observed and documented quite some time ago by for example McCroskey [1981]. In this research the behaviour of the flow on a dynamically stalling airfoil is attributed mostly to the leading edge vortex that is generated. As a result of this behaviour, the maximum loading on the airfoil tends to be increased. This is accomplished by delaying the angle at which complete stall occurs. Additionally, the time required to return to the stationary lift curve is also increased as a result of the travelling vortex.

As was discussed, a main reason for the changes in loading is the leading edge vortex being created and travelling over the top of the stalling airfoil. During this process five stages can be identified, which are presented in Mulleners and Raffel [2011] and Leishman and Beddoes [1989]. An illustration of these stages is shown in Figure 2.5. During the first stage, the angle of attack is increased to the static stall angle. This causes the lift coefficient to follow the static value quite closely. Once the static stall angle is reached, some recirculation might be observed in the boundary layer near the leading edge. However, this does not greatly affect the loading. In the second stage, this zone of recirculation develops into a leading edge vortex (LEV), which starts to move separately from the airfoil. In the third stage, the LEV moves along the top surface of the airfoil, carrying an area of low pressure with it. This causes the lift to continue to rise. Additionally, the centre of pressure is moved towards the trailing edge. This change in the centre of pressure affects the moment coefficient significantly. Once the vortex leaves the airfoil, the fourth stage begins, lift stall. During this stage, the lift decreases rapidly as the flow becomes completely detached. The final stage is the reattachment of the flow, which occurs at a much lower angle of attack compared to the static lift curve. Once the angle of attack has been sufficiently reduced the flow is able to reattach front to back. During this process the loading gradually returns to the static lift curve, if given sufficient time and the angle of attack is sufficiently small.

To describe dynamically stalling airfoils, a distinction can be made between light stall and deep stall, McCroskey [1981] and Mulleners and Raffel [2011]. During light stall the airfoil remains relatively close to attached flow, periodically moving in and out of the stalled regime. Due to these relatively small angles of attack, the LEV tends to separate as the result of the airfoil motion at the end of an upstroke. This results in a smaller viscous zone on top of the airfoil where the dynamic effects are taking place. It should be noted that the light stall regime depends more significantly on airfoil geometry, motion, maximum angle of attack and other flow conditions such as the mach number. In the current research the mach number will not be sufficiently large to be a relevant consideration.

In the deep stall regime, the shedding of vortices is the dominant force. As a result the viscous layer is significantly larger. During deep stall the LEV tends to separate as a result of its growth during the upstroke and as such the separation occurs before the maximum angle of attack is reached. It should be noted that this regime of dynamic stall is most relevant for the situation that is considered in the research question. Additionally, the onset and behaviour of stall in this regime are much less dependent on the airfoil characteristics and the motion. This is promising for the modelling of such behaviour as the model parameters are less likely to be airfoil dependent in this regime.

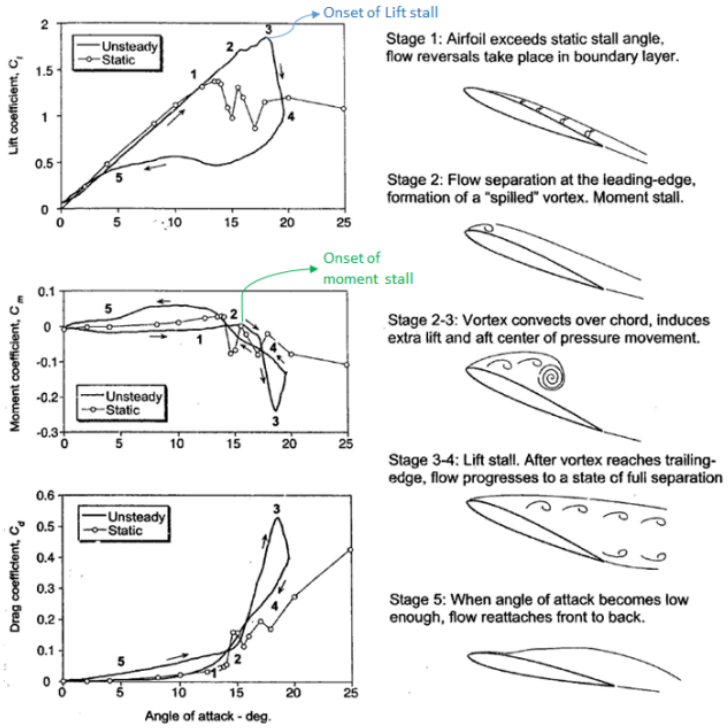

Figure 2.5: Stages of dynamic stall from Khan [2018]

2.2.2 Vortex shedding

As has been mentioned, the phenomenon of vortex shedding is a dominant forcing term in the deep stall regime. Therefore, the observed behaviour during this behaviour is to be considered as well in this section. It should be noted here that the dynamic stall models typically consider a single vortex being shed at the onset of stall. This vortex is the result of the changing between attached and detached flow conditions. However, when the angle of attack is increased further, the shedding of vorticity can continue. This phenomenon of continuous vortex shedding in deep stall conditions can be referred to as self-induced vortex shedding. The behaviour can be compared to the Von-Karman streets produced by blunt objects placed in a continuous flow. For this behaviour to become dominant the inflow angle typically is increased far beyond stall, Fallahpour et al. [2022]. Therefore, for the purpose of this report large inflow angles are considered to be those that place the airfoil in this deep stall condition. Typically, these values appear to be beyond 30 degrees.

The vortex shedding behaviour of airfoils is often analysed in the frequency domain by considering the dominant frequencies present in the loading. To analyse this domain, the Strouhal number of the vortex shedding, defined as in Equation 2.16, is often used. This equation transforms the frequency, f, into a non-dimensional quantity. This is done by using the velocity of the airflow, V, and the characteristic length, L. The characteristic length is defined as the length of the airfoil considered perpendicular to the flow direction. In Skrzypiński et al. [2014], CFD was performed to investigate the vortices being shed by a stationary airfoil placed at 90 degrees angle of attack under constant operating conditions. This was done for several different operating conditions. These different simulations resulted in a range of shedding frequencies. The Strouhal numbers representing the frequen-

cies ranged from 0.125 to 0.159 over the considered condition. Based on these simulations it was found that the oscillations could grow in magnitude for operating cases that were representative for wind turbine blades. On other simulations performed on airfoils, such as Pellegrino and Meskell [2013], the shedding of the vortices was found to be similar to the behaviour shown by bluff bodies. The shedding behaviour from these simulations resulted in Strouhal numbers ranging from 0.11 to 0.16 for different airfoils and operating conditions. Additionally, it was found that the angle of attack and orientation of the sharp trailing edges relative to the flow were of significant influence on the vortex shedding. However, the camber did not seem to affect the results, suggesting that these results could be applicable to other airfoil sections.

$$S_t = \frac{f \cdot L}{V} \tag{2.16}$$

Both of these studies used CFD as a tool to predict the loading of the airfoil, however other tools are also available. In Riziotis et al. [2010], a vortex model is used to simulate the vortex shedding of a stalled blade at large angles of attack in order to assess its stability. From this it was found that for certain inflow conditions, some of the modes of the blade would experience negative damping and as such be at risk of becoming unstable. The fact that these damping characteristics were incorrectly predicted using steady-state polars once again shows the importance of accurately simulating the loading created in such operating conditions.

Apart from simulation results of vortex shedding, some experimental results have also been produced. Firstly, wind tunnel experiments such as the one presented by Yon and Katz [1998], show that the disturbances created by the vortex shedding in the wake can be measured as unsteady pressure fluctuations. Additionally, this experiment observed Strouhal numbers in a very similar range to the ones obtained from the above mentioned simulations. The experiment used a different airfoil profile to the ones considered so far, suggesting these shedding frequencies to be a relatively constant phenomenon. It should be noted that at angles closer to the light stall regime, lower frequencies may also occur as the result of instabilities in the shear layer of the wing. However, these disappeared for deep stall conditions.

In addition to the wind tunnel measurement on wings, scaled turbine models have also be examined in term of their vortex shedding by Schreck [2007] and Khan et al. [2020]. In these experiments similar trends were observed in terms of the frequency of the shed vortices. There were a number of Strouhal numbers that were in the expected range for vortex shedding as has been defined. Additionally, these experiments also observed the lower Strouhal numbers which result from instabilities closer to the airfoil. In Khan et al. [2020], these are attributed to the switching between stalled and non-stalled state of the airfoil as a result of which the leading edge loading would vary.

2.2.3 Necessity dynamic stall modelling

The different types of behaviour that can be observed in stalling blades have been outlined in the previous sections. In this section the effects of this behaviour are explored further based on several additional investigations. The goal of this is to clarify the critical nature of the accurate modelling of stalling blades on the turbine performance.

Firstly, the stability of turbines in idling or standstill conditions is considered. In Wang et al. [2017], the stability of several modes related to an idling turbine were simulated using an aeroelasticity tool. From this it has been concluded that some of the modes related to the considered turbine do contain negative damping when simulated and as such are unstable. Similar results relating to the instability of certain modes in idling turbines were also found in Bir and Jonkman [2007]. Additionally, from the simulations presented there, the instability of these modes was larger when steady-state values of the polar were used. As such, changes in the implementation of the dynamic stall model can be critical in order to predict the stability. Another simulation shown in Chen et al. [2022] also showed that some of the modes of a wind turbine could become unstable given certain conditions during standstill. As has been shown in the research described above, instabilities of idling turbines are a real possibility and the selection of the sectional loading coefficients affects when they occur. Therefore, since these load cases can be important in the design, they should be accurately predicted.

Another reason that the prediction of dynamic stall is important for the loading on a turbine is examined in Liu et al. [2017]. There, the unsteady loading on a moving airfoil is simulated using CFD, showing the ability of the model to capture the variation of the loading with reasonable accuracy. Additionally, it is shown that the motion of an airfoil can also greatly affect the loading. Based on these conclusion the loading on a turbine is simulated both including and excluding the out-of-plane motion using a Blade Element Method (BEM). This showed that the inclusion of the vibration induced out-of-plane motion was greatly important to especially the fatigue loading of the turbine. Therefore, it can be concluded that the accurate prediction of these vibrations, in which dynamic stall can be play a large role, is also important for the fatigue life of turbines.

So far the importance of the prediction of dynamic stall for both fatigue and peak loading on wind turbines has been shown. Next, the influence of the dynamic stall models on these simulations should be considered. In Stettner et al. [2016], simulations are once again performed to examine the stability of a large idling wind turbine blade. These simulations resulted in some conditions leading to undamped oscillations similarly to previously outlined results. It should be noted that the inclusion of a dynamic stall model, the Beddoes-Leishman or ONERA model, typically increased the damping. This potentially leads to a more conservative solution. It was also found that including the rotation of the blade and as such introducing 3D effects also decreased the damping. However, when dynamic stall models were applied to the 3D results, the effects were similar to the stationary wing. Therefore, it can be concluded that the inclusion of a dynamic stall model is of great importance for the accurate prediction of the stability in turbine blades.

In addition to this conclusion, it was found that the selection of the dynamic stall model and the parameters within this model played a critical role in the stability of the structure. In fact, it was found that different structural dynamic, structural modelling choices as well as mode shapes had only secondary influences compared to the dynamic stall model. Based on this, and the overview presented in this section, it can be concluded that the selection of these models and their parameters is crucial for the design of wind turbines. Therefore, this research aims to explore the applicability of these models for higher inflow angles.

2.3 Overview of dynamic stall models

As was outlined in the previous section, the selection of the dynamic stall model and the parameters within such a model is important to the prediction of the loading on a wind turbine. Therefore, this section will explore some of the different dynamic stall models that are commonly used. The definitions of these models will be presented as well as their limitations relating to the operating conditions considered in this research.

2.3.1 Beddoes-Leishman

The first model that is discussed in the Beddoes-Leishman model, as originally defined by Leishman and Beddoes [1989]. This is still one the most commonly used models in practise. The model aims to use the separation of the different stall phases, as described in subsection 2.2.1. Each of these phases includes specific contributions that are meant to represent the flow phenomena occurring at that time.

During the first phase the flow remains attached to the airfoil. In the modelling, Theodorsens theory is used to model the time-delay in the loading response to changes in angle of attack. This response consist two parts, first a circulatory part, which results from the wake behaviour and includes the time-delay as shown in Equation 2.17. In these equations, b_1 and b_2 are the time-constants of the lag equations, with A_1 and A_2 being their respective coefficients. Time is also non-dimensionalised by introducing $S = \frac{2Vt}{C}$.

$$\begin{aligned} C_{N,n}^{C} &= C_{N,\alpha}(\alpha_{E,n} - \alpha_0) = C_{N,\alpha}(\alpha_n - X_n - Y_n - \alpha_0) \\ X_n &= X_{n-1}e^{-b_1\Delta S} + A_1\Delta\alpha_n e^{-b_1\frac{\Delta S}{2}} \\ Y_n &= Y_{n-1}e^{-b_2\Delta S} + A_2\Delta\alpha_n e^{-b_2\frac{\Delta S}{2}} \end{aligned} \tag{2.17}$$

Additionally, a non-circulatory contribution is added, which is the direct result of the movement of the airfoil itself. This creates an added mass as well as an impulse loading contribution, as shown in Equation 2.18. In those equations, D_n represents the deficiency function. The non-circulatory time-constant $T_I = \frac{c}{a}$ is used to examine the propagation time of disturbances over the airfoil. This time-constant is multiplied by a factor K_α, which depends on mach number as described by Leishman and Beddoes [1989]. The combination of $C_{N,n}^{C}$ and $C_{N,n}^{I}$ is used to find the total force coefficient on the airfoil.

$$\begin{aligned} C_{N,n}^{I} &= \frac{4K\alpha c}{V}\left(\frac{\Delta\alpha}{\Delta t} - D_n\right) \\ D_n &= D_{n-1}e^{\frac{-\Delta t}{K_\alpha T_I}} + \frac{\Delta\alpha_n - \Delta\alpha_{n-1}}{\Delta t}e^{\frac{-\Delta t}{2K_\alpha T_I}} \end{aligned} \tag{2.18}$$

The second phase contained within this model relates to the trailing-edge separation. This module is meant to express the non-linear effects occurring during flow separation using Kirchhoff's theory with a dimensionless parameter f. This parameter f represents the effective separation point, which can be obtained from the experimental static loading curve as explained by Gupta and Leishman [2006]. To accurately accomplish this the pressure and viscous lag are also modelled to represent the time delay caused during the flow

separation. The definition of the loading is based on unsteady static loading coefficient shown in Equation 2.19 from Kirchhoff's theory. This equation can be altered to be valid at larger angles of attack, Gupta and Leishman [2006]. For that purpose the small angle assumption has to be removed by taking the sine of the angle of attack instead.

$$C_N = C_{N,\alpha}\left(\frac{1+\sqrt{f}}{2}\right)^2(\alpha-\alpha_0) \tag{2.19}$$

Based on the equation above, the parameter f can be expressed as a function of the static loading and angle of attack. However, the stalling process is a dynamic process and therefore the coefficient must be adapted. The pressure lag is incorporated by applying Equation 2.20. In these equations, the time constant T_p depends on the mach number, but not on the shape of the airfoil.

$$\begin{aligned} C'_{N,n} &= C^P_{N,n} - D^P_{N,n} \\ D_{p,n} &= D_{p,n-1}e^{-\frac{\Delta S}{T_p}} + \left(C^P_{N,n} - C^P_{N,n-1}\right)e^{-\frac{\Delta S}{2T_p}} \end{aligned} \tag{2.20}$$

Based on this new lagged definition of the loading, a new effective angle of attack can be found. From this the effective separation point is found from experimental data. Having applied the pressure lag, the only step that remains in this module is to apply the viscous lag as well. This is done in a similar way as the pressure lag. The equation is shown by Equation 2.21. However, in this case the time constant T_f does depend on the airfoil shape in a significant way.

$$\begin{aligned} f''_n &= f'_n - D_{f,n} \\ D_{f,n} &= D_{f,n-1}e^{-\frac{\Delta S}{T_f}} + \left(f'_n - f'_{n-1}\right)e^{-\frac{\Delta S}{2T_f}} \end{aligned} \tag{2.21}$$

These steps finally combine in the adapted dynamic loading coefficient during trailing-edge stall. This is done by once again applying Equation 2.19 to the newly obtained effective separation point. The resulting equation is shown in Equation 2.22.

$$C_N = C_{N,\alpha}\left(\frac{1+\sqrt{f''}}{2}\right)^2(\alpha_{E,n}-\alpha_0) + C^I_{N,n} \tag{2.22}$$

The final two stages of the model relate to the computation of the onset of dynamic stall and the loading induced by the phenomena. Firstly, the onset is governed by the leading-edge separation module. As has been discussed, during the onset of dynamic stall a leading edge vortex is created and convected over the top surface of an airfoil. To determine at which moment this occurs, the non-dimensional vortex time parameter is introduced. This parameter is updated based on the normal loading, which is directly related to the leading edge pressure. The vortex time parameter is used to represent the location of the vortex that is being shed and as such represent the dynamic stall process. The update conditions are shown in Equation 2.23.

$$\tau_{v,n} = \begin{cases} \tau_{v,n-1} + \frac{0.45V2\Delta t}{c} & \text{if } C'_N > C_N \\ 0 & \text{if } C'_N < C_N \text{ and } \Delta\alpha_n > 0 \end{cases} \tag{2.23}$$

Having determined the location of the leading-edge vortex, the effect on the loading has to be considered. As described in subsection 2.2.1, the vortex carries an area of low pressure, which affects the loading. The vortex lift module of the Beddoes-Leishman models this through the increment shown in Equation 2.24.

$$C_{v,n} = C^{C}_{N,n}(1 - K_{N,n}) \tag{2.24}$$
$$K_{N,n} = \left(\frac{1+\sqrt{f''}}{2}\right)^2$$

As the vortex convects over the top of the airfoil, the loading decays. This continues until the vortex leaves the surface. Additionally, before the vortex separates the loading is not affected significantly, Khan [2018]. Therefore, no changes to the loading are computed as a result before this stage. To model the decay and convection of the vortex Equation 2.25 is used. In these equations, T_{vl} represents the time when the vortex leaves the airfoil. Similarly to the previous equations, T_v is a time constant. In this case T_v is slightly dependent on the airfoil shape and is obtained from experimental data. This loading contribution is added to the force coefficient in order to obtain the vortex loading.

$$C^{v}_{N,n} = \begin{cases} C^{v}_{N,n-1} e^{-\frac{\Delta S}{T_v}} + \left(C_{v,n} - C_{v,n-1}\right) e^{-\frac{\Delta S}{2T_v}} & \text{if } 0<\tau_{v,n}<T_{vl} \\ C^{v}_{N,n-1} e^{-\frac{\Delta S}{T_v}} & \text{else} \end{cases} \tag{2.25}$$

In this subsection, the four different modules of the Beddoes-Leishman model have been described. Each of the sections represents a different flow regime with different parameters as was discussed. However, some of these parameters do depend on airfoil data and as such should be calibrated for each airfoil specifically. Additionally, it should be noted that this model was originally developed for rotorcraft applications. It has been adapted to perform or wind turbines and their operating conditions as shown by Gupta and Leishman [2006]. However, as there is no explicit method for modelling the vortex shedding in a continuous sense. The vortex being shed during the final phase is a singular vortex and the effect on the loading would not be repeated without varying the inflow conditions. Thus, no higher order effects can be modelled using this approach. Therefore, the application of the model to the considered problem seems unattainable.

2.3.2 ONERA

The second model that will be discussed is the ONERA model, defined by Tran and Petot [1980] and Mcalister et al. [1984]. The ONERA model was later adapted by Peters [1985] to include higher angles of attack. This model introduces two differential equations to model the loading effects induced by the dynamic stall process. The first of these equations is meant to model the inviscid effects that occur. The second serves to model the viscous behaviour. Therefore, this model has the potential to model the second order effect that is vortex shedding. These equations are shown in Equation 2.26 and Equation 2.27.

$$\dot{C_{l,1}} + \lambda_L C_{l,1} = \lambda_L C_{l,pot} + (\lambda_L + \sigma_L)\dot{\alpha} + s_L\ddot{\alpha} \tag{2.26}$$
$$\ddot{C_{l,2}} + a_L\dot{C_{l,2}} + r_L C_{l,2} = -(r_L\Delta C_l + e_L\Delta\dot{C_l}) \tag{2.27}$$

In the equations above, there are many coefficients that have to be defined. The values of λ_L, σ_L and s_L depend on the angle of attack and the airfoil. They have to be obtained from wind tunnel measurements. The other parameters have definitions as shown in Equation 2.28 to Equation 2.30. These definitions also contain a large number of model parameters that all depend highly on the shape of the airfoil and as such have to be obtained from measurements. The value of ΔC_l is defined as the difference between the potential flow lift coefficient and the lift coefficient obtained from static airfoil polars. This works as a forcing term for the stalled regime as can be seen in Equation 2.27.

$$r_L = \left(r_0 + r_2 \Delta C_l^2\right)^2 \tag{2.28}$$

$$a_L = a_0 + a_2 \Delta C_l^2 \tag{2.29}$$

$$e_L = e_2 \Delta C_l^2 \tag{2.30}$$

From the description of the model, it is clear that this model requires a larger number of parameters to be determined separately before it can be applied. These parameters all require experimental data from an airfoil and as such limit the applicability for this model. However, if no data is available it is possible to use the "mean airfoil", Holierhoek et al. [2013]. Finally, it can be noted that the implementation of higher order differential equations allows for a method to model the unsteady behaviour that occurs beyond stall. In this case this is done by the forcing term of the second equation including a term based on the lift coefficient. Therefore, the forcing is non-zero even for a stationary airfoil. The shape of response to this forcing will depend highly on the value of the coefficients on the left side of the equation. The possibility of modelling these higher order effects is required for the application to the considered conditions in this research.

2.3.3 Snel

The third model that is outlined in this report is the Snel dynamic stall model, originally defined by Truong [1993b]. This model also applies two differential equations. These equations are used to model both the lower and higher order effects occurring during dynamic stall. Both differential equations produce an additional lift term which can be added to the steady value in order to obtain a new estimate of the lift coefficient. However, this model is does not contain as many parameters that depend specifically on the considered airfoil. The equations are shown in Equation 2.31 and Equation 2.32.

$$\tau \frac{d\Delta C_{l,1}}{dt} + cf_{10} \Delta C_{l,1} = ft_1 \tag{2.31}$$

$$\tau^2 \frac{d^2 \Delta C_{l,2}}{dt^2} + cf_{21} \frac{d\Delta C_{l,2}}{dt} + cf_{20} \Delta C_{l,2} = ft_2 \tag{2.32}$$

These equations once again introduce a number of new variables. Firstly, the first order equation is examined. In these equations τ is a time constant describing the time required for the flow to travel across a semi-chord. Its value is given by $\frac{c}{2V}$. Additionally, the coefficients ft_1 and cf_{10} are time dependent, where ft_1 represents the forcing as given by Equation 2.33. The coefficient cf_{10} is described by Equation 2.34. In this equation, the

value of E is set to 80 on the upstroke and 60 on the downstroke as increased stiffness is expected on the downstroke, Holierhoek et al. [2013].

$$ft_1 = \tau \frac{d\Delta C_{l,pot}}{dt} \tag{2.33}$$

$$\Delta C_{l,pot} = 2\pi sin(\alpha - \alpha_0) - C_{l,steady}$$

$$cf_{10} = \frac{1 + 0.5\Delta C_{l,pot}}{8(1 + E\tau \frac{d\alpha}{dt})} \tag{2.34}$$

The second equation, Equation 2.32, introduced two coefficients in the differential equation and one forcing term. The forcing term of this equation is represented by Equation 2.35. The other coefficients present in the differential equation are shown by Equation 2.36 and Equation 2.37. In these equations the parameter k_s is defined as the Strouhal frequency in uniform flow in deep stall conditions. This parameters typically has values between 0.17 and 0.2, Khan [2018]. Similar values were also observed in experiments and simulations of airfoils showing vortex shedding behaviour in subsection 2.2.2. From the definition of the damping shown in Equation 2.37, it is clear that a different type of damping definition is used in this method. This type of damping is referred to as a van der Pol type damping. Van der Pol oscillators are a non-linear system that include the square of the considered variable in the damping term of the differential equation.

$$ft_2 = 0.1k_s \left(-0.15\Delta C_{l,pot} + 0.05 \frac{d\Delta C_{l,pot}}{dt} \right) \tag{2.35}$$

$$cf_{20} = k_s^2 \left(1 + 3\Delta C_{l,2}^2\right) \left(1 + 3\left[\frac{d\alpha}{dt}\right]^2\right) \tag{2.36}$$

$$cf_{21} = \begin{cases} 60\tau k_s \left(-0.01(\Delta C_{l,pot} - 0.5) + 2\Delta C_{l,2}^2 \right) & \text{if } \frac{d\alpha}{dt} \geq 0 \\ 2\tau k_s & \text{if } \frac{d\alpha}{dt} < 0 \end{cases} \tag{2.37}$$

As discussed in the provided description, this dynamic stall model does not require many airfoil specific parameters to be used. As such, it can be implemented much more easily compared to the ONERA model. Additionally, the model contains the higher order dynamics that required within the second order differential equation. These are required to include the vortex shedding considered in this research.

However, in recent years some improvements have been made to the original formulation of the model as presented by Adema et al. [2020]. The first of these improvements is to apply the equations to the normal force coefficient instead of the lift coefficient. This, combined with the choice to use the specific normal force coefficient curve instead of the 2π value generally found for attached flow, improved the results of the model. Additionally, some of the model parameters are adjusted in their definitions. The first parameter that is adjusted is the k_s value, for which the projected value is used. This introduces a direct dependency of the shedding frequency on the angle of attack. Secondly, the first order parameter is adjusted according to Equation 2.38.

$$cf_{10} = \begin{cases} \frac{1+0.2\Delta C_{l,inv}}{8(1+60\tau \frac{d\alpha}{dt})} & \text{if } \frac{d\alpha}{dt} C_{N,inv} \leq 0 \\ \frac{1+0.2\Delta C_{l,inv}}{8(1+80\tau \frac{d\alpha}{dt})} & \text{if } \frac{d\alpha}{dt} C_{N,inv} > 0 \end{cases} \tag{2.38}$$

The second order parameters were also adapted as shown by comparing Equation 2.39 to Equation 2.41 with the previously presented equations in Equation 2.35 to Equation 2.37. In these updates it is clear that most of the adaptations relate to changing the values of certain parameters in the coefficients. This was done to improve the performance based on a number of references cases using pitching airfoils in wind tunnel experiments. Additionally, the parameter τ is included in the second order equation more in order to eliminate the dependency on the velocity.

$$f t_2 = 0.01 k_s \left(-0.04 \Delta C_{l,pot} + 1.5 \tau \frac{d \Delta C_{l,pot}}{dt} \right) \tag{2.39}$$

$$c f_{20} = 10 (k_s sin(\alpha))^2 \left(1 + 3 \Delta C_{l,2}^2 \right) \left(1 + 280^2 \tau^2 \left[\frac{d\alpha}{dt} \right]^2 \right) \tag{2.40}$$

$$c f_{21} = \begin{cases} 60 \tau k_s \left(-0.01 (\Delta C_{l,pot} - 0.5) + 2 \Delta C_{l,2}^2 \right) & \text{if } \frac{d\alpha}{dt} > 0 \\ 60 \tau k_s \left(-0.01 (\Delta C_{l,pot} - 0.5) + 14 \Delta C_{l,2}^2 \right) & \text{if } \frac{d\alpha}{dt} \leq 0 \end{cases} \tag{2.41}$$

2.3.4 IAG adapted model

The final model that is discussed in this literature review is the recently developed model presented by Bangga et al. [2020]. This model also adapts the dynamic response with a first and second order term similarly to the previously presented models. The first correction is based on the Beddoes-Leishman model with several adaptations. These adaptations relate to the moment and drag force coefficients that can also be obtained from the Beddoes-Leishman model. Up to this point only lift is considered in the descriptions. In the adaptation of the drag force the second phase of the model simply uses a time-lagged version of the static drag coefficient. This in combination with a correction, which eliminates drag hysteresis for relatively low angles of attack, was shown to improve the results significantly. The considerations for the moment coefficient are not discussed here. These are not expected to be as relevant for the purposes of this research as most considered experimental data does not provide a moment coefficient.

The second correction is meant to include the unsteady effects and as such is similar to the one presented by Truong [1993b] and Adema et al. [2020]. However, there are some alterations and selections that are made. The first choice is to differentiate with respect to S instead of time directly. The parameter S was introduced in the Beddoes-Leishman model and is defined as $S = \frac{2Vt}{C}$. This is also done in the application of the ONERA model to non-dimensionalise the equations. The second choice that is made, is the selection of the non-projected value for k_s used in the original definition of the Snel model. This decision was made as some instabilities were introduced by using the projected value. Additionally, some of the coefficients were altered as shown in Equation 2.42.

$$c f_{20} = 20 k_s^2 \left(1 + 3 \Delta C_{l,2}^2 \right) \left(1 + 3 \left[\frac{d\alpha}{dt} \right]^2 \right) \tag{2.42}$$

For the second coefficient the same formulation as presented by Adema et al. [2020] is used. Although the coefficient values are once again adjusted. For this coefficient, the newly found values are shown by Equation 2.43.

$$cf_{21} = \begin{cases} 150k_s\left(-0.01(\Delta C_{l,pot} - 0.5) + 2\Delta C_{l,2}^2\right) & \text{if } \frac{d\alpha}{dt} > 0 \\ 30k_s\left(-0.01(\Delta C_{l,pot} - 0.5) + 14\Delta C_{l,2}^2\right) & \text{if } \frac{d\alpha}{dt} \leq 0 \text{ and } \alpha \geq \alpha^{crit} \\ 0.2k_s & \text{if } \frac{d\alpha}{dt} \leq 0 \text{ and } \alpha < \alpha^{crit} \end{cases} \tag{2.43}$$

Finally, the forcing is adapted from the original Snel model, Truong [1993b]. Once again the exact values are slightly adjusted as is shown by Equation 2.44.

$$f t_2 = 0.5k_s\left(-0.15\Delta C_{l,pot} + 0.05\frac{d\Delta C_{l,pot}}{dt}\right) \tag{2.44}$$

For the other loading parameters, drag and moment, two different approaches are taken. The drag is obtained in a similar manner as described by Adema et al. [2020]. The moment however aims to use the idealised center of pressure location from the Beddoes-Leishman model. This results in a moment definition as is shown by Equation 2.45, where the normal and moment coefficients all relate only to the effect of the second order correction.

$$\Delta C_m = -C_{p,v}\Delta C_N \tag{2.45}$$

2.3.5 Overview of discussed models

In the previous sections, the theoretical definitions of several dynamic stall models have been described. Based on these descriptions, the theoretical advantages and disadvantages can be assessed together with their ability to be applied to the problem of vortex shedding in airfoils.

Firstly, the Beddoes-Leishman model is the only model unable to model the higher order dynamic directly. All other models contain a second order differential equation to be able to model higher order effects. Therefore, this model is never able to include the vortex shedding behaviour considered in this research.

A second consideration is the number of airfoil specific parameters. Having a large number of these parameters means that more experimental data for the used airfoil is required. This can be especially problematic when turbine blades are considered, as these often contain multiple different airfoil profiles over their span. As a result, the model parameters would be hard to determine for intermediate sections. As was discussed in the sections above, the Snel model has the least airfoil specific parameters, and as such is able to be applied most generally. The ONERA model has the largest number, as the determination of all coefficients in the differential equations rely on airfoil specific parameters. The Beddoes-Leishman model has some parameters that are specific to an airfoil profile, but significantly less compared to the ONERA model despite having more overall parameters. Finally, the IAG model also has a critical angle of attack which depends on the airfoil. However, in this discussion it should be noted that the numerical values used in the equations are often varied based on new calibrations. Therefore, the use of a different airfoil or measurement can also affect their values. Since these parameters are not specifically stated to be airfoil depended, these are not considered in Table 2.1.

The final consideration is the number of loading coefficients that are determined by the different models. This depends on the applied method and the choices made. For example, the Snel model was extended by Adema et al. [2020] to also include the drag coefficient.

An overview of all the considerations is provided in Table 2.1. This table shows that in order to model the second order effects any model other than the Beddoes-Leishman is possible. Additionally, the Snel based models have less model parameters that have to be determined from experimental data. Finally, it is shown that most of the models are able to predict all required loading coefficients.

Table 2.1: Overview of different dynamic stall models

Model	Highest order effect	Number of airfoil specific parameters	Coefficients modelled
Beddoes-Leishman	First	2	Cl, Cd, Cm
ONERA	Second	8	Cl, Cd, Cm
Snel	Second	None	Cl, Cd (Adema et al. [2020])
IAG	Second	1	Cl, Cd, Cm

The performance of different dynamic stall models has also been examined by for example Holierhoek et al. [2013]. From this comparison it was concluded that there was no strong preference for any of the models. However, this research did not contain the model presented by Adema et al. [2020] and Bangga et al. [2020].

2.4 Current state of research

In this section the current state-of-the-art experimental and simulation research relevant to the current research topic is explored. The goal of this process is to evaluate the relevant area of research and what questions are to be answered. As a result the main research questions are developed in this section. The current state of research is examined for airfoils and higher dimensional cases separately.

2.4.1 Airfoil state-of-the-art

In section 2.2 several experimental and simulation results have already been discussed to outline the expected behaviour during dynamic stall. This section aims to provide an overview of the conclusions that were reached, to provide context for the questions that the current research aims to answer.

In the experiments related to the dynamic stall behaviour, the goal is typically to measure the changes in loading in time. This can be used to determine effect of the changing pressure distribution on the airfoil. Additionally, if any periodic effects such as vortex shedding are to be investigated, this is also possible from this data. An example of this is the experimental data used in Adema et al. [2020]. This was obtained from the OSU database is used to examine both the shedding frequency of the airfoil, as well as the time-dependent loading. To compare the loading in the time domain, the phase of the simulation is shifted in order to match the phase of the measurement.

Additionally, some experiments are performed with the goal to understand the reasons for the changes in loading. These experiments are more interested in the flow field and can use techniques such as Particle Image Velocimetry (PIV) to visualise this. An example of

this is described by Henne et al. [2018], which investigated the effects the formation and release of the LEV had on the loading of an airfoil. This resulted in the conclusion that the strength of the LEV determines the maximum of the lift coefficient that is experienced during the dynamic stall cycle described previously. Therefore, this process is critical in producing an accurate model for the loading of an airfoil in dynamic stall conditions.

Apart from experiments, simulations can also be used in the investigation of dynamic stall behaviour. These simulations can use a variety of approaches to model the behaviour. The shedding of vorticity from a stationary airfoil is often done using CFD, examples of which are shown in Zakaria et al. [2018] and Pellegrino and Meskell [2013]. With such approaches the shedding of vorticity in time can be modelled, however the computational cost is relatively high. Other methods, such as the vortex method shown in Riziotis et al. [2010], are also available for predicting vortex shedding behaviour at a lower cost.

All these simulation methods are able to provide the user with a loading variation in time. This can be used to compare to experimental results in terms of loading and well as shedding frequencies. From this it is found that the prediction of the dominant shedding frequencies produces similar results in terms of Strouhal numbers for different cases. In each case the range of 0.15 to 0.2 is present in the Strouhal numbers that are obtained. Additionally, Adema et al. [2020], showed that the dominant frequencies present in the loading of a pitching airfoil in constant operating conditions could be predicted with reasonable accuracy using the presented version of the Snel model.

At this point it is important to highlight that most of the research into dynamic stall models focuses on moving airfoil sections. The vortex shedding of stationary airfoils might be considered, but this is not typically done using the dynamic stall models used in turbine codes. A possible reason for this is the fact that these models were developed by considering experiments with varying angles of attack. In fact, when vortex shedding during a stationary condition is considered, some parts of the equation are eliminated. Therefore, the effectiveness of applying current dynamic stall models to a stationary airfoil in deep stall conditions is unknown. This gap in current research does lead to the first main research question; How accurately can the current dynamic stall models be used predict the unsteady loading on a stationary airfoil in deep stall?

After investigating the applicability of the current dynamic stall models to stationary airfoils, an additional question can be considered. This question pertains to the improvement of these current dynamic stall models for this specific conditions. As the models have yet to be applied to these conditions, it is expected that some improvement would be possible based on comparison to experiments. This results in the second main research question; To what extend is it possible to improve the performance of the dynamic stall models for predicting vortex shedding behaviour in 2D, stationary airfoil modelling?

2.4.2 Turbine state-of-the-art

Due to the large scale of full-size turbines, there is no experimental research available for the large structure as far as the writer is aware. However, there are some wind tunnel experiments that aim to analyse the performance of dynamic stall models on scaled, stationary turbines. An example of such an experiment is the New Mexico experiment used in Adema et al. [2020] and Khan et al. [2020]. In the first, the differences between the Snel model and the stationary turbine model loading was found to be quite significant. These discrep-

ancies are attributed to the assumed damping coefficient of the turbine model as well as the unknown impact of different airfoils present in the blade. Additionally, the tunnel effects could not be taken into account in the software used for the simulation. Despite not finding a strong convergence between the model results and the experimental values, this comparison does showcase how an experiment could be compared to simulations for a turbine application.

In Khan et al. [2020], the modelling of the turbine is not considered. Instead the focus is placed on the analysis of the same experimental results. From this, a range of shedding frequencies is identified for the stationary turbine model at different yaw and pitch angles. The variation in shedding frequencies, which was also discussed in section 2.2, is something that will also have to be considered in the analysis of the current research. In Schreck [2007] the shedding frequencies for a rotating turbine are evaluated from the NASA Ames wind tunnel experiment. In both experiments the loading at several sections was identified using pressure taps. Despite using different rotors, two similar ranges of Strouhal numbers were identified as dominant frequencies. The first of these ranges varying from 0.12 or 0.15 to 0.2 depending on the paper. These frequencies are found to be related to the bluff body vortex shedding behaviour that was also identified in the airfoils. The second range, related to the more inboard sections in both cases, is located at Strouhal numbers of around 0.04. This range is expected to be the result of a post-stall regime in which switching between attached and stalled conditions is taking place. The fact that both these different experiments were able to identify similar ranges in Strouhal numbers does mean that similar results should be expected from the models to be deemed accurate.

Based on the available research, the current dynamic stall models have not been applied for stationary turbine simulations. This is to be expected as their applicability for airfoils has yet to be investigated. However, the next step after that validation would be to explore the usage for the purpose of turbine modelling. Unfortunately this area of investigation could not be contained within the scope of the current research. Therefore, this aspect is merely identified as a topic of future research. This research would aim to answer very similar research questions to the ones discussed in the previous section. The main exception would be the application to higher dimensional systems instead of airfoils.

2.5 Research plan

This section aims to formulate a plan to address some of the gaps in the research that were outlined in the previous section. To accomplish this, the necessary steps are discussed and combined into a research plan.

2.5.1 Research plan

Based on the main research questions discussed in the previous section, there are several considerations to be made to answer these questions. The first is the methods that could be used to assess the performance of the models that are implemented. There have been many different studies comparing the results of the dynamic stall models to experimental results. This is typically done by considering the loading on an airfoil in time for a range of angles of attack. In this project the airfoil angle of attack is kept stationary and the dynamic effects resulting from deep stall are considered. However, the method for comparing the results to

the experiment can be applied in a very similar way. This is mostly done by comparing the time domain loading from the experiment directly to the simulation results, as is done in Holierhoek et al. [2013] and Bangga et al. [2020]. Additionally, the shedding frequency can also be considered as was also shown in Adema et al. [2020] for airfoil. This would result in a comparison of the dominant frequencies produced by the loading of the airfoil.

Apart from a method for assessing the results of the models, the method that can be used for improving the results should also be considered. This could be done by taking the original model and simply adjusting the parameters manually to better match the data. During this phase more structural changes could also be proposed based on the observed results. A third approach for this process is using a statistical method as is outlined in section 2.6. This method calibrates the parameters using a uncertainty quantification tool. It should be noted that before this method is applied the sensitivity of the solution to different parameters should be considered as well. This is useful for the future development of the model.

Finally, this project relates to the comparison of dynamic stall simulations to experimental data. Therefore, an approach for the assessment of such results should be defined. The first step of this approach is to obtain both the experimental and simulation data. This means that the relevant parameters are to be extracted from the results. In terms of the vortex shedding this will likely be the projected Strouhal number. Next, these parameters can be compared in order to assess the performance of the model results compared to the experimental results. This could be done by comparing the L_2 norm of different models or comparing the frequencies. The L_2 norm produces a normalised error based on the square of the error at each data point.

Having outlined the methodology that is to be used to answer the research questions, it is instructive to examine how these methodologies would come together in a project plan. The first stage of this plan would consist of the collection of data. For the experimental results the experiments have already been performed as will be discussed in the next chapter. The second set of data has to be generated by the dynamic stall model. This requires the implementation of the dynamic stall models that seem relevant to the considered application.

The second phase of the plan is the comparison of the original dynamic stall models to the experimental results. Several methods that could be used for this have already been discussed in this section. The comparison will mainly consider the frequency domain. In addition, the time response of the relevant parameters can also be considered to better understand the performance of each of the dynamic stall models. This comparison is shown in chapter 4.

In the third step of the research plan, the potential improvement of the model definitions is considered. This could be achieved by calibrating the existing parameter definitions based on the previously described comparison. Another approach could be to adapt the parameter definition to be better suited for the operating conditions at hand. Both of these steps are performed in this report, in chapter 5 and chapter 6 respectively.

The three steps described above will be performed several cases of airfoils placed in deep stall conditions. For this purpose several sets of wind tunnel experiments are considered. These experiments and their results are outlined in the following chapters.

2.6 Optimisation of model parameters

This section aims to provide an introduction for the proposed calibration process of the dynamic stall models. This is done by first outlining the theoretical background of the proposed calibration process. Secondly, the application of the tool that would be used is explained. Finally, the way this information interacts with the current research is discussed.

2.6.1 Theoretical basis

The calibration method that is proposed to be applied to the discussed problem is a Bayesian inversion method as discussed in Wagner et al. [2022a]. This method is based on the definition of Bayes' theorem, Equation 2.46. This equation is meant to represent the probability that a certain input, $\mathbf{x}$, has occurred given the output, $\mathbf{y}$. The right side of the equation also contains the prior, $\pi(\mathbf{x})$, an assumed distribution of the input parameters. Additionally, the likelihood, $L(\mathbf{x};\mathbf{y})$, is also present on this side of the equation. This value is meant to represent the relatively likelihood that the observed data occurs given the current input. Finally, the factor Z, the evidence, is meant to normalise the distribution obtained from this equation. However, in the case of the calibration this factor is eliminated as the relative probabilities are the only relevant parameter as will be shown.

$$\pi(\mathbf{x}|\mathbf{y}) = \frac{\pi(\mathbf{x})L(\mathbf{x};\mathbf{y})}{Z} \tag{2.46}$$

The goal of the calibration is to obtain probability distributions for the model parameters that could result in the observed output in the experiment. In order to do this, the output from the experiment is represented as shown in Equation 2.47. This is the combination of the model evaluation with the inferred input parameters and a discrepancy term. The discrepancy term is usually a normal distribution centred around zero as the measurements are typically assumed to be unbiased.

$$\mathbf{y} = \mathscr{M}(\mathbf{x}) + \eta \qquad , \eta = \mathscr{N}(0, \sigma^2) \tag{2.47}$$

If this representation is used, the likelihood becomes relatively simple to evaluate, since the model evaluation is known. This creates a distribution around the expected value for these model parameters based on the discrepancy. It should be noted that the model evaluation does not always have to use the complete dynamic stall model. Surrogate models can be used to accelerate the process as many iterations are required for the calibration. Such models contain a representation of the actual dynamic stall model, and are typically constructed from a large number of evaluations of the original model. Additionally, the prior uses an assumed distribution of the model parameters. As such, the probability of those model parameters occurring can be evaluated as well. Therefore, the numerator of the fraction in Equation 2.47 can be evaluated for any model parameter value.

However, the goal of these methods is to obtain an estimation of the model parameters based on the data. The distribution that represents these is called the posterior and is shown on the left side of Equation 2.47. To sample and gain a distribution of the posterior, Markov chain Monte Carlo methods are typically used. These methods create a chain of points in the space of the model parameters. The chain is created by first selecting a starting point in the space. Next, samples are selected around this point. For each of these

samples the relative probability of their occurrence can be evaluated. Based on the relative probability of these samples in the posterior, the samples are accepted or rejected. This process is repeated until a large number of samples are selected which in turn represent the posterior probability distribution.

There are multiple different ways in which the different samples can be accepted or rejected. The choice in algorithm for this process mainly influence the efficiency of the inversion process but not the actual result, Wagner et al. [2022a]. It has also been shown that to obtain a correct probability distribution for the posterior a sufficiently large number of calibration points is required, Sanderse et al. [2022]. However, to obtain the Maximum A Posteriori (MAP) value much fewer sample points are required. This MAP value represents the most likely combination of model parameters based on the used experimental data. This results can be seen as the best fitting set of model parameters based on the observed data.

2.6.2 UQLAB tool applications

The implementation of the previously described process is performed using the UQLAB tool, Wagner et al. [2022a]. This tool contains functions for all required steps in the calibration process. For example, it is able to create surrogate models based on a large number of model evaluation, as well as evaluate the sensitivity of the solution to different model parameters, Zhou et al. [2019b]. This functionality can first be used to identify which model parameters in the dynamic stall models are most influential for the solution in the considered cases. Potentially, this could eliminate some parameters from the calibration and as such make the procedure simpler.

The evaluation of the BEM or VW methods does not take a very long time. However, due to the number of evaluations required in this process the computational time can still increase rapidly. Therefore, the ability to construct a surrogate model can be critical in the calibration process as well.

Apart from the sensitivity analysis and surrogate models, the UQLAB tool also provides the tools required to perform the Bayesian inversion process described previously. These methods have already been effectively implemented for this purpose by for example Ceravolo et al. [2020].

Finally, it should be noted that the calibration process has already been implemented in the context of wind turbines by TNO, Sanderse et al. [2022]. In this research the calibrations were performed on different models. However, the principles would remain the same.

2.6.3 Applicability in current research

Having discussed a method that allows for calibration of model parameters based on observations, the application to the current topic can be considered. Firstly, the model parameters that could be adapted are considered after which the performance parameters are examined.

As was discussed in subsection 2.3.5 each of the dynamic stall models has a number of model parameters that are used in the computations. Some of these parameters are based on experimental data specific to the considered airfoil. However, a large number of the model parameters are not adapted based on the airfoil and have been calibrated

based on several experimental results. These parameters are most likely to be calibrated effectively. It should be noted that these parameters have already been adapted between different versions. Therefore, a precedent has already been set for the alteration of the parameters in order to match experimental results. Examples of such changes have been discussed in the description of the Snel model and its improvements, subsection 2.3.3.

In the case of the ONERA model, it is harder to make a general calibration, as this model exclusively contains model parameters that depend on airfoil geometry. These parameters could be altered based on the comparison to the experiment, but the calibration would only be valid for the considered airfoil. Therefore, this model will not be considered in such a calibration.

Apart from the changes that can be made to the input of the model in terms of parameters, the assessment of the calibration has to also be considered. In order to be able to determine if the calibration has improved the results a performance criterion has be determined.

Since the area of interest is placed at in deep stall conditions, the results from both the simulation and the experimental data are unsteady. Therefore, choosing an optimisation parameter in time is made more difficult. As such, assessing the performance with a frequency based parameter is expected to be the most suitable for implementation. Therefore, the vortex shedding frequency is proposed as a parameter that could be used to assess the performance of the models. This parameter has already been used to compare model results to experimental data for airfoil in the past Adema et al. [2020].

Apart from the frequency, the strength of the changes in loading could also be assessed. This could be done by considering the amplitude of the variations in the loading coefficients on the airfoil.

It should be noted that the alteration of the model parameters based on this specific operating range could negatively impact the performance of the model for other conditions. Therefore, the performance of the models in operating conditions that it is more commonly applied to should also be examined during the calibration process. These conditions would for example contain pitching airfoils at more moderate angles of attack of below 30 degrees.

In addition to the calibration results, the assessment of the sensitivity of the different model parameters is also of interest. As has been discussed, the UQLAB tool also is capable of performing this analysis. The goal of considering the sensitivity is mainly to identify which parameters are most important for the prediction of the shedding frequency. This information can be useful for future adaptions of the model as well as obtaining a better understanding of the proposed definition.

Chapter 3

Wind tunnel experiments for different airfoils and operating conditions

As has been outlined in the research plan, the dynamic stall models are to be compared to different experimental results. In this chapter, the three main experiments used in this report are shown. First, an experiment by DNW is described in section 3.1. This experiment covers a large range of angles, both positive and negative. Secondly, another experiment that covers a variety of both positive and negative angles is introduced in section 3.2. This experiment was performed by the TU Delft. The third experiment that is considered is discussed in section 3.3, which covers only a range of positive angles of attack. Finally, some general conclusions are drawn based on the presented experiments in section 3.4.

3.1 DNW-HPG experiment

In this section, the results that can be extracted from an experiment performed by DNW are discussed. The data from this experiment did require some more processing compared to the other experiments. First, a description of the experiment is provided in subsection 3.1.1. Next, the approach for extracting the relevant data is outlined in subsection 3.1.2. Thirdly, the effect of blockage on the vortex shedding results is considered in subsection 3.1.3. Finally, some more observations are made based on the available data that could be relevant for the considered topic.

3.1.1 DNW-HPG experiment description

The considered experiment was performed by German-Dutch Wind Tunnels (DNW) in the High Pressure wind tunnel in Göttingen (HPG). An overview of this wind tunnel is shown in Figure 3.1. During the experiment, this tunnel caused some turbulence as well. The maximum intensity that was measured during the experiment was 0.5%. The data resulting from this experiment was provided to the student by TNO.

The tunnel used in this experiment is suitable for 2D testing, during which an airfoil is implemented over the entire width of the test section. The side view of this test section is shown in Figure 3.2 and the top and bottom of the section are equipped with pressure sensors. The airfoil can be rotated over the full 360 degree range. As such, the large angles

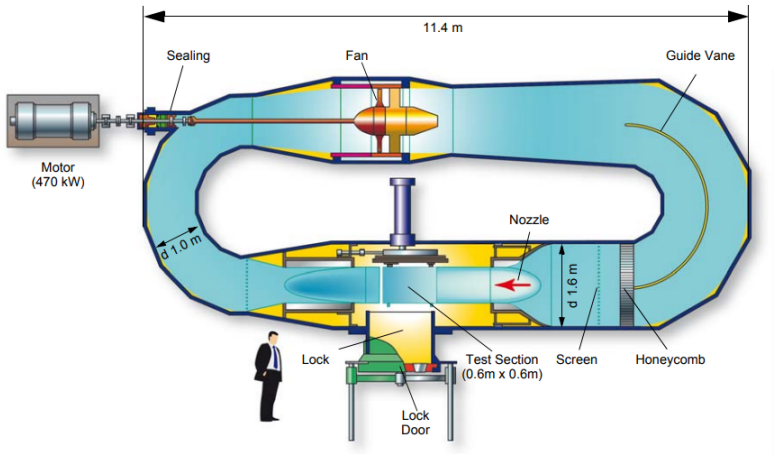

Figure 3.1: Overview of the wind tunnel layout used in the DNW experiment

of attack, required for the vortex shedding phenomena to occur, can be reached. In the experiment, a DU-00-W-212 airfoil is used for all measurements. This airfoil has a relatively high thickness to chord ratio of 21% and is commonly used in the context of wind turbine blades. The airfoil could additionally equipped with transition dots that forced transition of the flow at fixed locations. However, these were not used in the measurement points considered in for this report.

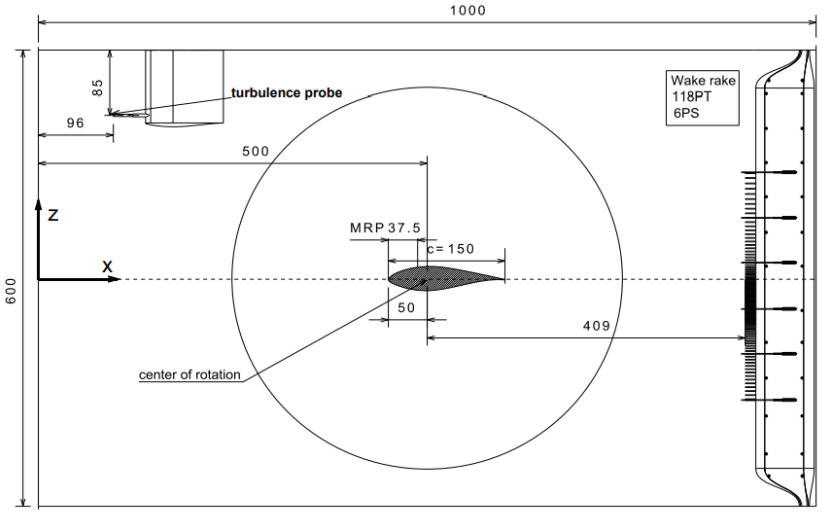

Figure 3.2: Side view of the test section that is used in the DNW experiment

From the experiment a variety of different data sources are available. The airfoil itself was equipped with 90 pressure taps along both the top and bottom surface of the airfoil to evaluate the steady local loading distribution on the section. The distribution of these pressure taps is shown in Figure 3.3. Some unsteady pressure measurements were also taken at 5 locations on the airfoil. One of the unsteady sensors was placed at 37% of the chord on the top surface. The other 4 are placed on the bottom at the following locations relative to the chord; 20%, 33%, 38% and 42%. Additionally, a wake rake was placed behind the airfoil to evaluate the flow behaviour in the wake, as can be seen in Figure 3.2. Finally,

measurements can be obtained from a force balance that is attached to the model. Using the wake and the force balance, both steady and unsteady measurements of the loading on the airfoil can be obtained. It should be noted that some oil flow visualisations were also performed, however these are not considered in the current analysis.

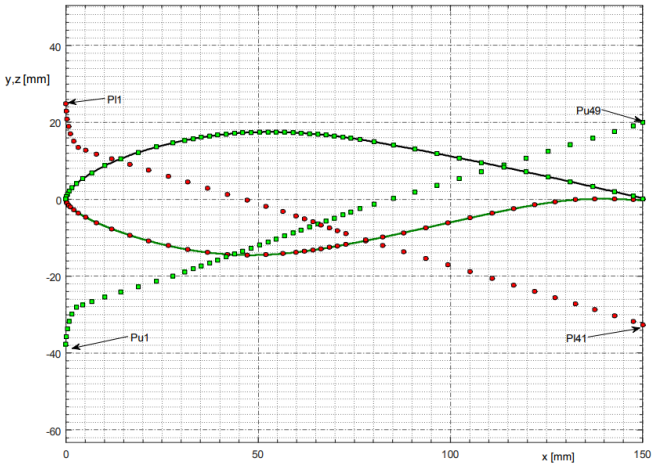

Figure 3.3: Location of the pressure taps placed on the DU00W212 airfoil used in the experiment

With the test setup described above, a large number of measurements was completed. These ranged over different Reynolds numbers, angles of attack and total pressures. The data has primarily been used for the validation of airfoil performance codes at high Reynolds numbers, Ozlem et al. [2017]. This work especially used the relatively low angles of attack. In the present work however, the data set that is found to be most relevant is the one that contains the largest variation in angles of attack. This data set consists of measurements at a Reynolds number of 6 million and a total pressure of 64 bar. During the measurements the angle of attack of the airfoil is varied from -90 to 90 degrees. This allows for the expected flow phenomena related to dynamic stall to be examined. It also ensures that a significant portion of the selected data points should show vortex shedding behaviour based on the discussed literature.

3.1.2 Results of the DNW experiment

Having outlined the test setup used in subsection 3.1.1, the data obtained from the experiment can be considered. To do this, the chosen methods for obtaining the different results are discussed. First, some general measurements obtained from the experiment are outlined. After, the unsteady loading is considered. There are two aspects that are considered, the dominant frequencies and the time dependant representation of the loading. The processes for obtaining both of these are examined individually.

General measurement results

Some of the data obtained in the experiment has already been processed and therefore can be presented directly. The first of these results is the steady force polar, which is shown in Figure 3.4. This polar shows all the expected behaviour from airfoils over such a range of

angles of attack. There is a linear region for the smaller angles at which the flow remains attached. After which the onset of stall takes place. During this stage the lift decreases, while the drag experiences a sudden increase. Finally, the normal force coefficient keeps increasing as the airfoil is placed more perpendicular to the flow. This data will be used to determine the difference between the potential loading and the steady loading in the dynamic stall models. This terms has been shown to be an important contribution in the previously discussed dynamic stall models.

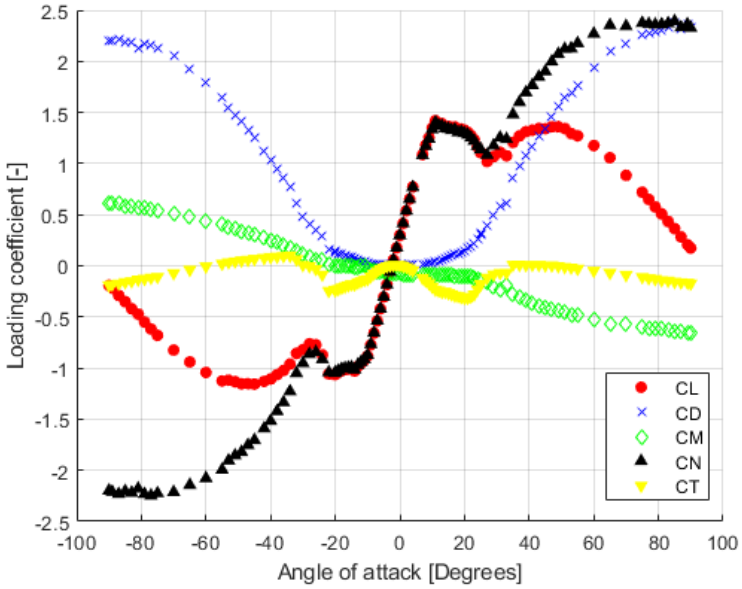

Figure 3.4: Airfoil polar from DNW experiment

Another result that can be immediately be analysed is the pressure sensor data. The steady results are available over the length of the airfoil. An example of such an average pressure distribution is shown in Figure 3.5a and Figure 3.5b. In this image the pressure distribution is shown by the blue dots. Additionally, the unsteady sensor results are included through 5 box plots placed at the previously discussed locations. These box plots represent the variation of the pressure coefficient at each location. The first box indicating a single standard deviation and the horizontal lines representing three standard deviations. From these results the local state of the flow can be considered. For example in Figure 3.5a relatively large unsteadiness of the sensor on the top surface can be observed. This sensor is shown in the lower part of the plot. Therefore, it can be concluded that this location on the airfoil is not likely to be experiencing attached flow. This is to be expected as the airfoil is placed at an angle of attack of 27 degrees for these results.

Frequency analysis

To obtain more information from the unsteady measurements some processing has to be done. As is already observed through the variation of the pressure coefficient, the measurement of the loading varies in time. This unsteady result is the area of interest for the current research, as goal is to develop a model to predict this unsteady behaviour. To consider this aspect of the data, the frequency spectrum of the loading is first constructed. This is done

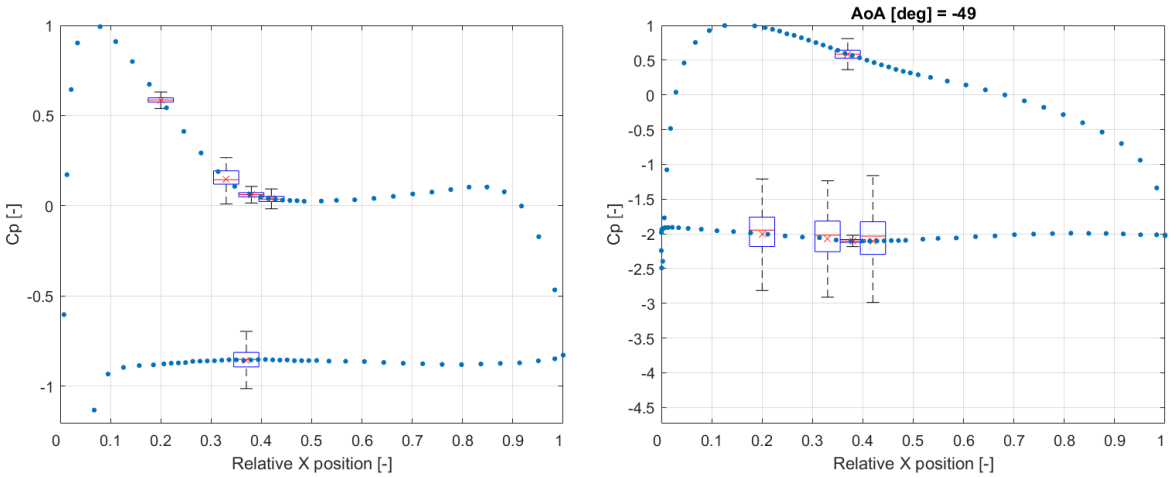

(a) Loading distribution at 27^o including variations from unsteady measurements

(b) Loading distribution at -49^o including variations from unsteady measurements

Figure 3.5: Examples of unsteady and steady pressure distributions from measurements

by considering the frequencies that are dominant in the loading of the airfoil. There are two different measurements that can be used for this purpose. Firstly, the force balance data can be considered. Secondly, the unsteady pressure sensors are also available.

First, the results from the force balance are analysed. To represent the frequencies present in the loading, the projected Strouhal number is used. The frequency spectrum of this loading is obtained by applying the Fourier transform to the time signal. The approach used for obtaining the time signal from the balance data is shown in appendix A. From the frequency spectrum peaks can be identified. These represent the dominant frequencies in the response. The process for selecting such peaks is shown in more detail later in this section.

The force balance provides results in two directions, one parallel and one perpendicular to the airfoil orientation. The dominant frequencies for both loading directions of the force balance are shown in Figure 3.6, which shows the 3 most significant frequencies present in each direction. Based on the previously presented literature, the vortex shedding behaviour is expected to occur for projected Strouhal numbers between 0.15 and 0.2 for larger angles of attack. In the results, slightly higher values of vortex shedding frequencies are found for angles larger than 30 degrees. Additionally, it does appear that the projected Strouhal number varies with the angle of attack, which is not expected.

At lower angles of attack, different frequencies are expected to be present. These lower frequencies are observed to produce similar Strouhal numbers compared to literature, as was discussed in chapter 2. The only range of frequencies that has not been previously been observed is the V-shape located at angles of attack below 30 degrees. The origin of these frequencies could not be identified and remains an area for future investigation. However, as the vortex shedding behaviour appears at larger angles of attack, this does not affect the current investigation.

Apart from the use of force balance data to study the unsteady results, the unsteady pressure measurements can also be considered. The provided data already contained the normalised pressure fluctuations observed by the sensors. Therefore, no additional processing was required on the part of the author. For these measurements the Fourier trans-

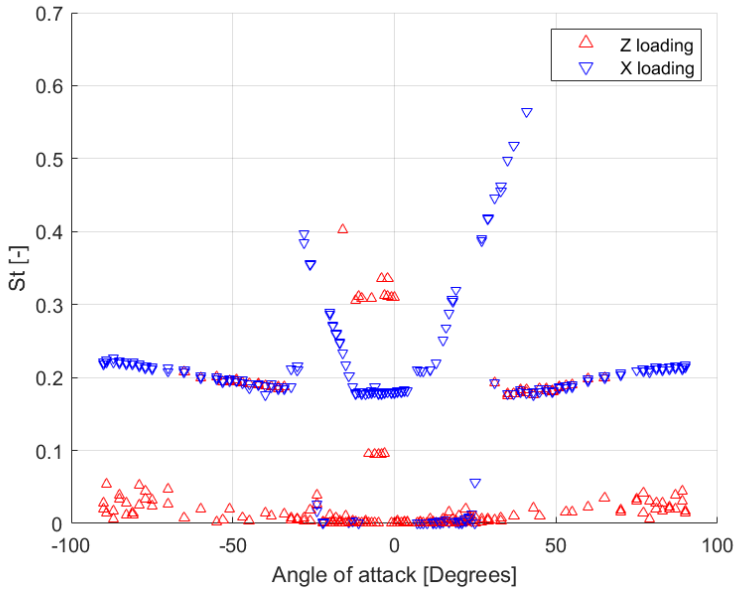

Figure 3.6: Projected Strouhal numbers present for different angles of attack in both loading directions

form is once again used to obtain the frequency spectrum of the signal. Some examples of the frequency spectra from each available source are shown in Figure 3.7 to Figure 3.9.

Each of the images shows the frequency spectra from 7 different results. The first two spectra contain the results of the force balance in both loading directions. The next 5 spectra contain the frequencies present in the signal from the unsteady pressure sensors. These different results can be compared to ensure the validity of the results and produce a method for extracting the vortex shedding frequencies.

Based on the shown Fourier spectra shown several conclusions can be drawn. Firstly, the fourth unsteady pressure sensors appears to produce erroneous results in quite some cases. This conclusion is based on the fact that the peaks occur at different frequencies compared to all other sensors. Additionally, the spectrum of this sensor does not show any significant peaks at all for some angles, for example in Figure 3.9. However, based on the other sensors, some peaks should be present in the frequency spectrum at this angle of attack. Therefore, it is assumed that the results produced by this sensor should be discarded.

The second observation that is made about the frequency spectra is the peak present around 60 Hz for the balance force in X. This peak is present for a variety of angles of attack. However, no clear origin can be found. A possible explanation could be the movement of the balance itself or some other disturbance in the signal. It is important to note that no such peak is present in any of the pressure sensors. This suggests that this part of the signal is not present on the surface of the airfoil, and thus is not an aerodynamic effect. Therefore, it is excluded from the analysis.

Thirdly, it is observed that the frequency peaks are most clearly defined in the spectra of the pressure sensors facing away from the incoming flow. This is especially true for larger angles of attack. For example, in Figure 3.8, the first pressure sensor shows the most clearly defined peak. This sensor is placed in the top surface of the airfoil and thus faces away from the incoming flow. This behaviour could also be observed for other larger angles of attack. The is to be expected as the unsteady effects of vortex shedding and stall mostly take place

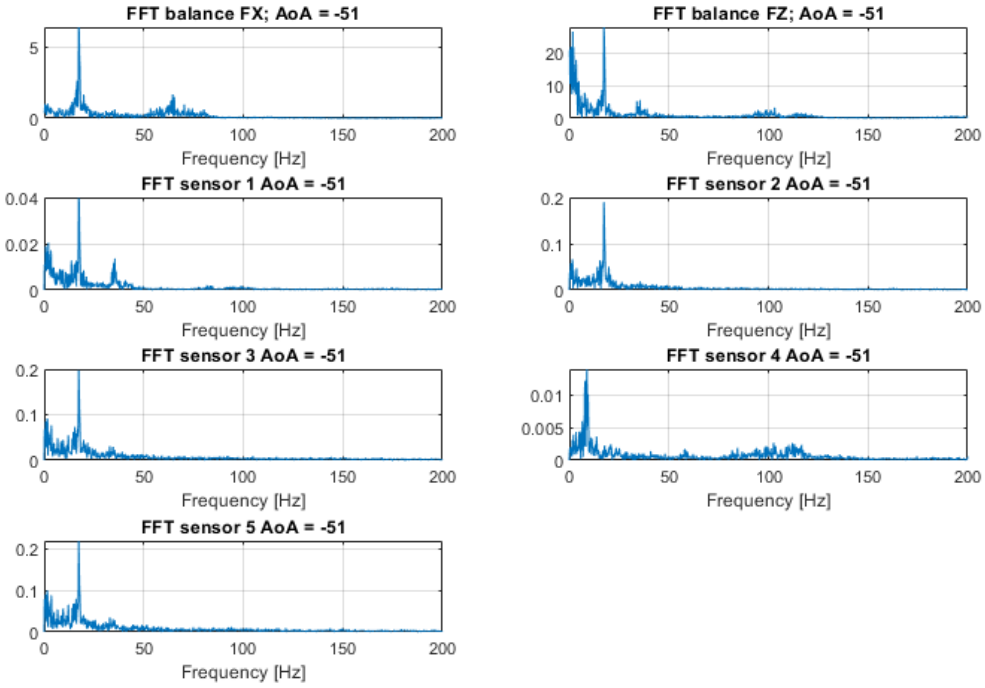

Figure 3.7: FFT values for the different unsteady sensors at -51 degrees angle of attack

on this side of the airfoil.

Based on the observations in the FFT spectra, potential problems in identifying the dominant frequencies can be found. In Figure 3.9 it can be seen that the shedding frequency peak might not always be correctly identified, if a single spectrum is used. This is the results of some large peaks being present at low frequencies, in for example the first pressure sensor or the Z direction of the balance. To resolve this problem the shedding frequencies is selected only if the found peak is present in multiple sensors. In the example of Figure 3.9, this would result in the peaks at approximately 30 Hz. These can be seen in multiple pressure sensors and thus this frequency is selected as the shedding frequency.

Additionally, a minimum and a maximum frequency should be considered when selecting peaks from the FFT result. These implemented to eliminate peaks that do not correspond to the vortex shedding behaviour. The minimum frequency was set to 3 Hz to resolve any issues with peaks at very low frequencies. The maximum frequency was set to 300 Hz. This was done to eliminate any peaks that result from a distortion caused by the main drive electrical system. These peaks occur at any integer multiple of 300 and do not relate to any physical process that is to be observed. This information was provided by DNW in the internal reporting of the experiment.

Finally, it can be observed that the main peaks that are present in the balance results are also present in the pressure sensors. This is an expected result as the force on the balance is expected to be the result of the pressure distribution. Therefore, both methods could theoretically be used to select the vortex shedding frequency.

To investigate the use of either measurement, the two sensors are compared in Figure 3.10. Based on this, it appears the main frequency peaks could be identified for all an-

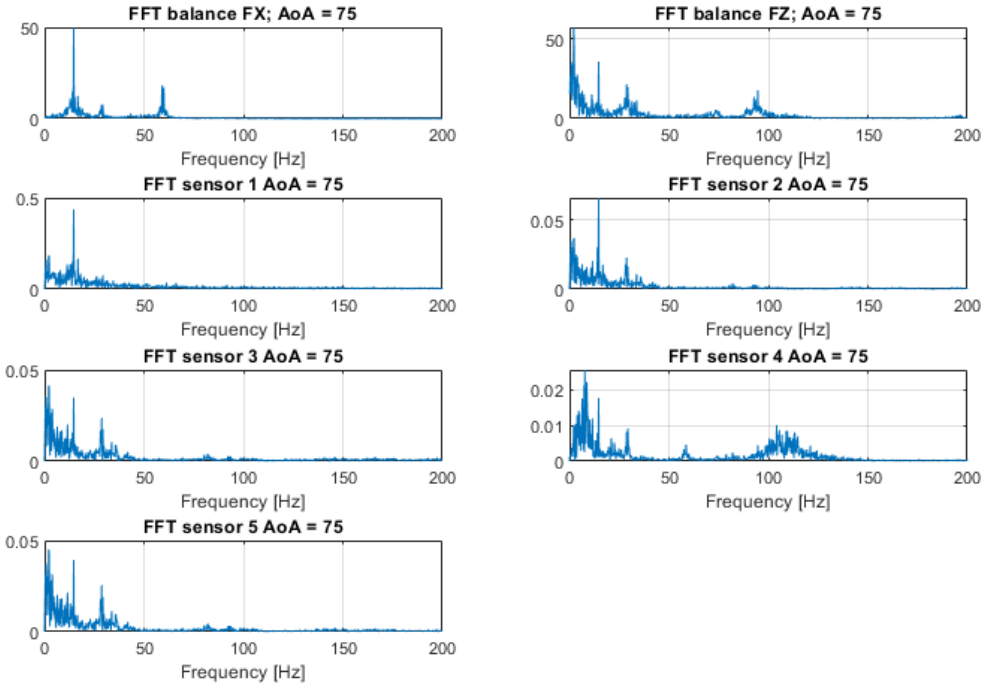

Figure 3.8: FFT values for the different unsteady sensors at 75 degrees angle of attack

gles of attack using both the force balance or the pressure sensor data. It should be noted that the fourth sensor was excluded from Figure 3.10a. Interestingly, the V-shape that was observed in the frequencies of the force balance data is not present for the pressure sensors. This could mean that these frequencies are not a result of an aerodynamic effect on the surface of the airfoil. Most importantly, the comparison shows that the dominant vortex shedding frequencies obtained from the pressure sensors are very similar to the ones from the force balance. For this purpose on angles of attack larger than 30 degrees are considered as these are expected to correspond to vortex shedding behaviour.

As a result of the presented analysis, an approach for determining the dominant shedding frequencies for each angle can be defined. The results from the pressure sensors were chosen to be used for the definition of the vortex shedding frequencies. This selection was deemed to be more desirable for several reasons. Firstly, more pressure sensors are available at each angle of attack. Since multiple of these sensors have to show the same frequency, this allows for a more accurate determination of the shedding frequency. Additionally, the pressure sensors are not subject to any structural interactions as they are directly measuring a flow property at the airfoil. This could be a reason for some frequencies not being present in their signal, while being shown in the results of the force balance. Thirdly, the pressure sensors measure the pressure directly, without having to apply any additional processing to the signal as is the case for the balance. Finally, this approach is also used for obtaining the frequencies in the TU Delft experiment presented later in this chapter. Therefore, selecting this method could eliminate differences caused by the processing approach.

Having selected the pressure sensors as the source for the shedding frequencies, the

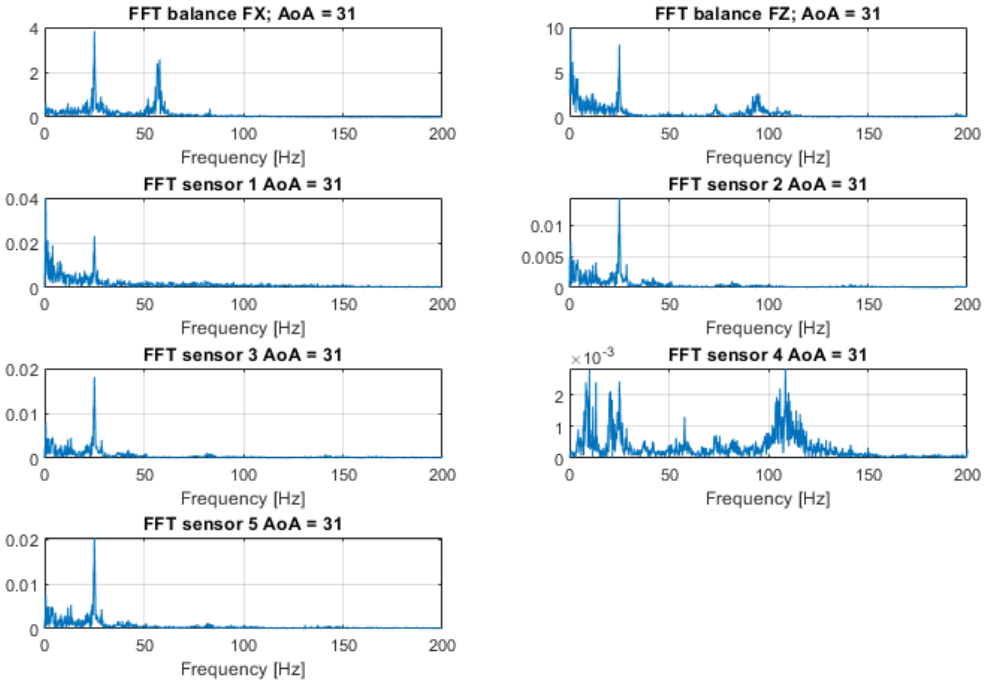

Figure 3.9: FFT values for the different unsteady sensors at 31 degrees angle of attack

described process can be applied to obtain these. In Figure 3.11 the resulting dominant frequencies are shown.

From Figure 3.11, the range at which vortex shedding occurs can clearly be identified. This is done by considering the projected Strouhal numbers that are associated with the shedding behaviour. These values are typically located in the range of 0.15 to 0.2 for all angles of attack at which vortex shedding occurs. Based on this, the near constant range of frequencies that is centered around 0.2 can be identified as the vortex shedding frequencies. Therefore, vortex shedding is found to not be present in this experiment below 30 degrees.

It should be noted that these frequencies do show a larger variation with angle of attack than expected. Additionally, the mean value of the projected Strouhal number is higher than typically reported. This is expected to be caused by blockage effects as these have been shown to increase the Strouhal number at lower Reynolds numbers Wang et al. [2021]. This will be considered in more detail in subsection 3.1.3.

Unsteady balance measurements

Another potentially relevant result form the experiment that can be considered is the loading of the airfoil in time. This can be obtained from the force balance data. To extract this several steps had to be taken, which are outlined in appendix A. These results will be used to compare the response of the dynamic stall models in time to the experiment.

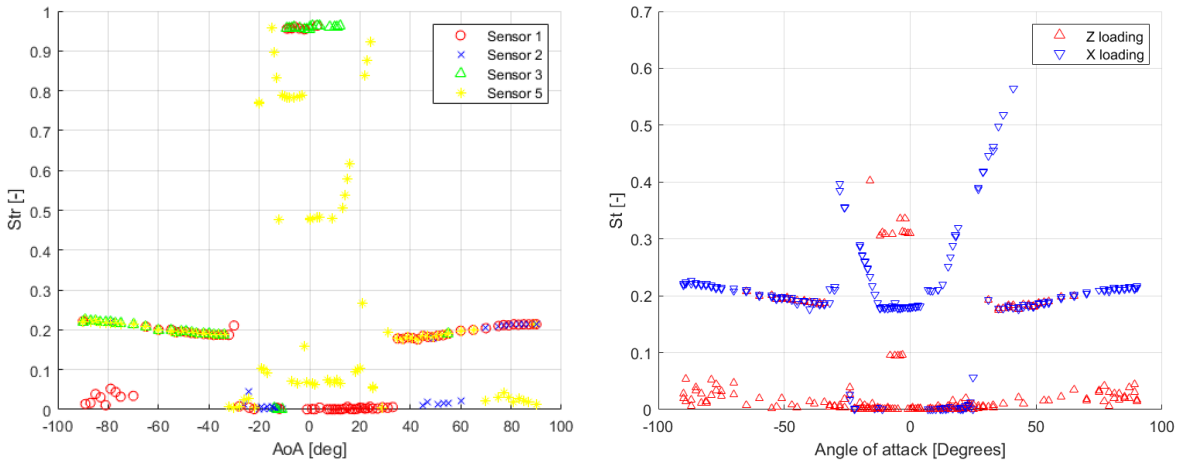

(a) Projected Strouhal numbers for each pressure sensor

(b) Projected Strouhal numbers from force balance

Figure 3.10: Frequency responses in both measurements

3.1.3 Blockage effects of DNW experiment

In subsection 3.1.2 it was observed that the shedding frequencies produced by this experiment varied from the values expected from literature. It was theorised that the effect of blockage could be a reason for this discrepancy. In this section the effect of blockage on vortex shedding behaviour is first examined based on available literature. Next, possible options for a correction are examined before correcting the data for this effect.

Blockage effects from literature

In literature the effect of the blockage on shedding behaviour is typically considered for the case more general and blunt shapes. However, the shedding behaviour of an airfoil tends to be similar to such shapes at large angles of attack. Therefore, the results are expected to be similar and corrections are generally applied in a similar sense.

Firstly, the effects of the blockage has been analysed using numerical and experimental results in Sharify et al. [2013]. The considered Reynolds number is only 1000 for a square cylinder. For this problem it was found that the Strouhal number related to the vortex shedding of this shape increases with blockage ratio. The blockage ratio is defined as the ratio between the cylinder height and the wind tunnel section height. This definition will be used in the case of all other shapes as well. These conditions are quite different from the considered airfoil cases in terms of shape and Reynolds number. However, the behaviour observed here appears to be representative for cases with more similar conditions as will be explored.

Another experiment which considered several blunt shapes is shown in Wang et al. [2021]. In the experiment, tests were performed at slightly higher Reynolds numbers, $R_e \sim O(4)$. This research also showed an increase of the shedding frequency with blockage ratio for all shapes. Additionally, it aimed to show the origin of this increase. It was concluded that the increase in shedding frequency is the result of the increased velocity at the model position. The velocity is increased in this section due to the model blocking a part of the airflow, while the mass flow has to remain constant. Based on this, a correction was devised which used the blockage ratio, β, to adapt the expected Strouhal number with a factor. This

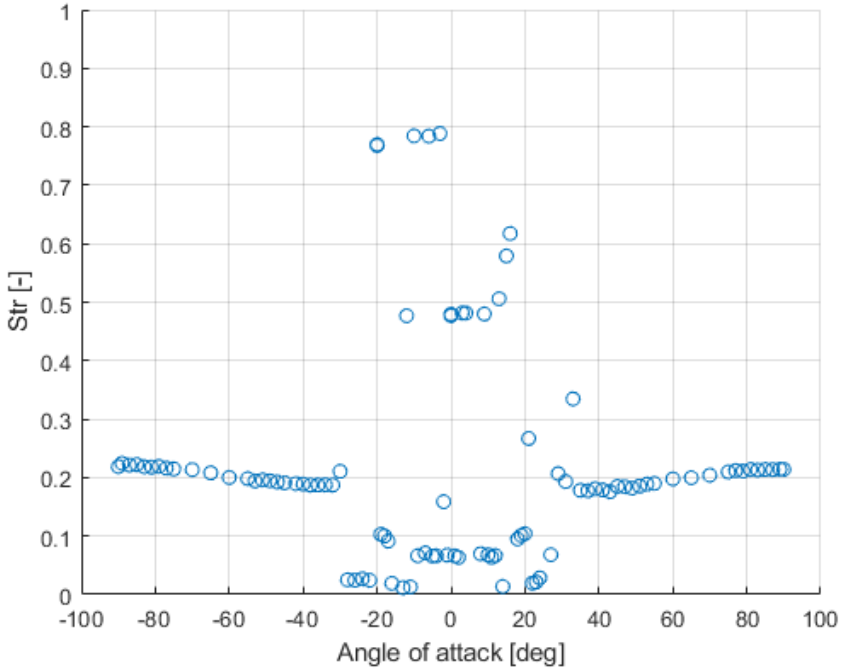

Figure 3.11: Selected projected Strouhal numbers based on discussed approach

correction is described as $St = St_0 \cdot (1 - \beta)$ and showed a reasonable correspondence with experimental results for the considered cases.

Thirdly, an experiment was performed for rectangular prisms at a higher Reynolds number, $R_e \sim O(5)$, Awbi [1978]. This experiment once again showed an increase of shedding frequency with blockage ratio. No correction was investigated in this research.

Therefore, it is concluded that, based on the described experiments, the Strouhal number is typically increased for general bluff bodies as the blockage ratio increases. Therefore, a more extensive investigation into the possible corrections of the shedding frequency is worthwhile.

Several correction methods are available based on the blockage ratio, apart from the simplest blockage correction that was already discussed. First, two simple adaptations of this correction are suggested. The first was presented by Ota et al. [1994], which is shown in Equation 3.1. In this correction the ξ term is an empirical value, which was set to 0.82 for a flat plate. This value was further investigated for inclined plates by Chen and Fang [1996] and for airfoil by Besem et al. [2016]. These studies suggested a value for ξ of 1.21 and 1.6 respectively. This variation does suggest that the parameter is dependent on the model shape.

A second simple correction method was proposed by YEUNG [2009], which is based on the self-similarity of the flow past several confined bluff bodies. This resulted in Equation 3.2. This equation once again requires an empirical constant for the correction.

$$St_c = St_0(1 - \xi\beta) \tag{3.1}$$

$$St_c = St_0(1 - \beta)^{\xi} \tag{3.2}$$

A more complicated method for correction is presented by Zhou et al. [2019a]. This

method is based on the predictions of an airfoil over a range of angles of attack contains more parameters as is shown in Equation 3.3. In this equation both μ and λ are empirical parameters with a value of 1.15 and 0.28 respectively. These values were based on a NACA-0012 airfoil.

$$St_c = St_0(1-\mu\beta)(1.7-sin(\alpha)^3)^{\lambda} \tag{3.3}$$

In conclusion, the shedding frequency of airfoils as well as general blunt bodies is affected by the blockage ratio. Several corrections are available based on experimental and simulation results. These corrections typically are based on a correction factor applied to the measured results. After this correction a constant value of the projected Strouhal number is obtained, as would be expected. In the next section the effect of several of these corrections are considered for the DNW experiment.

Corrections applied to DNW experiment

As discussed several possible corrections are available for the shedding frequency due to blockage. In this section the effect of these corrections are applied to the results of the DNW experiment.

However, one additional correction on the velocity is considered. This is based on the wind tunnel corrections already used in the DNW experiment as discussed in appendix A. This correction produced an interference velocity at the airfoil. Based on this a new effective velocity is obtained for which the correction factor is defined as η. This new velocity can also be used to normalise the shedding frequency. Since the other methods are also based on an altered velocity at the airfoil, it was found to be interesting to also consider the effect of this correction. The effect of the different velocity corrections is shown in Figure 3.12.

From Figure 3.12, it can be observed that the considered corrections have a large effect on the projected Strouhal numbers that resulted from the data. Firstly, the suggested correction based on the already applied wind tunnel corrections varies greatly from the other corrections. Therefore, this approach not considered as a viable option for correcting the Strouhal number.

Secondly, the two corrections shown in Equation 3.1 and Equation 3.2 produce very similar results. For these corrections the empirical parameter ξ was set to 1.15 and 1.2 for the respective corrections, similarly to Zhou et al. [2019a].

Additionally, the corrected values of the Strouhal number in both of these corrections have a close to constant value. This value appears to be centred around 0.15 approximately, which is a very similar result to the result obtained in other experiments as was discussed in chapter 2.

Another observation that can be made at this point is the fact that the variation with angle of attack is almost entirely removed with relatively simple corrections. This variation was the reason for the introduction of more complex corrections as shown in Equation 3.3. The usage of the projected Strouhal number might be the reason for this observation. Therefore, it is concluded that the relatively simple corrections are sufficient in terms of correcting the projected Strouhal number for this experiment.

In conclusion, it would seem that either of the simple corrections shown in Equation 3.1 and Equation 3.2 can be used to correct for the blockage effect. When applied, the results

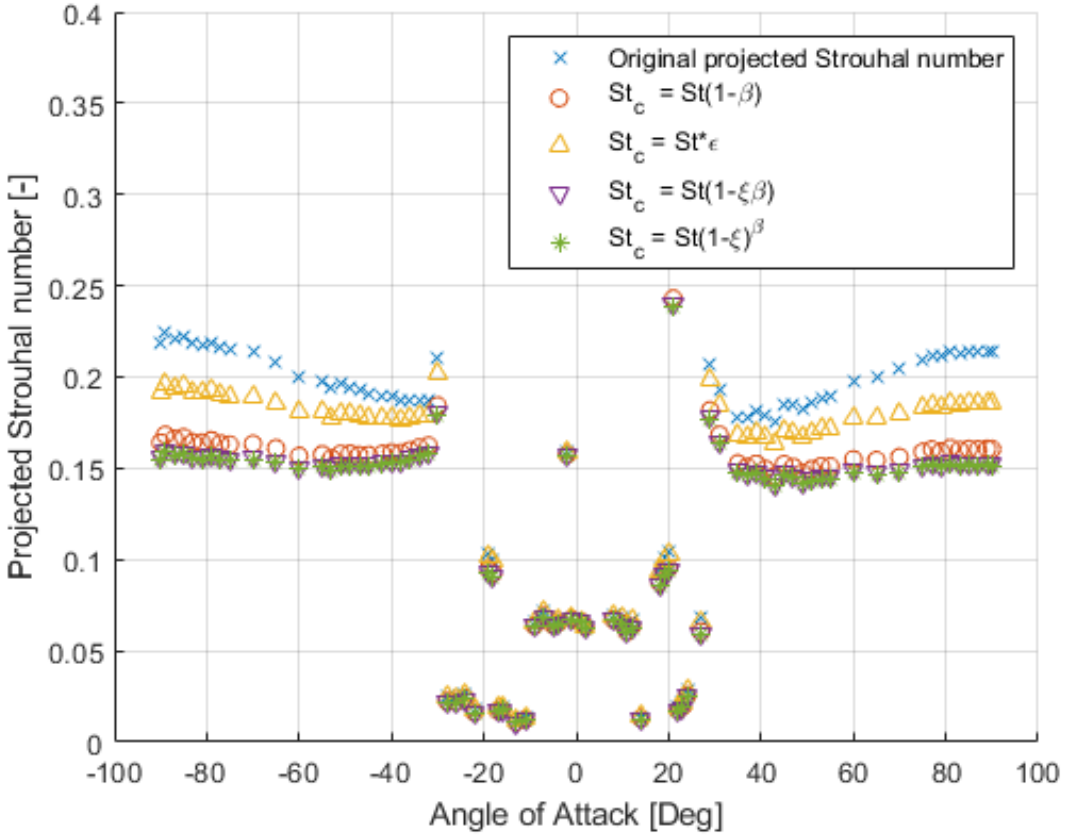

Figure 3.12: Effect of different corrections on the projected Strouhal number

of the projected Strouhal number are very much in line with the expected results from literature. In rest of this report Equation 3.1 is used as a correction for the Strouhal number.

3.1.4 Initiation of vortex shedding

In subsection 3.1.2 it was concluded that the vortex shedding behaviour only occurred at angles larger than 30 degree. This conclusion was based on the dominant frequencies found in the pressure sensors. In order to support this conclusion further, another parameter can be considered. This parameter is the base pressure coefficient, k, which is defined as shown in .Equation 3.4. In this equation $C_{P,s}$ is the average pressure coefficient on the suction side of the airfoil. As the DNW experiment contains pressure sensors over the entire range of the airfoil, this value can be obtained from the available data.

$$k = \sqrt{1 - C_{P,s}} \tag{3.4}$$

In Fallahpour et al. [2022] this definition is used to investigate the onset of shedding behaviour. As the angle of attack increases, the base pressure coefficient increases. Once the value of the parameter passes 1.4, vortex shedding behaviour starts to become dominant for that experiment. In Figure 3.13 this behaviour is shown visually. For a cylinder the onset of vortex shedding is also observed once the base pressure coefficient passes this same value. Therefore, in Fallahpour et al. [2022] the applicability of this parameter on different

shapes was identified as an area of future research. In this section, the results of the DNW experiment are considered in this context.

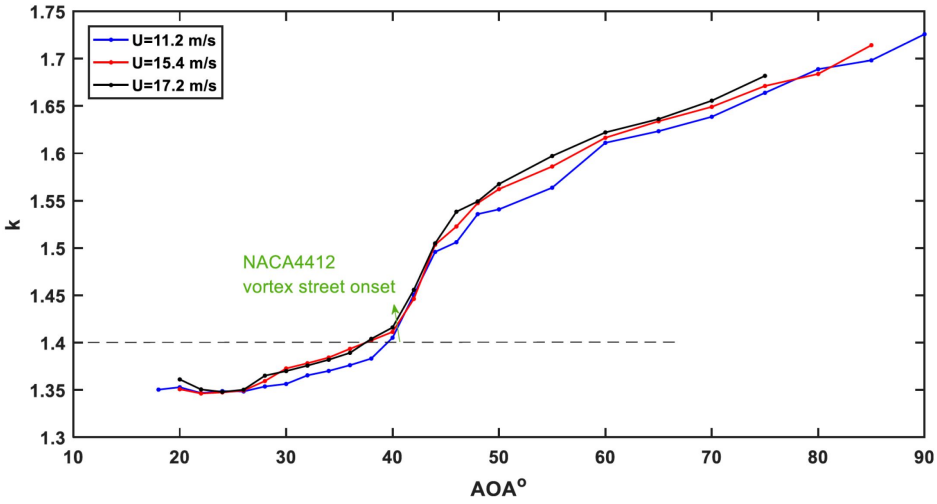

Figure 3.13: Base pressure coefficient variation from Fallahpour et al. [2022]

Using the already discussed average pressure measurements obtained in the DNW experiment, the base pressure coefficient can be obtained. In Figure 3.14 the variation of k with angle of attack is shown. There are some differences in these results compared to Figure 3.13. The DNW experiment appears to not have a near constant value of k before the onset of vortex shedding. In Figure 3.13, the base pressure coefficient is approximately constant at this stage. As of now no complete for this has been found but this could be investigated further. However, a potential reason could be the number of pressure sensors used. The experiment shown in Figure 3.13 uses only 18 pressure sensors, while the DNW experiment uses 90 sensors.

However, at around 30 degrees the base pressure coefficient does increase beyond the 1.4 for the DNW experiment. This is approximately the same angle at which a dominant frequency starts to appear at frequencies that are expected to be related to vortex shedding. This result suggests that this threshold for the base pressure coefficient could be useful in determining the onset of vortex shedding behaviour in airfoils. However, this claim should be investigated for a larger number of shapes before this can be confirmed.

3.2 TU Delft experiment

In addition to the data obtained by the DNW measurement, an experiment performed by the TU Delft is also to be used. This experiment uses a different airfoil and operating conditions. Therefore, it can be very useful to provide insight in the applicability of the conclusions drawn from the comparison of dynamic stall models.

3.2.1 TU Delft experiment description

The TU Delft experiment is performed in the Low Speed Low Turbulence Tunnel at the university with a DU91-W2-250 airfoil section Xu et al. [2023]. To measure the pressure on the

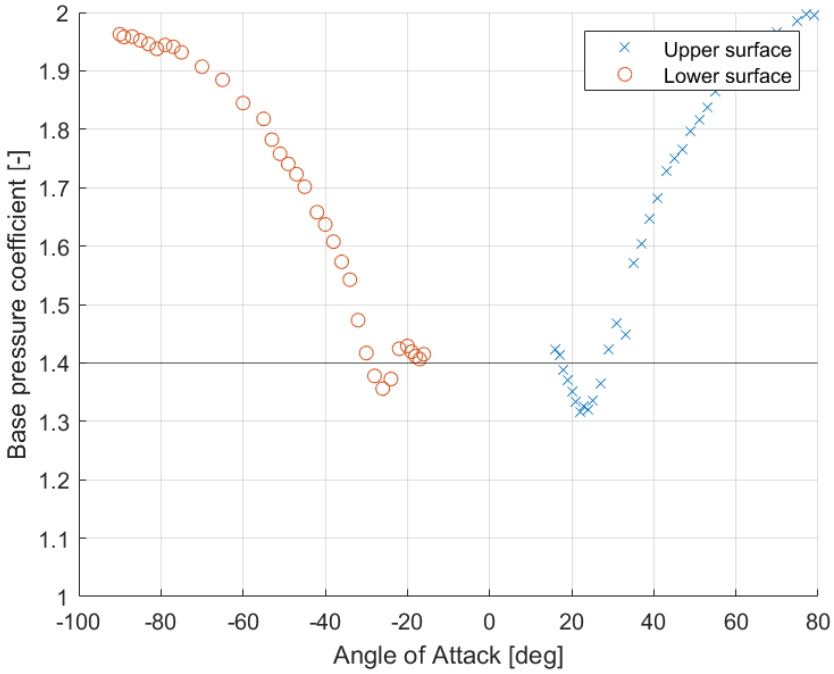

Figure 3.14: Base pressure coefficient variation from DNW experiment

airfoil, 21 taps are placed on either side of the airfoil. These sensors are able to measure the pressure with a frequency of 331.6 Hz. The loading is obtained by integrating the pressure over the surface. Some turbulence was expected in the results of this experiment. However, no more than 0.2% intensity is present due to the large contraction ratio of the tunnel. This is the lowest turbulence intensity of the three considered experiments.

This airfoil was tested over a large range of angles of attack. Firstly, from 0 to 130 degrees, and secondly from 175 to 310 degrees. The gaps in these ranges are the result of physical limitations in moving the airfoil. The experiments were repeated for three different Reynolds numbers; $2 \cdot 10^5$, $5 \cdot 10^5$ and $8 \cdot 10^5$. The inclusion of this data in the analysis can be especially valuable as both a different airfoil and different operating conditions are used.

It should be noted that in these experiments PIV measurements were also performed. These could be used to analyse the state of the flow around the airfoil and explain any unsteady results that are obtained from the force measurements. However, these results are note explicitly used in this report.

3.2.2 Results TU Delft experiment

In contrast with the DNW experiment, the processing of the TU Delft experiment has already been completed. Therefore, the results are immediately discussed. In this report, the shedding behaviour is the main concern. Therefore, the shedding frequencies based on the pressure sensors are presented in Figure 3.16a. Additionally, the projected Strouhal numbers are shown in Figure 3.16b.

From Figure 3.16 it can be observed that the frequency response of the TU Delft experiment produce frequencies in the expected range. Interestingly, the response of the pro-

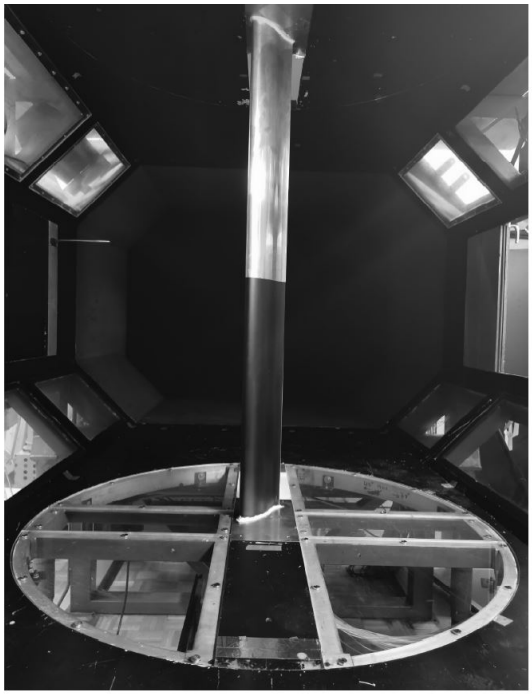

(a) Airfoil position in wind tunnel TU Delft

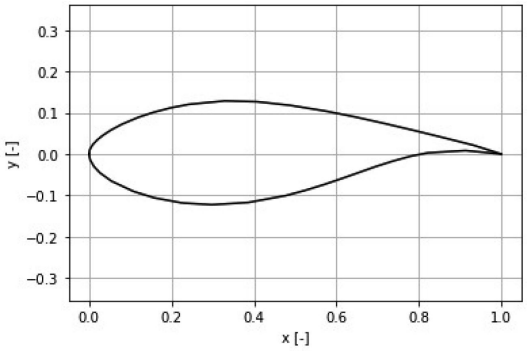

(b) Geometry of the DU91-W2-250 airfoil

Figure 3.15: Setup of the TU Delft experiment, Xu et al. [2023]

jected Strouhal number is not symmetric for positive and negative angles of attack. This is likely caused by an interaction of the geometry with the flow, when concave side is oriented towards the flow direction, Xu et al. [2023]. Such behaviour has also been observed in other results Pellegrino and Meskell [2013].

Additionally, it should also be noted that the frequencies shown in Figure 3.16a consistently show minima at locations in which the airfoil is placed perpendicular to the flow. This behaviour is to be replicated by the proposed dynamic stall model later in this report.

3.2.3 Blockage corrections TU Delft experiment

It should be noted that the data from this experiment has not been corrected for the blockage. The reason for this is the relatively small blockage ratio of 12% when the airfoil is placed perpendicular to the flow compared to the 25% of the the DNW experiment. In the case of the DNW experiment a correction was required for the resulting Strouhal numbers to approach expected values from literature. However, in the case of the TU Delft experiment the values for the Strouhal number before any correction already correspond to such values. Therefore, it would be interesting to investigate the effect of applying a correction for the shedding frequency to this data set regardless. The chosen correction is the one presented in Equation 3.1. The results are shown in Figure 3.17.

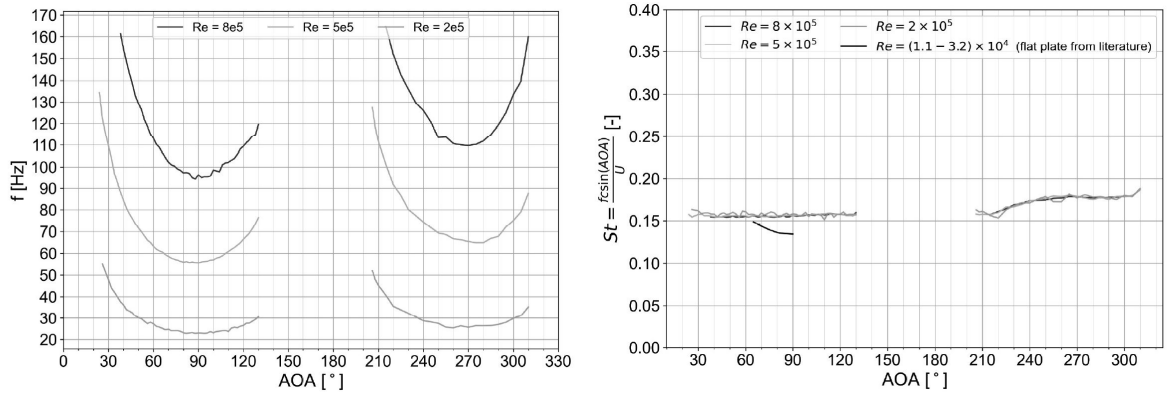

(a) Shedding frequencies TU Delft experiment

(b) Projected Strouhal number TU Delft experiment

Figure 3.16: Frequency results of the TU Delft experiment, Xu et al. [2023]

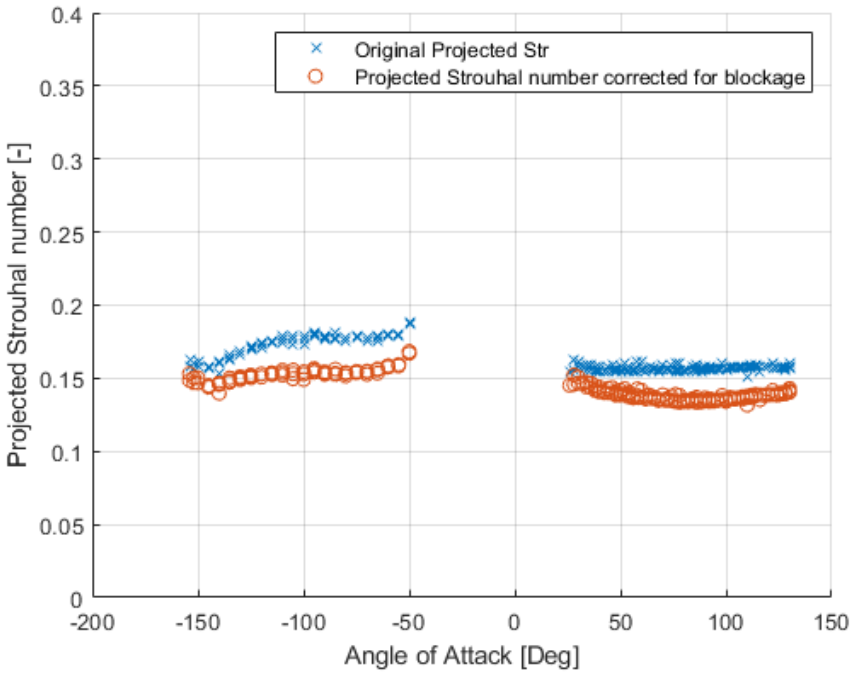

Figure 3.17: Effect of blockage correction on the projected Strouhal number of the TU Delft experiment

Based on Figure 3.17 several observations can be made. The first observation is that the frequencies for positive angles of attack no longer produce the constant projected Strouhal number that was present before. On these angles of attack the expected constant Strouhal number was achieved without any correction for the blockage.

Secondly, the negative range of angles does produce a more constant response in terms of the projected Strouhal numbers after the correction. In fact, much of the variation present in the response on this side is reduced by applying this correction. The difference in the response of either side of the rotation is therefore an interesting area of further investigation.

Finally, it should be noted that the effect of the correction is smaller in the case of the TU Delft experiment compared to the DNW experiment. This is the result of the airfoil area

being smaller compared to the wind tunnel section area. In fact the maximum blockage ratio for the TU Delft case is only 0.12 whereas the DNW experiment can reach ratios of up to 0.25 instead.

In the rest of this report the data from this experiment is considered without blockage correction. This is done for two reasons. Firstly, the results before the blockage correction correspond with expected results from literature. Additionally, the blockage ratio is relatively small with a maximum value of 0.12 when the airfoil is placed perpendicular to the flow. In previous experiments on bluff bodies, blockage ratios below 10% were found to have little effect on the aerodynamic behaviour, Choi and Kwon [1998]. For this experiment, most angles produce a blockage ratio lower that this value. This observation, in combination with the fact that the uncorrected values correspond with results from literature, suggest that no correction is required. Therefore, the projected Strouhal numbers shown in Figure 3.16b will be used in the rest of this report.

3.3 NACA 4412 experiment

In this section, a final experiment that is to be used in the assessment of shedding behaviour is outlined. This experiment once again uses a different airfoil operating at a different Reynolds number compared to the previous experiments. Therefore it should allow for a more complete understanding of the applicability of the models.

3.3.1 Description of NACA 4412 experiment

In Fallahpour et al. [2022] a stationary NACA 4412 airfoil is placed in the AmirKabir University of Technology (AUT) open loop wind tunnel. The airfoil is considered over the range from 0 to 90 degrees, thus including only positive angles of attack. The Reynolds number in this experiment is lower compared to the other experiments discussed so far. Two measurment conditions are included with Reynolds numbers of $9.8 \cdot 10^4$ and $1.5 \cdot 10^5$. The experiments were performed in a 1X1m test section. An airfoil model with a span of 0.45m and a chord of 0.15m was placed in this section. To remove 3D effects an additional plate was installed to cover the width of the section. This experiment did also experience some turbulence. The maximum intensitty found during the experiment was 0.5%, which is similar to the other two experiments.

In order to measure the loading on the airfoil, the model is equipped with 18 pressure sensors over the cross section. The location of these sensors is shown in Figure 3.18. In addition to the pressure sensors, a hot-wire anemometry setup was placed behind the airfoil. This setup measures at a high frequency and thus allows for the dominant frequencies present in the response of the airfoil to be extracted. Using a combination of these two measurements, the airfoil polar as well as the dominant frequencies are obtained. Both of these results are required for the comparison to the dynamic stall model.

3.3.2 Results of the NACA 4412 experiment

Based on the data from the experiment, several results are presented. First, the airfoil polar is considered in Figure 3.19. In this polar several regions are defined based on the behaviour of the lift coefficient of the airfoil. Within these regions different effects are taking

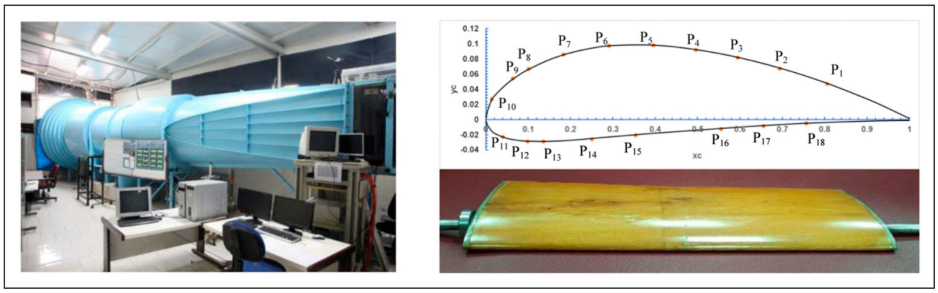

Figure 3.18: Setup and measurement locations from Fallahpour et al. [2022]

place, such as the stall occurring in region 1. It has been concluded that the vortex shedding becomes a significant effect beyond region 3. This is supported by the consideration of the frequency spectra and the base pressure coefficient. The use of the base pressure coefficient has already been discussed in subsection 3.1.4. Therefore, this experiment finds that the onset of vortex shedding appears to occur at a later stage compared to the DNW experiment.

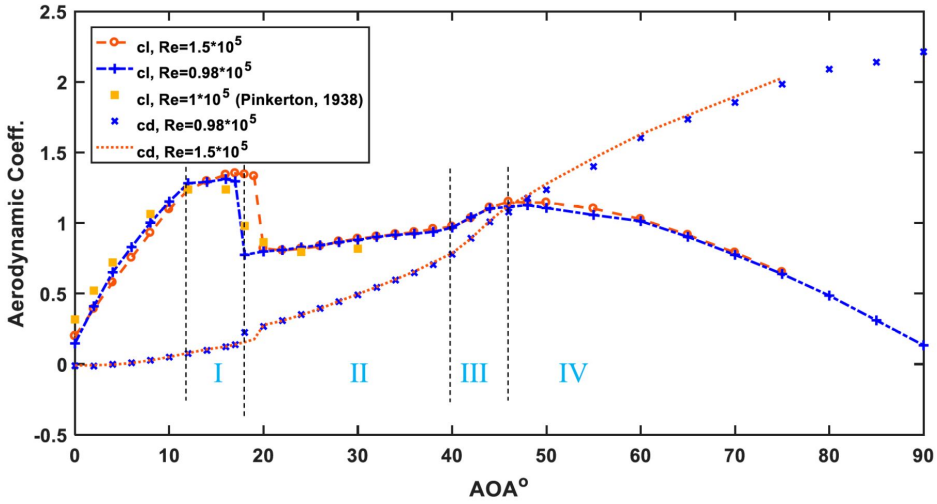

Figure 3.19: Polar from NACA 4412 airfoil as found by Fallahpour et al. [2022]

Secondly, the shedding frequency in terms of Strouhal number can be considered. It should be noted that the results have already been corrected for the blockage effect, using the same correction as was used for the DNW data. Therefore, this experiment can be used to compare the model results directly.

From Figure 3.20 it can be concluded that this experiment also shows a range of angles for which the projected Strouhal number approaches a constant value. In this case, the value is approximately 0.18, which is slightly higher compared to the other experiments. However, based on the considered literature, this is still a reasonable value. Additionally, it can be observed that the constant Strouhal number is obtained for larger angles of attack, where the vortex shedding has become dominant. In this case this behaviour takes place for angles larger than 40 degree. The areas in which the constant value of the projected Strouhal number is observed are also supported by the previously presented regions

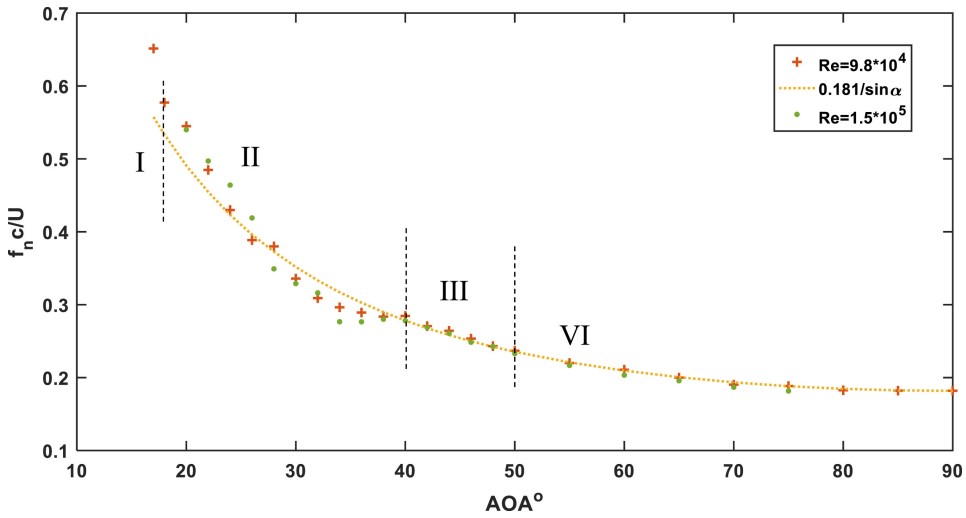

Figure 3.20: Strouhal number resulting from the experiment described by Fallahpour et al. [2022]

in which vortex shedding takes place.

3.4 Comparison of all experiments

At this stage three experiments have been described that consider the vortex shedding behaviour. These experiments can be compared in terms of the projected Strouhal number. It is expected that the shedding behaviour at large angles of attack approaches that of a flat plate, as discussed in chapter 2. Therefore, it would be expected that the results for all airfoils are similar. To investigate this the projected Strouhal numbers obtained in each of the experiments are shown in Figure 3.21. Additionally, a reference case of a flat plate is also included Fage et al. [1927].

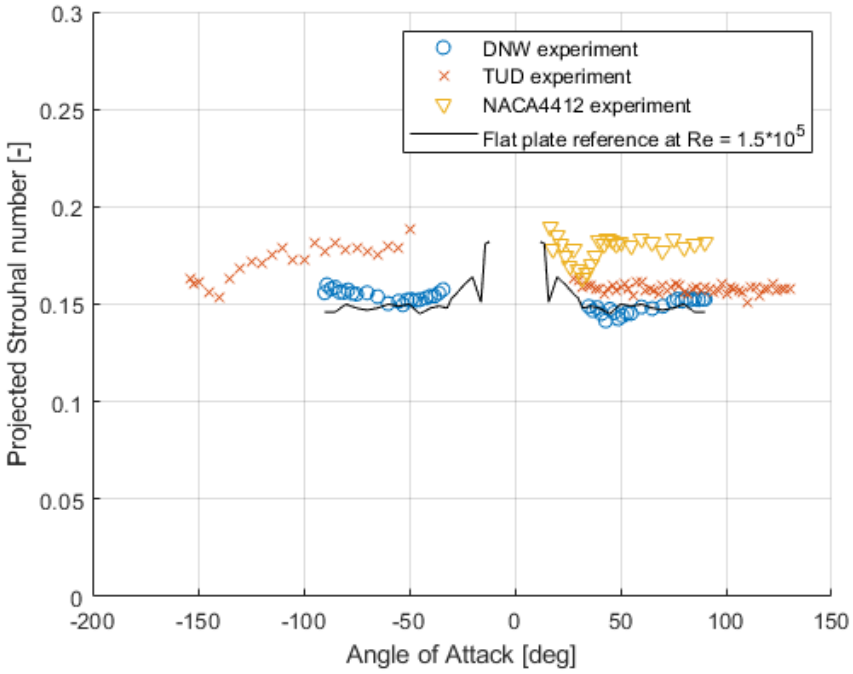

Figure 3.21: Comparison of Strouhal number between experiments

Firstly, the different experiments do provide somewhat different results. All experiments provide relatively constant projected Strouhal numbers between values of 0.15 and 0.18 for all angles. However, each experiment still shows a different result compared to the others. This suggests that the airfoil shape does have some effect on the frequency that is produced by the vortex shedding.

However, it should be considered that other factors could also have affected the results. For example the use of different wind tunnels, equipment or processing methods could have been of influence on the results. Nevertheless, it could be interesting to further investigate which aspect of the airfoil shape is the most influential for the observed differences. However, this considered to be outside the scope of the current research.

A second major observation is the asymmetry in the results. This once again indicates that the airfoil shape has an influence of the shedding behaviour. The experiment performed by TU Delft shows especially asymmetric behaviour. However, the DNW experiment also has slightly higher Strouhal numbers for negative angles of attack. The flat plate does show symmetric results in terms of vortex shedding, as it is a symmetric object. Therefore, the conclusion can be drawn that airfoils produces some asymmetry in the results. This could for example be caused by the camber.

Thirdly, the comparison between the experiments and the reference case of a flat plate can be considered. The DNW experiment very closely matches frequencies found in this reference case. However, the other airfoils show higher frequencies. This could further suggests that the shape of the airfoil is of some influence on the produced vortex shedding behaviour. An investigation into this observation could serve as another area for future research.

Chapter 4

Existing dynamic stall models for stationary airfoils in deep stall

In the previous chapter the vortex shedding results from three experiments. In this chapter these results are compared to several common dynamic stall models. In order to do this three models are first selected. Next, the method for determining the predicted shedding behaviour for the dynamic stall models is defined. After this, the predictions of the different stall models are compared to the experiments. Finally, based on this comparison, the critical elements of the dynamic stall model for predicting vortex shedding frequencies are established.

4.1 Selected dynamic stall models

In chapter 2 several dynamic stall models were outlined. The second order correction for each of these models takes a very similar form for many of the models. This is given by Equation 4.1.

$$\Delta\ddot{C}_{L,2} + c f_{21}\Delta\dot{C}_{L,2} + c f_{20}\Delta C_{L,2} = f t_2 \tag{4.1}$$

Since each of the models takes a similar approach to solving the second order correction, the main difference between them is the values of the coefficients. To investigate these effects three dynamic stall models were selected to be investigated. The only higher order model that is excluded from the analysis is ONERA model, as it included a significant number of airfoil dependent parameters. This is deemed to be undesirable at this stage to allow for a more direct comparison between the different experiments. The three other models, by Snel (Truong [1993b]), Adema (Adema et al. [2020]), and Bangga (Bangga et al. [2020]) were implemented and their implementation verified. The model presented by Bangga is typically referred to as the IAG model in this report. This process is documented in chapter B.

4.2 Extraction frequencies

Using the different implementations, the response of each of the models at a stationary angle of attack can be considered. The main parameter of interest of this process is the produced vortex shedding frequency. To extract the frequencies from the simulation results, the Fourier transform will be used. This is a similar approach to the one used for the extraction of the frequencies from the experimental results. However, the results from the simulation results have different characteristics compared to the experimental data. As there is no turbulence or other disturbances, the signal of dynamic stall model tends to contain one clear dominant frequency. The experimental signal showed a variety of frequencies present in the frequency domain as was discussed in the previous chapter. Additionally, the response is not guaranteed to be periodic. Therefore, a method has to be described for extracting the dominant frequency.

As discussed in some cases, the response might be significantly damped, an example of which is shown in Figure 4.1. This is the result of the damping coefficient used in the dynamic stall model. In this case, the dynamic response is reduced to a near constant value of after a couple of seconds. These sort of responses do still contain a dominant frequency. However, for the purposes of modelling the vortex shedding behaviour, these do not provide a suitable response as vortex shedding is a continuous process. Therefore, in order to exclude this type of response, only the second half of the 5 second response signal is considered when the frequency spectrum is constructed. This eliminates any quickly damped responses, while maintaining a sufficiently large range of data to extract the dominant frequency.

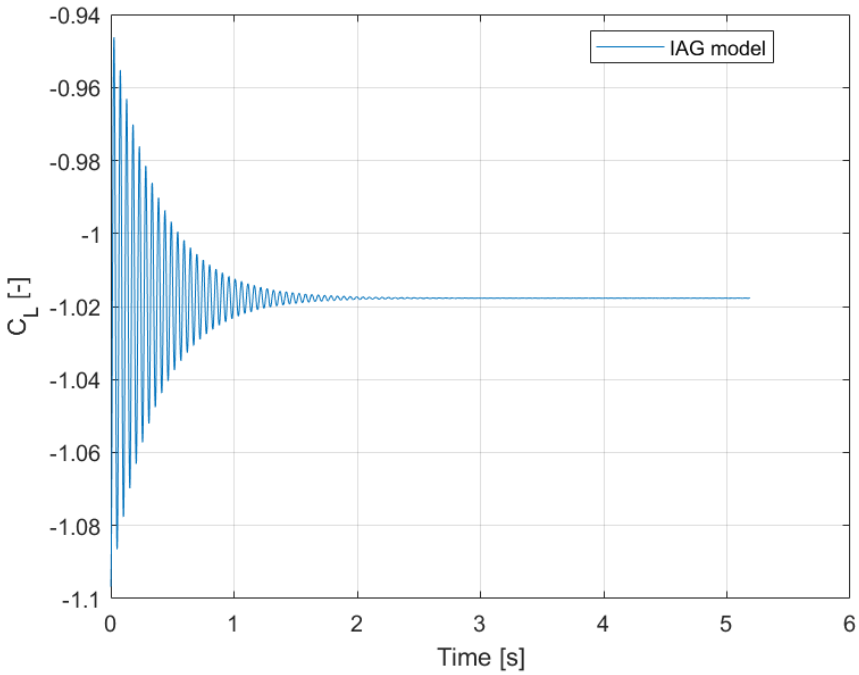

Figure 4.1: Example of a damped response of the dynamic stall model, IAG model applied to a stationary DU-00-W-212 airfoil at -38 degrees

Another step that has to taken for extracting the dominant frequency is the selection

of the peaks from the frequency spectrum. For this step it is important that the selected peaks are significant. As an example for the signal shown before, the frequency response for considering both the full and second half of the response is considered by showing the FFT of the signal of both cases.

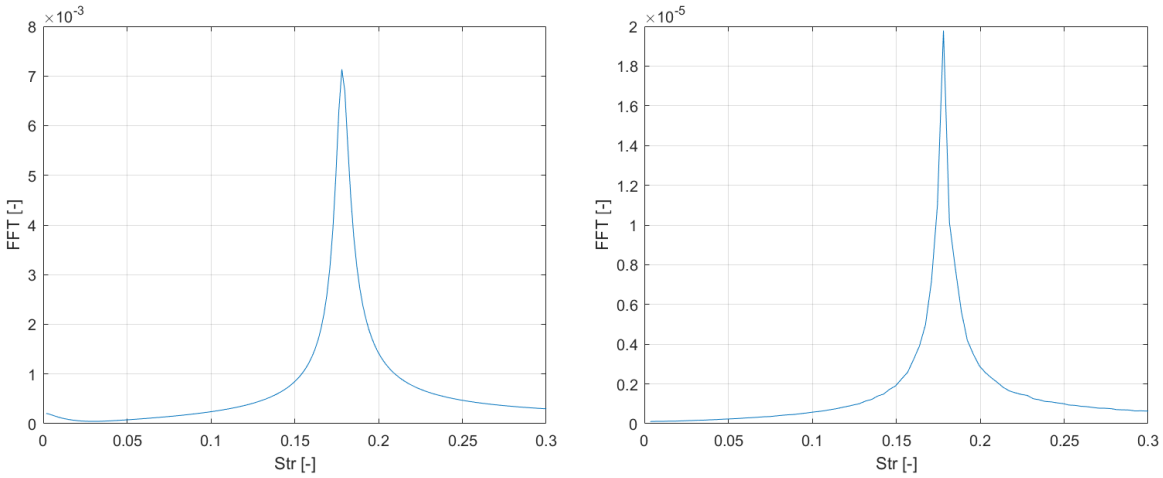

(a) Frequency response considering the full signal

(b) Frequency response considering the second half of the signal

Figure 4.2: Effect of the window considered in the determination of the frequency response

In the images above it can be observed that the location of the peak in frequency response is identical in both cases. However, when only the second half of the signal is considered the magnitude of the peak is significantly, about two orders of magnitude, smaller. This is to be expected and can be used to eliminate damped signals from the response. For this purpose, the peak has to reach a minimum magnitude before being considered for the shedding frequency. After some iterations, the parameters chosen for the peak selection were as follows, considering the second half of the response, a minimum peak height of 0.0001 should be obtained in the frequency domain. Since the signal used the lift coefficient, this magnitude is already normalised and this can be applied to all cases.

4.3 Common dynamic stall models for stationary airfoils

With the method described so far in this section, the vortex shedding frequencies of the dynamic stall models can be extracted. Therefore, the dynamic stall models can be compared to the data obtained from the stationary airfoils in the previously described experiments. It should be noted that the dynamic stall models are only compared to the DNW and TU Delft experiments in this section. With both of these experiments, the angles covered in the third experiment are already simulated. Therefore, the final experiment is excluded from this section as little additional information could be obtained from that comparison.

4.3.1 Vortex shedding predictions of the Snel model

In Figure 4.3, the frequency peaks that result from the original Snel dynamic stall model are compared to the experiments. Additionally, the reference case of a flat plate is included,

Fage et al. [1927]. As is clear from the image, no frequency peaks were found for this dynamic stall model. This is the result of all responses being heavily damped. An example of such a response is shown in Figure 4.4.

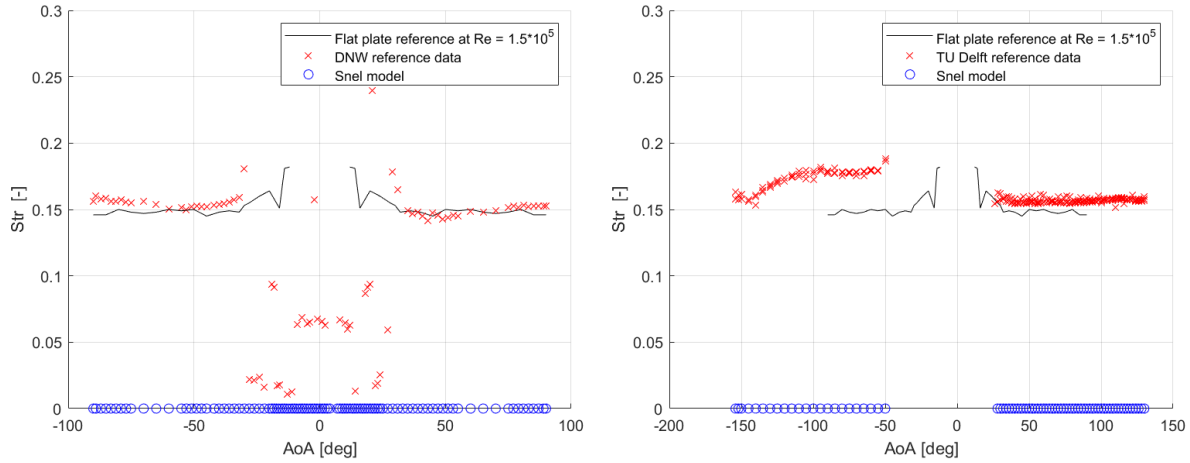

(a) Projected Strouhal number predicted by Snel model compared to DNW experiment

(b) Projected Strouhal number predicted by Snel model compared to TU experiment

Figure 4.3: Frequency response Snel model compared to both experiments

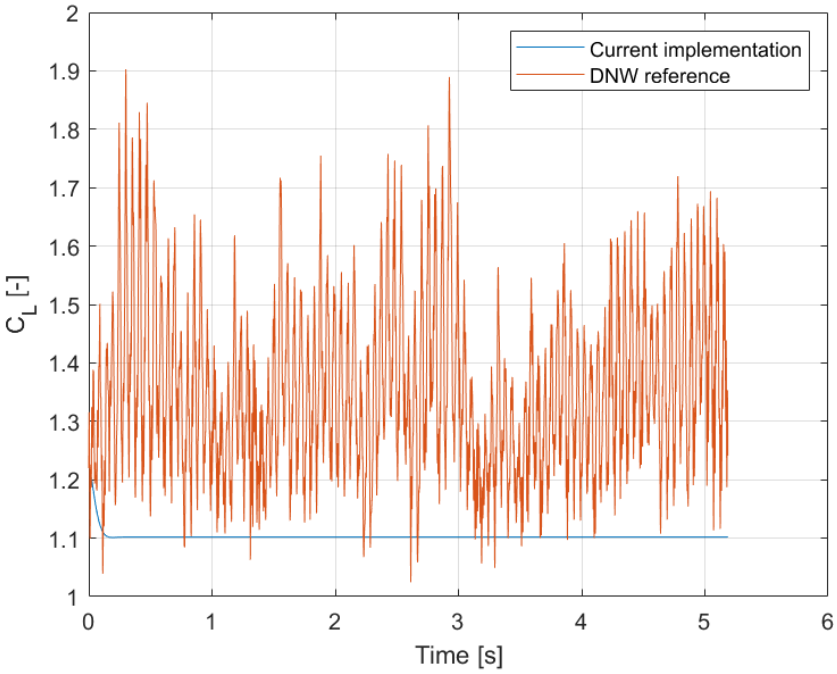

Figure 4.4: Time response comparison at 41 degrees of base Snel model and DNW experiment

4.3.2 Vortex shedding predictions of the Adema model

In Figure 4.5a and Figure 4.5b, the dominant projected Strouhal numbers that result from the Adema model are compared to the experimental results. This model does show shed-

ding frequencies at positive angles of attack, as the resulting signal does not get damped as significantly. However, the frequencies that result from the dynamic stall model are significantly lower compared to the ones from the experiment for most angles. Additionally, the variation with angle of attack is larger in the simulation results compared to the experimental values. Another major observation is while shedding frequencies are found for positive angles of attack, these are not observed for the negative angles. From the experimental results it is expected that the negative angles of attack also contain vortex shedding.

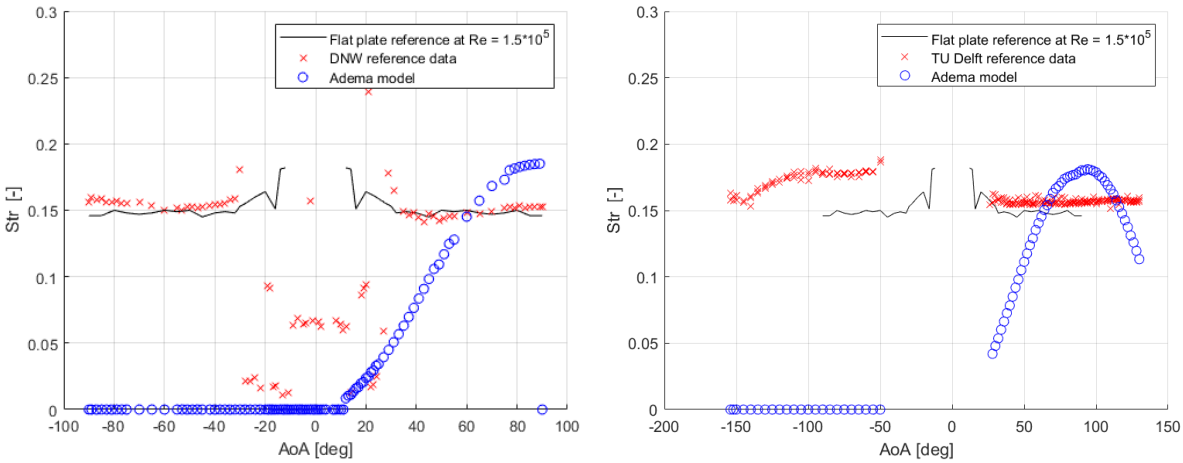

(a) Projected Strouhal numbers of Adema model compared to DNW experiment

(b) Projected Strouhal numbers of Adema model compared to TU Delft experiment

Figure 4.5: Frequency response Adema model compared to both experiments

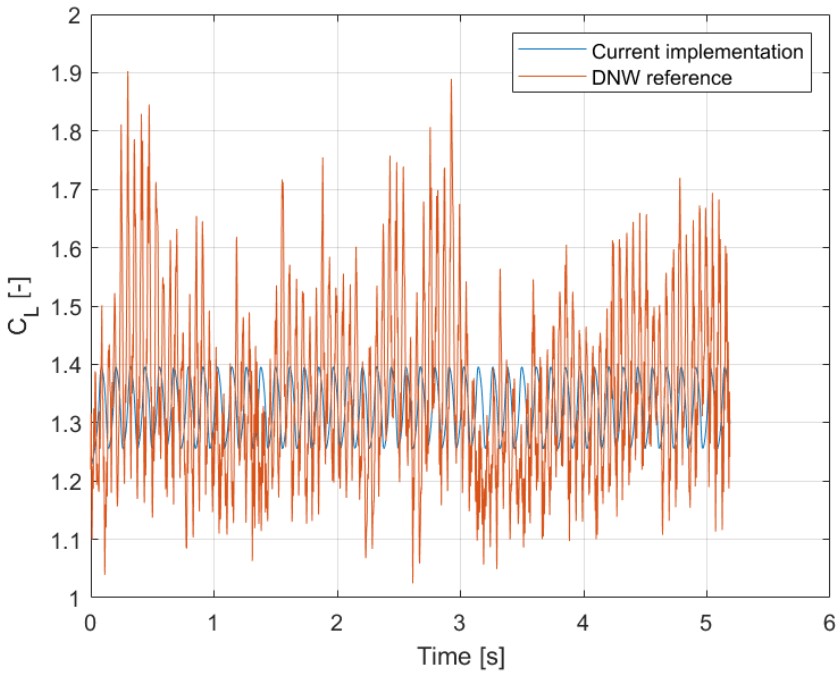

Figure 4.6: Time response comparison at 41 degrees of Adema model and DNW experiment

4.3.3 Vortex shedding prediction of the IAG model

The third model that is considered is the IAG model. This model uses a similar method for the second order correction s the other two considered model. In the two previous models the results varied greatly based on the coefficients used in the equations. This is once again the case for this final model. The values of the coefficients used in the differential equation cannot directly be compared to the other models, as the equations are non-dimensionalised. This was done by considering a normalised version of the time, as was discussed in section 2.3. However, the coefficients are different even when this is accounted for and thus the results are different as well. The comparison of the shedding frequencies for the IAG model to both the DNW and TU Delft experiment is shown in Figure 4.7a and Figure 4.7b.

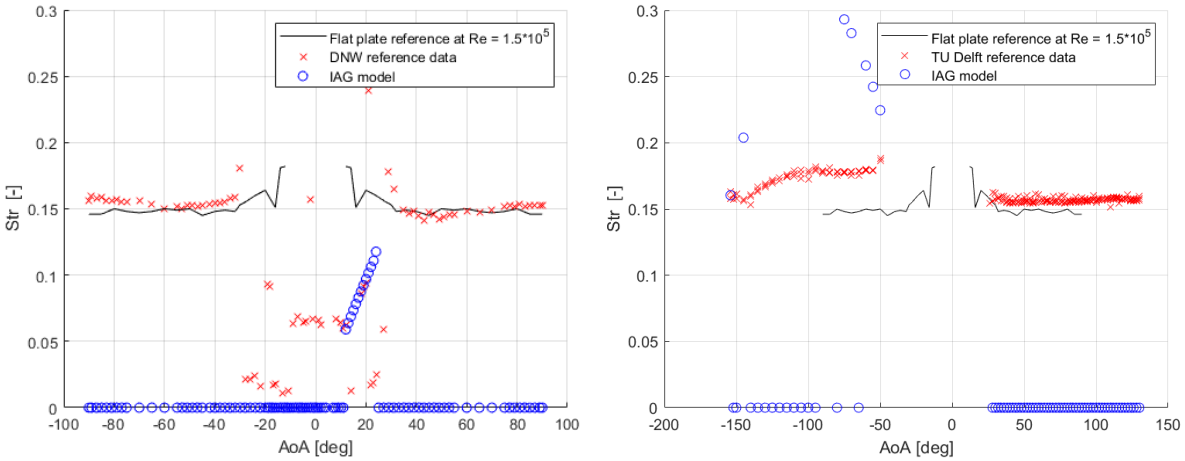

(a) Projected Strouhal numbers from IAG model compared to DNW experiment

(b) Projected Strouhal numbers IAG model compared to TU Delft experiment

Figure 4.7: Frequency response IAG model results compared to both experiments

Once again many angles of attack do not produce a periodic vortex shedding response. This is the result of the damping definition used in the model. It is interesting to briefly investigate the different damping effects that are present in this model and their effects on the response. As was shown for the Snel model, the damping can be very strong, almost representing a critically damped response. The frequencies shown in the image above would suggest a similar response. However, this is not the case. For the IAG model there can be an oscillating response at the start for some angles of attack. This response is damped relatively quickly after a number of oscillations. Hence, the results are different compared to the Snel model despite both not producing the continuous oscillation that is expected. Interestingly, the IAG model has a different type of response depending on the angle of attack. For example, for negative angles of attack the responses tend to be a relatively quickly damped oscillation. However, for the positive case the oscillations are slowly damped at smaller angles and stronger or even critically at larger angles. Some examples of this behaviour are shown in Figure 4.8.

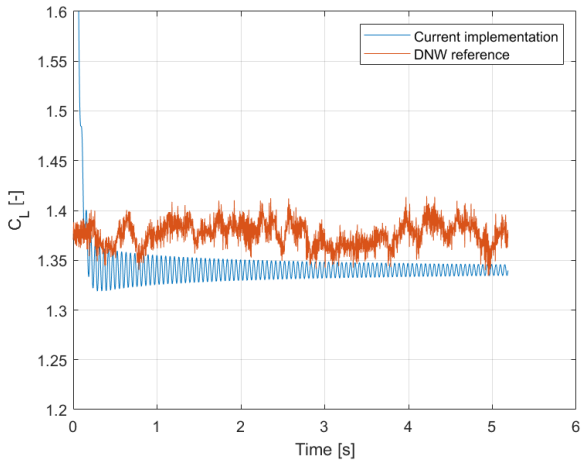

(a) IAG model response at 15 degrees

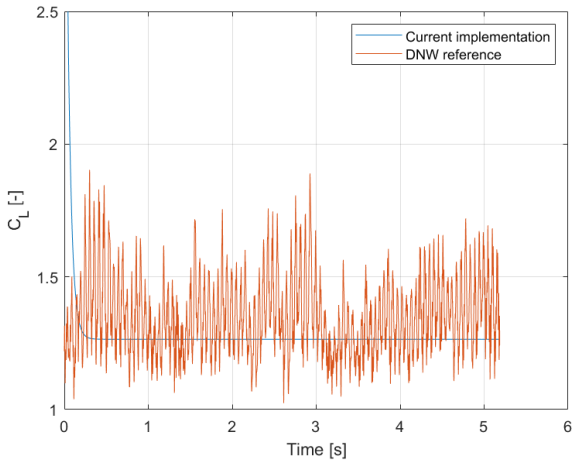

(b) IAG model response at 41 degrees

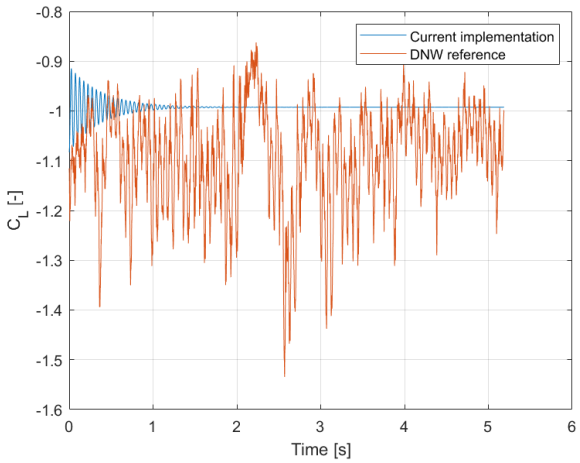

(c) IAG model response at -60 degrees

Figure 4.8: Different responses of the IAG model

It should also be noted that the speed at which oscillations are damped depends quite significantly on the operating condition. To demonstrate this, the frequency response can also be considered if only the first quarter of the response is excluded, Figure 4.9. The newly appeared frequencies indicate that these angles contain some oscillations at the start of the response, which are reduced significantly in time. These vast differences in types of responses between the different models does show that the selection of the model parameters can greatly affect the type of response that is obtained from the different models. This is an especially important realisation, as the second order correction of all models is governed by a similar differential equation.

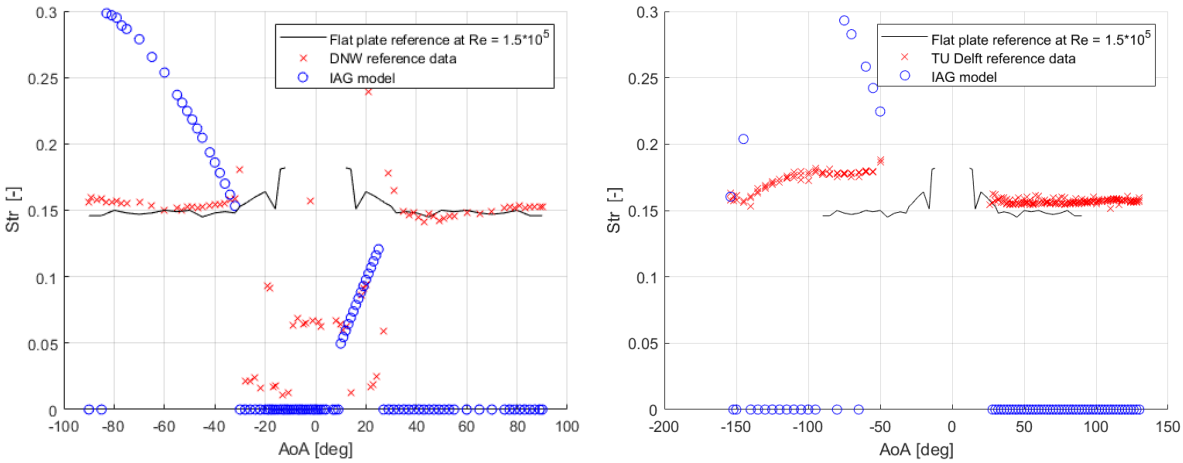

(a) Projected Strouhal numbers from IAG model compared to DNW experiment

(b) Projected Strouhal numbers from IAG model compared to TU Delft experiment

Figure 4.9: Frequency response IAG model results when only the first quarter of the signal is excluded

Observations dynamic stall models

In general, the dynamic stall models that are considered show large differences to the experimental data. There are several major differences that can be observed. The first is the fact that the experimental data looks vastly different in the time domain compared to the simulation results. This can partially be attributed to the fact that the experimental results contain a large number of frequencies, also lower frequencies, whereas the simulation results contains a small number of frequencies. Additionally, the amplitudes of the variations are also different. As a result, the comparison between the two results shows large discrepancies. This is expected to be the result of the dynamic stall models being designed to model the shedding effects on a dynamic airfoil. Therefore, the periodicity of the continuous vortex shedding behaviour cannot expected to be modelled accurately. Additionally, one should consider that the experimental responses also contain other sources of unsteadiness such the turbulence of the tunnel.

Secondly, the average of the oscillations can be analysed as well. In the case of the original Snel model this steady state value varies greatly compared to the experimental results. The Adema and IAG model do not suffer as greatly from this problem in the considered cases.

Next, there are many angles of attack for which all models do not create a periodic response. This is especially problematic for the larger angles of attack. The reason for the lack of a periodic response is the definition of the model parameters. These are defined such that they contain too much damping for continuous oscillations to occur. In fact, the original Snel definition contains such a large amount of damping that the response is immediately damped. This suggests that the proposed definition of the damping in the differential equation is not suitable for modelling the periodic response of the vortex shedding behaviour.

The Adema model does obtain a periodic response for larger positive angles of attack. However, for negative angles this behaviour is not observed. This is the result of the parameters in the equation varying with the angle of attack. The most important term for this observation is the $\Delta C_{L,pot}$ term, which defines the difference between the static and po-

tential coefficients. In the creation of this model only positive angles of attack were used. Hence, only positive differences were considered. This term changes sign for negative angles of attack, which affects the coefficients used in the differential equation. From the definition, it is observed that this change in sign alters the variation of the damping with angle of attack. As a result, the damping is too strong for negative angles and no periodic response is produced.

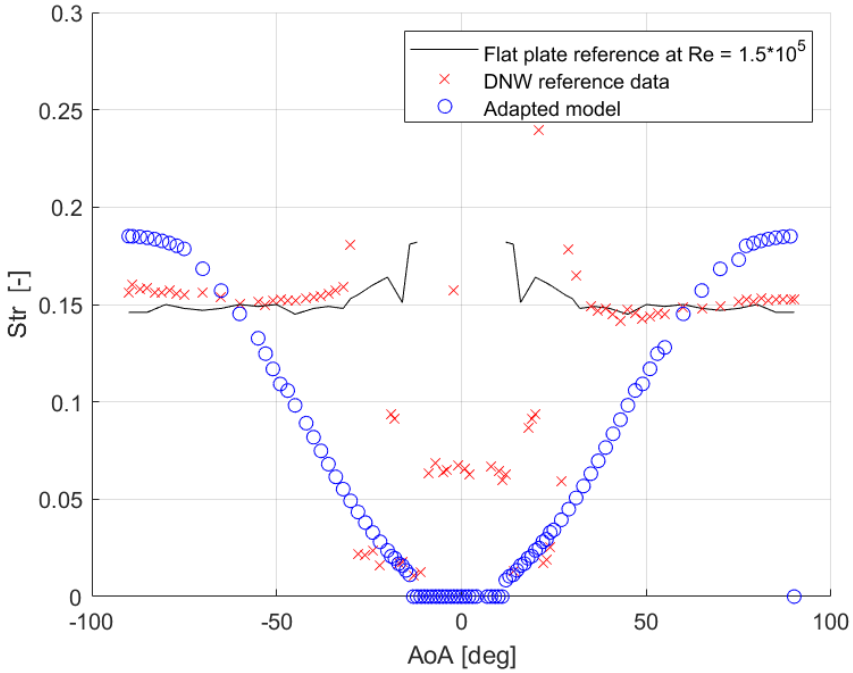

Figure 4.10: Projected Strouhal numbers predicted by Adema model if absolute value is taken for $\Delta C_{L,pot}$

Figure 4.10 shows the variation of the Strouhal numbers resulting from the Adema model with one adaptation. This adaptation is to take the absolute value of the original definition of the $\Delta C_{L,pot}$ term. This simple change already allowed for shedding frequencies to be produced at negative angles of attack. Additionally, this change can be supported by the fact that the $\Delta C_{L,pot}$ term is typically used to define the size of each of damping and forcing term of the differential equations. Since typically only positive angles are consdired in the creation of dynamic stall models, this change allows for the forcing to remain present even if the sign is altered.

The IAG model showed a damped response to the considered operating conditions. This means that this model does contain too much damping to accurately represent the periodic response. However, the frequencies that are observed in this response are significantly higher compared to the Adema model. This is mostly the result of the $c f_{20}$ term being differently defined in each model. The higher frequencies are required at lower angles of attack in order to better match the results from the experiments. Therefore, some inspiration can be taken from this model in terms of the magnitude of the model coefficients.

Based on the described observations the first steps towards a model for predicting the shedding frequencies can be taken. Firstly, the Adema model is selected as a starting point, as this model shows periodic responses for a large number of angles of attack. Additionally,

the periodic behaviour is not damped significantly over time. It has also been observed that the projected Strouhal number predicted by the dynamic stall models, if a periodic response is created at all, varies rapidly with angle of attack. This behaviour is different from that observed in the experiments and other literature. Therefore, the removal of this variation with angle of attack should be a main focus of the adaptations of the model. Finally, changes to the magnitude of the frequency coefficient in the differential equation can be used to effectively alter the vortex shedding frequencies predicted by the model. These observations will be used in the next chapter to produce an adapted dynamic stall model for the prediction of vortex shedding.

4.3.4 Effect of Reynolds number

In the TU Delft experiment a number of Reynolds numbers were considered. From the results it was concluded that the effect of the Reynolds number was minimal on the vortex shedding frequency. To investigate if this is also the case in the dynamic stall models the same Reynolds numbers were considered.

When the Adema model is applied to these different Reynolds numbers the results also show little variation. This is visually represented by Figure 4.11. Therefore, the Adema model is shown to have no strong dependency on the Reynolds number. This is similar behaviour to what is observed in the experiment. The observation that both the experiment and dynamic stall model show no strong correlation with Reynolds number is supportive of the method being applied in a more general sense. However, it should be noted that the variation of the Reynolds number is limited in this experiment. Therefore, to be certain of this result a larger variety of Reynolds numbers should be considered.

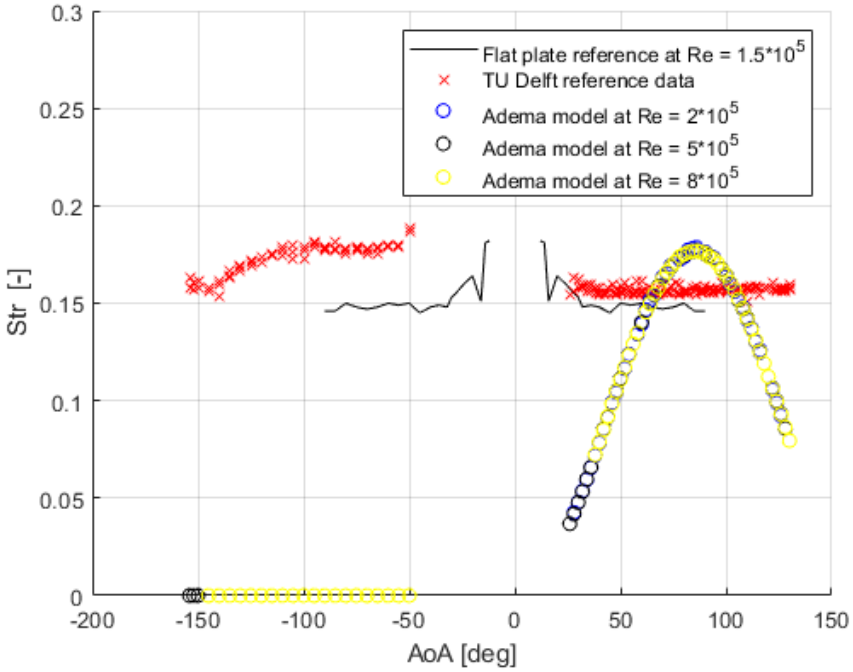

Figure 4.11: Effect of Reynolds number on the vortex shedding frequencies of the Adema model

Chapter 5

Development adapted model for vortex shedding frequencies

As was shown in the previous chapter, the current dynamic stall models are not suitable for predicting the vortex shedding frequencies produced by stationary airfoils. Therefore, A new model is proposed in this chapter. First, changes are made to the Adema model to better predict the shedding frequencies for large angles of attack in section 5.1. Next, the effect these changes have on the time domain results for both stationary and pitching airfoils is explored in section 5.2. Based on these observations an adapted version of the Adema model is proposed. Finally, the accuracy of this adapted model is compared to different dynamic stall models in section 5.3.

5.1 Adapted model for stationary airfoils

Based on the observations made in the previous chapter, changes can be proposed to predict the shedding frequencies using an adapted dynamic stall model. In this section some structural changes to the model are explored. First, the definition is adapted for the large angles of attack at which the vortex shedding behaviour occurs. Next, the definition of the coefficients is considered to devise a method for adapting the terms. Finally, some changes are proposed to the Adema model to improve the prediction of the shedding frequency.

5.1.1 Adapting definitions for deep stall angles

The first step in adapting the Adema model for vortex shedding predictions is to change the definition of the potential lift. This is required as the current definition is based on a small angle assumption. Therefore, the $\Delta C_{N,pot}$ in the models has to be updated to be suitable for the large angles of attack associated with deep stall conditions.

This term is originally defined as shown in Equation 5.1. Based on this definition, the potential difference keeps increasing indefinitely with angle of attack. This results is based on a linearisation using the small angle assumption. However, it would be expected that a maximum would be reached after the airfoil is rotated vertically. This could for example be observed in the results of the TU Delft experiment, section 3.2. In these results, the shedding frequencies show a clear minimum when the airfoil is placed perpendicular to

the flow. The behaviour can be replicated by removing the mentioned assumption of small angles.

$$\Delta C_{N,pot} = C_{N,\alpha}(\alpha - \alpha_0) - C_{N,steady} \tag{5.1}$$

The linear relation in Equation 5.1 is the results of the definition lift based on potential theory. In this theory, the formulation of the lift is obtained through a small angle assumption. However, this assumption is not valid at the operating conditions considered at this stage. Therefore, the small angle assumption has to be removed from the potential lift definition. The resulting equation is shown in Equation 5.2.

$$\Delta C_{N,pot} = C_{N,\alpha} sin(\alpha - \alpha_0) - C_{N,steady} \tag{5.2}$$

Based on this new definition of the potential lift curve, the difference between the steady polar and the potential does not keep increasing with angle of attack. This is shown by Figure 5.1, where the two are compared to the steady polars of the DNW and TU Delft experiment.

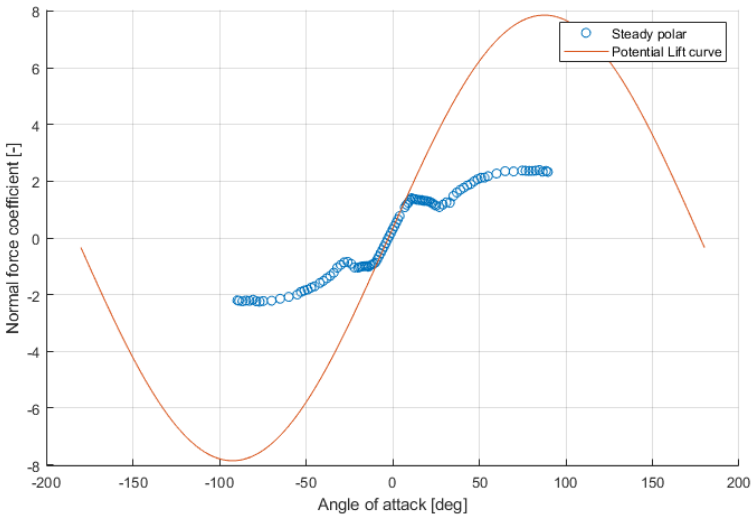

(a) DNW polar comparison

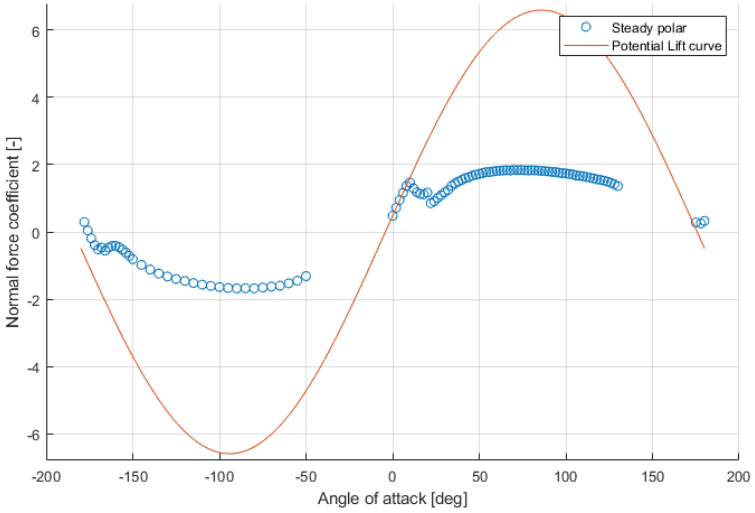

(b) TU polar comparison

Figure 5.1: Comparison of steady polars to newly defined potential for both experiments

Next, the effect of this change has on the shedding frequencies produced by the Adema model is examined. This is done by considering the Adema result for the TU Delft experiment, as this experiment has the largest range of angles of attack. The results are shown in Figure 5.2.

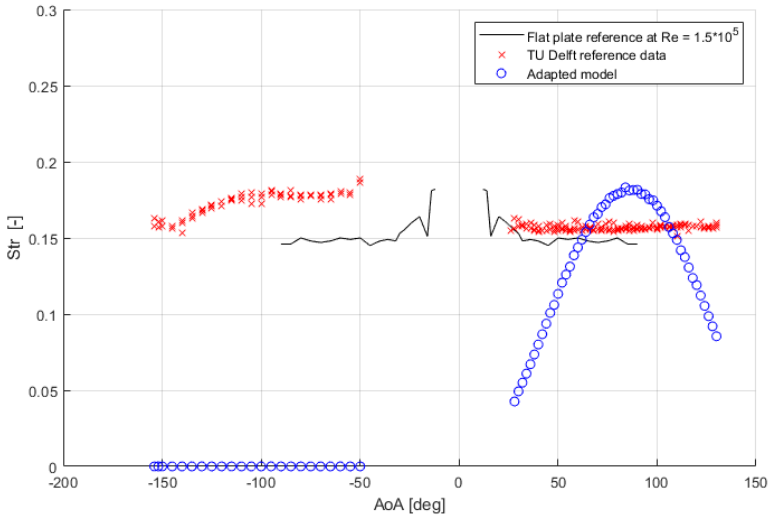

(a) Projected Strouhal numbers Adema model original potential

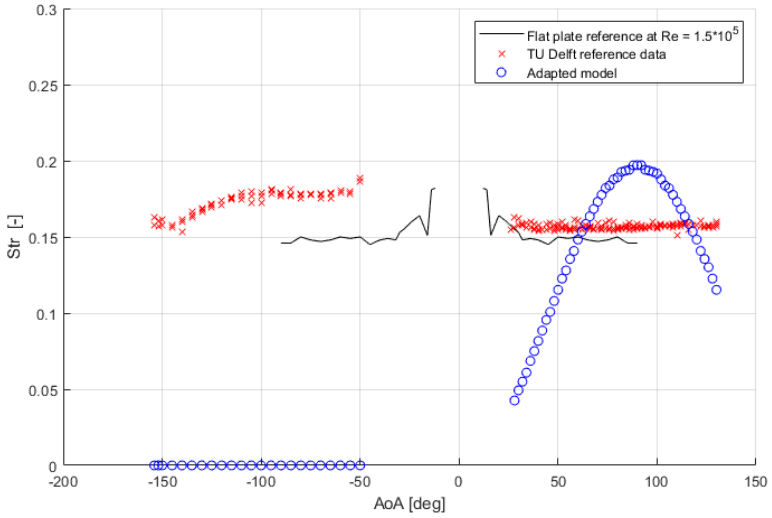

(b) Projected Strouhal numbers Adema model new potential

Figure 5.2: Effect of newly defined potential loading on shedding frequencies

In Figure 5.2, the effect of the newly defined potential normal force can be clearly observed. At the large positive angles of attack the frequency decreases far less rapidly. This is the result of the forcing term no longer increasing these angles of attack. Hence, the results from the adapted model already approach the results of the experiment more closely for these large angles.

At around 90 degrees, it can also be observed that the predicted shedding frequency has increased slightly. This is the result of the potential difference being smaller at this point compared to the linear definition used earlier. This change in the results is something that should be adjusted for at a later stage in the model development.

5.1.2 Identifying potential adaptations of the model coefficients

Apart from changing the definition of the potential term in the equations, the other contributions to the coefficients could also be adapted. To get in indication of the potential changes that could be made, the equations that contribute to the shedding behaviour are shown below.

$$\tau^2 \frac{d^2 \Delta C_{l,2}}{dt^2} + cf_{21} \frac{d\Delta C_{l,2}}{dt} + cf_{20} \Delta C_{l,2} = ft_2 \tag{5.3}$$

$$ft_2 = 0.01 k_s \left(-0.04 \Delta C_{l,pot} + 1.5\tau \frac{d\Delta C_{l,pot}}{dt} \right) \tag{5.4}$$

$$cf_{20} = 10(k_s sin(\alpha))^2 \left(1 + 3\Delta C_{l,2}^2\right) \left(1 + 280^2 \tau^2 \left[\frac{d\alpha}{dt}\right]^2\right) \tag{5.5}$$

$$cf_{21} = \begin{cases} 60\tau k_s \left(-0.01(\Delta C_{l,pot} - 0.5) + 2\Delta C_{l,2}^2 \right) & \text{if } \frac{d\alpha}{dt} > 0 \\ 60\tau k_s \left(-0.01(\Delta C_{l,pot} - 0.5) + 14\Delta C_{l,2}^2 \right) & \text{if } \frac{d\alpha}{dt} \leq 0 \end{cases} \tag{5.6}$$

In order to get an impression of the frequency that result from this approach one can consider the general form of such a differential equations, Equation 5.7. The solution to this differential equation can have many different forms depending on the values of the coefficients. It should be noted that the equation presented here is not linear as $C_{l,2}$ is also included in the Γ and ω terms. However, this general case can still be used to give an indication on how the coefficients should be adapted to obtain the desired result.

$$\frac{d^2 \Delta C_{l,2}}{dt^2} + 2\Gamma \frac{d\Delta C_{l,2}}{dt} + \omega^2 \Delta C_{l,2} = F \tag{5.7}$$

For the equation Equation 5.7, several different types of solutions exist based on the ratio between the damping and frequency term, Γ and ω. However, for the currently considered case only the underdamped case is of importance, as the goal is to obtain a solution that continues indefinitely in time. This is required in order to mimic the behaviour observed in vortex shedding. In this case, the frequency of the response case can be defined as $\Omega = \sqrt{\omega^2 - \Gamma^2}$. This definition will be used as an first indication for how to adapt the coefficients. For example, if the frequencies at high angles of attack should be increased, the contribution of the $\Delta C_{l,pot}$ could be decreased. This change would reduce the damping at angles where the potential difference is larger. Additionally, at smaller angles of attack the change would have a less effect as the potential difference is smaller. This approach will be used in the next section in order to obtain an adapted version of the Adema model that is able to better predict the vortex shedding frequencies.

5.1.3 Adapting the Adema model

As discussed in chapter 4, the relative magnitudes of the cf_{20} and cf_{21} coefficients are critical in determining the type of response. Hence, the adaptations presented in this section are applied to these aspects of the dynamic stall model. The forcing term is ignored as it did

not have any significant effect on the shedding frequencies predicted for a stationary airfoil. Several adaptations were considered in the development of this model. The selected definition is presented in this section, while an alternative option is outlined in appendix C.

The presented adaptation aims to generate an airfoil specific response for each of the experiments, based on the differences in their steady polars. This is desired as the different experiments show different vortex shedding frequencies as was discussed in chapter 3. To try and accomplish this, a set of adaptations is proposed in this section. These adaptations aim to improve the prediction of the vortex shedding frequency through the method presented in the previous section.

The first major contribution the is considered is the cf_{21} definition. The goals of the changes to this parameter were to reduce the variation of the response with angle of attack and allow for periodic responses at negative angles. To achieve this, the definition is separated into low and high angles of attack. With high angles of attack referring to angles which place to airfoil almost perpendicular to the flow direction. For these angles the potential difference will be at a maximum. This division is represented by the α_s parameter in the equations. In this section, the value of this parameter was set to 25 degrees to be able to show the effects on the vortex shedding predictions. The definition of this parameter is considered in more detail in the next section.

First, the cf_{21} is adapted by the introduction of the square on the $\Delta C_{l,pot}$ contribution. This adaptation aims to accomplish two things. Firstly, the square removes the change in sign for negative angles. Hence, it allows for periodic responses at negative angles. Secondly, the application of the square reduces the variation in projected Strouhal number with angle of attack. The reason for this is the relative larger value of $\Delta C_{l,pot}$ at large angles compared to the lower angles. The square further reduces the frequencies at large angles, while having a much less significant impact on the smaller angles of attack. For these angles the potential difference is relatively small. This results in an overall reduction in the variation of the vortex shedding frequency with angle of attack.

The second adaptation also relates to the $\Delta C_{l,pot}$ definition. The absolute value of this parameter is used in the adapted model. This was done to allow for periodic responses also at angles that are placed below the separation of high and low angles of attack.

Finally, one numerical value was adapted in the definition. This was done to better match the slightly asymmetric results that were observed in the experiments. The changes to the equations of cf_{21} are presented in Equation 5.8 and Equation 5.9.

$$cf_{21} = \begin{cases} 60\tau k_s \left(-0.01(\Delta C_{l,pot} - 0.5) + 2\Delta C_{l,2}^2\right) & \text{if } \frac{d\alpha}{dt} > 0 \\ 60\tau k_s \left(-0.01(\Delta C_{l,pot} - 0.5) + 14\Delta C_{l,2}^2\right) & \text{if } \frac{d\alpha}{dt} \leq 0 \end{cases} \tag{5.8}$$

$$\Downarrow$$

$$cf_{21} = \begin{cases} 60\tau k_s \left(-0.01(|\Delta C_{l,pot}| + 0.25)^2 + 2\Delta C_{l,2}^2\right) & \text{if } \frac{d\alpha}{dt} > 0 \;\&\; \alpha > \alpha_s \\ 60\tau k_s \left(-0.01(|\Delta C_{l,pot}| - 0.5) + 2\Delta C_{l,2}^2\right) & \text{if } \frac{d\alpha}{dt} > 0 \;\&\; \alpha < \alpha_s \\ 60\tau k_s \left(-0.01(|\Delta C_{l,pot}| + 0.25)^2 + 14\Delta C_{l,2}^2\right) & \text{if } \frac{d\alpha}{dt} \leq 0 \;\&\; \alpha > \alpha_s \\ 60\tau k_s \left(-0.01(|\Delta C_{l,pot}| - 0.5) + 14\Delta C_{l,2}^2\right) & \text{if } \frac{d\alpha}{dt} \leq 0 \;\&\; \alpha < \alpha_s \end{cases} \tag{5.9}$$

Next, the frequency term, cf_{20}, is considered in the adaptation. For this term, two goals were established. Firstly, the variation of the shedding frequency with angle of attack had to be further reduced. Additionally, after obtaining a more constant range of shedding frequencies, this range should be centered around the expected projected Strouhal numbers.

The first change to the cf_{20} definition is the removal the $sin(\alpha)$ term. This is done with the goal of removing the variation of the projected Strouhal number with angle of attack.

After the removal $sin(\alpha)$ from the definition, some significant variation could still be observed in the projected Strouhal number. This variation appeared to be of a sinusoidal nature. Therefore, an additional term is introduced to cf_{20} at larger angles of attack. This term contains a division by $sin(\alpha)$ and as a result ensures a much more constant response in terms of projected Strouhal number. It should be noted that the introduction of this term could potentially cause instabilities. Therefore, it is only applied to the definition at larger angles of attack.

The resulting changes to the frequency coefficient are shown in Equation 5.10 and Equation 5.11.

$$cf_{20} = 10(k_s sin(\alpha))^2 \left(1 + 3\Delta C_{l,2}^2\right)\left(1 + 280^2\tau^2\left[\frac{d\alpha}{dt}\right]^2\right) \tag{5.10}$$

$$\Downarrow$$

$$cf_{20} = \begin{cases} 10(k_s sin(\alpha))^2 \left(1 + 3\Delta C_{l,2}^2\right)\left(1 + 280^2\tau^2\left[\frac{d\alpha}{dt}\right]^2\right) & \text{if } \alpha < \alpha_s \\ 10k_s^2 \left(1 + 3\Delta C_{l,2}^2\right)\left(1 + 280^2\tau^2\left[\frac{d\alpha}{dt}\right]^2\right) + \frac{0.125}{sin^2(\alpha)} & \text{if } \alpha \geq \alpha_s \end{cases} \tag{5.11}$$

In Figure 5.3, the effect that the discussed changes have had on the projected Strouhal number is examined for each of the experiments. The variation in the values with angle of attack is reduced significantly and the prediction of the vortex shedding frequency is improved. The different airfoils also do show a unique response. Therefore, it can be concluded that the goal of achieving a response that is airfoil specific has been achieved in this definition. Based on these results, the proposed set of adaptions will be used as the start of the adapted dynamic stall model for predicting vortex shedding frequencies.

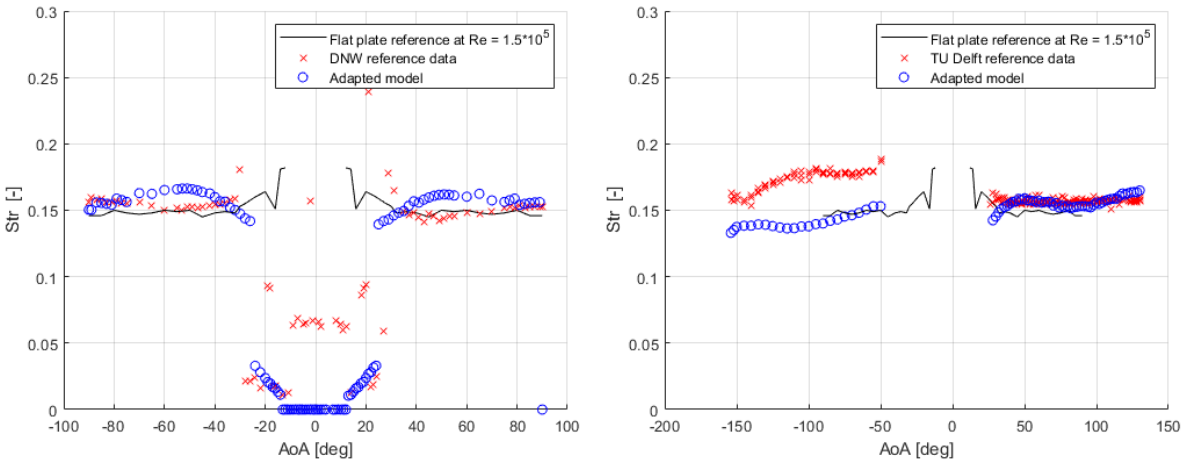

(a) DNW experiment

(b) TUD experiment

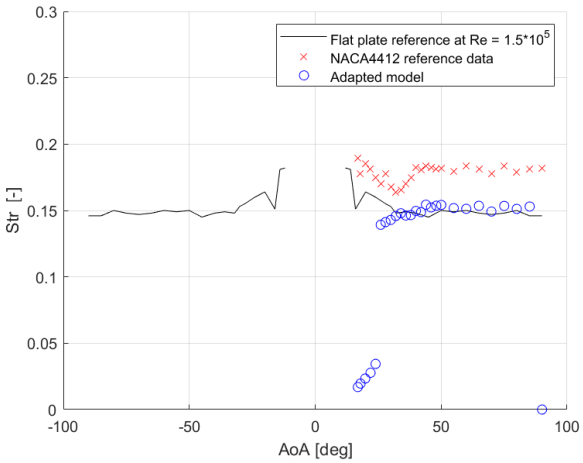

(c) NACA 4412 experiment

Figure 5.3: Shedding frequencies from the second option of the adapted model

5.1.4 Further considerations

Based on the changes made up to this point, there are several aspects that should be investigated before this model can be implemented. Firstly, the effect of these changes on the model response to more typical cases has to be considered. Currently, only the effect on the predicted vortex shedding frequencies was taken into account. However, dynamic stall models are typically applied to very different cases. These would consider more moderate angles of attack, below 30 degrees, with moving or pitching airfoils. For this purpose, a large amount of data is available. Therefore, the performance of the changed model will be examined for these conditions in section 5.2.

Additionally, the prediction of the time loading for stationary airfoils of this adapted model could be examined. The goal of this examination is to compare the magnitude of the oscillations that are introduced. For this purpose, the time resolved data from the DNW experiment can be used. This analysis should result in a better understanding of the effects of the proposed changes to the dynamic stall model in the time domain. The changes in the time domain are also presented in section 5.2.

Thirdly, the prediction of the shedding frequency can still be improved. To accomplish this a numerical optimisation is proposed. A potential optimisation method was introduced in chapter 2. The application of this approach to the proposed model is presented in chapter 6. The main reason for this optimisation is the fact that the numerical parameters present in the model definitions have not been considered in detail. In this section these were obtained through a trial and error process. Therefore, it is expected that a numerical optimisation could further improve the results. Additionally, this process can provide some information about the sensitivity of the proposed model. Since the applied changes are quite significant, the sensitivity of the model is an important consideration before more general application of the model can be considered.

5.2 Time domain results

In the previous section an adapted dynamic stall model was proposed to better predict the vortex shedding frequencies. However, the effect of these changes on the time-domain response is not considered. Additionally, the more typical application of dynamic stall models, pitching airfoils at moderate angles of attack, is also not included at this stage. To examine the effects in these areas of interest, the changes in the time response of a stationary airfoil are first considered in subsection 5.2.1. Secondly, the response of this new model to a time varying input is also examined in subsection 5.2.2. Based on these comparisons, some further adaptations are proposed. It should be noted that the previously introduced models contained a α_s parameter to remove instabilities from the definition. This parameter has been set to 1 degree in this section in order to examine the effect of the changes without limitations.

5.2.1 Shedding results adapted model in time

To consider the vortex shedding response in time, the time resolved data from the DNW experiment is used. This data is compared to both the original Adema formulation of the dynamic stall model and the adapted model from the previous chapter. In Figure 5.4, some selected comparisons are shown of the shedding response. It should be noted that only positive angles of attack were considered, as the original Adema formulation does not provide a periodic response for negative angles of attack.

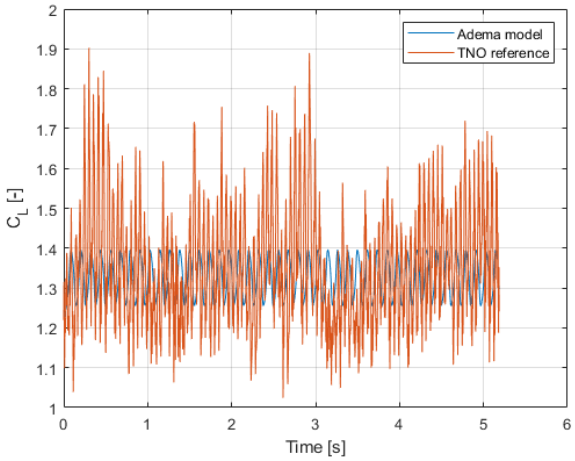

(a) Original Adema response at 41 degrees

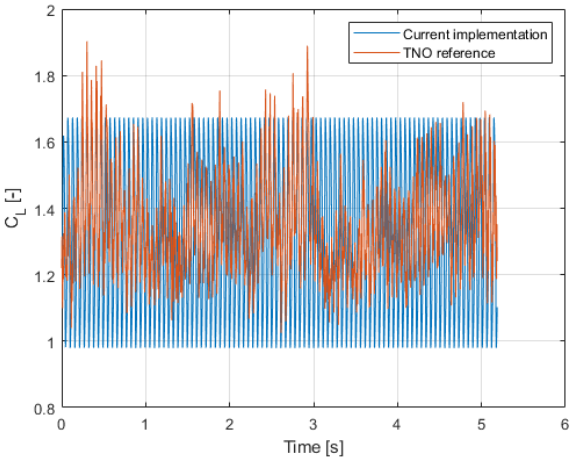

(b) Adapted model response at 41 degrees

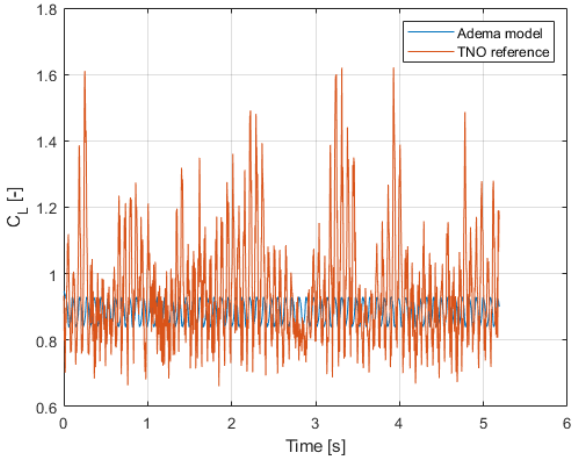

(c) Original Adema response at 70 degrees

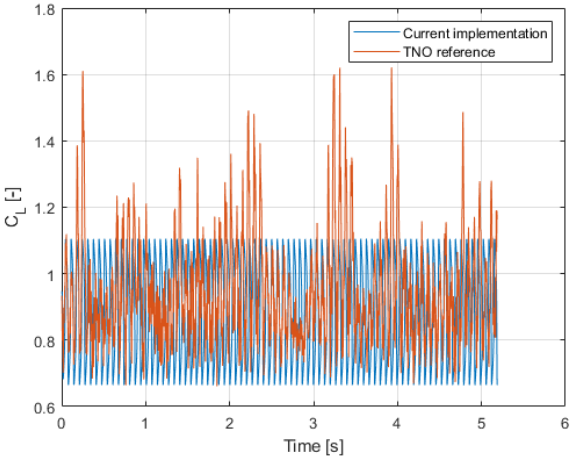

(d) Adapted model response at 70 degrees

Figure 5.4: Comparison of shedding response of new model in time

From the comparisons shown above it is clear that the magnitude of the oscillations were also greatly affected by the proposed changes. This is not something that could have been observed when the frequency response was considered in the previous section. The change is mostly the result from the adaptations to the damping parameter in the differential equation. However, it should be noted that this increase in oscillation size is not necessarily a problem. The variations in the experimental data are generally larger than the results produced by the Adema model. This is shown on the left side of Figure 5.4. Therefore, an increase in the variations is generally acceptable. However, for 41 degrees it seems that the fluctuations are larger than those observed in the experiment. This suggests that the damping might be altered too significantly for this inflow angle.

Another observation that can be made is the significant increase in the frequency of the responses. This is expected as the frequencies were generally increased at angles smaller than 90 degrees, Figure 5.3.

Thirdly, the oscillating responses of both models have identical averages. This is the case since the damping and frequency term in the equation do not affect the average of the response. The average of the displacement is governed by the forcing term, which is not

altered in this report. However, adapting this forcing term is another avenue that could be considered in future adaptations of the model.

5.2.2 Time responses for reference pitching airfoil cases

In the previous section the time response of a stationary airfoil using the new model was considered. However, dynamic stall models are most often applied to moving or pitching airfoils instead of stationary airfoils. Therefore, the response of the new model to such cases should also be considered. For this purpose, a significant amount of reference data is available. In this report the data is obtained from the OSU database. This dataset is chosen as it was also used to create the Adema model, Adema et al. [2020]. As a result, the newly adapted model can be easily compared to both the original Adema formulation and experimental results. Additionally, there is precedent for the use of this data set for the adaptation of dynamic stall models.

When the model as presented in the previous section is implemented the results vary greatly from the original Adema model. In Figure 5.5 the comparison to the original model and its reference data are shown for two cases. These specific cases use a NACA 4415 airfoil.

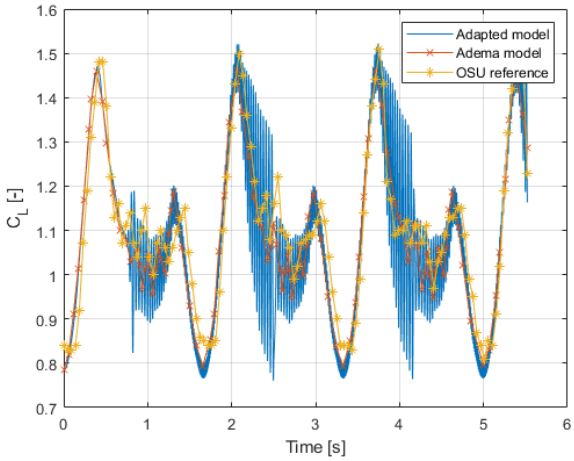

(a) Response of adapted model to k = 0.0228 with a mean α of 14^o and a variation of 10.5^o

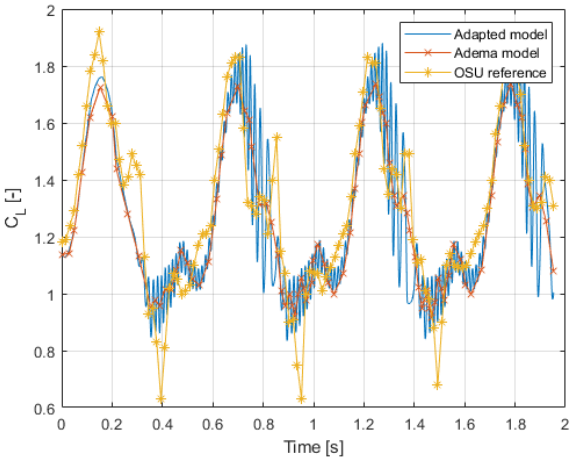

(b) Response of adapted model to k = 0.0711 with a mean α of 18.4^o and a variation of 10.7^o

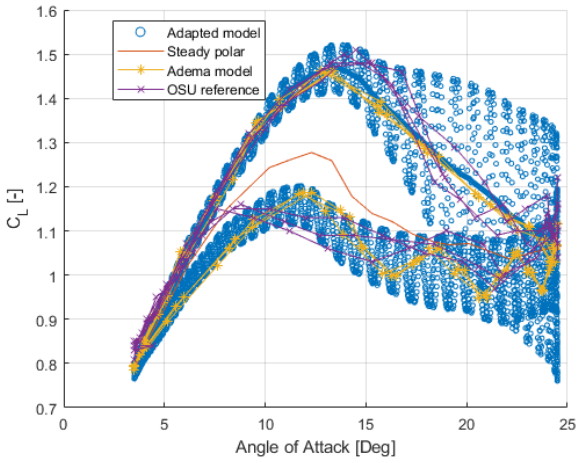

(c) Response of adapted model to k = 0.0228 with a mean α of 14^o and a variation of 10.5^o

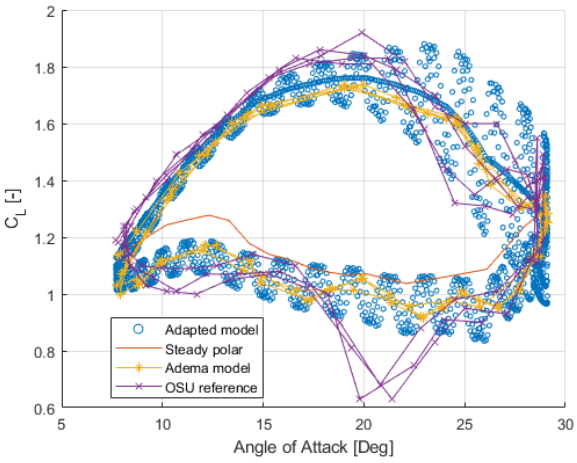

(d) Response of adapted model to k = 0.0711 with a mean α of 18.4^o and a variation of 10.7^o

Figure 5.5: Adapted model response to OSU reference conditions

When the results from the newly adapted model are compared to the original Adema model, many more oscillations are visible. These oscillations are the result of the changes to the frequency and damping terms of the dynamic stall model. The behaviour of this adapted model is more similar to the IAG model, as the oscillations produce different results for each cycle. Additionally, it can be observed that the oscillations have to develop as they increase rapidly in size as the angle of attack is increased.

Interestingly, the slower rotating airfoil experiences stronger oscillations in the response. This is likely caused by the forcing not varying as quickly and as such leaving time for the shedding effects to take over. The adapted model was changed to produce higher shedding frequencies at lower angles of attack. Hence, it can be observed that the oscillations in the adapted model response are relatively fast compared to both the Adema and experimental results. The high frequency in this response is the result of the changes that were made as for low angles of attack, where the shedding frequency had to be increased.

In Figure 5.5, two examples are shown of the proposed dynamic stall model applied to pitching airfoil cases. These comparisons clearly show that the changes in the model are

not suitable for predicting the dynamic stall behaviour for these conditions. Therefore, the model has to be further adapted in order to be applicable in a general sense. A proposed method for such adaptations will be explored next.

5.2.3 Adapting the vortex shedding model for pitching airfoil cases

Based on the observations in the time response, the adapted model provides oscillations that are too high in frequency and amplitude. This is especially clear at the end of the upstroke and start of the downstroke, Figure 5.5. Based on this, some term must be altered which allows for these oscillations to be damped more significantly. Additionally, the frequency term might also be adapted based on the angle of attack to allow for a more accurate modelling of the frequencies observed in the reference data.

Firstly, to consider the frequencies there appears to be a large difference between the frequencies occurring at lower angles of attack compared to the angles at which vortex shedding occurs. This was also observed in the experimental data of for example the DNW experiment. For this experiment, the higher range of Strouhal numbers only appeared for larger angles of attack. Since these frequencies are representative for the vortex shedding behaviour, it can be concluded that the frequencies in the response must increase with the onset of vortex shedding. Based on this observation, the frequency term might have to contain several definitions, one of which is selected based on the operating conditions that are experienced. The frequencies that are required to accurately predict the shedding frequencies that occur on an airfoil are generally much higher compared to the oscillations that were observed in the OSU references at moderate angles of attack.

In the definition of the model an additional angle α_s was introduced. This angle was meant to remove the singularity at zero introduced by the added term in the frequency coefficient. However, this angle can also be used to represent an angle at which the vortex shedding behaviour starts to become more significant. In this report this angle is selected based on the steady polar of the airfoil, as this data is available for all considered airfoil. After comparison to the OSU references it is suggested that the angle at which the normal and lift coefficient start to differ significantly, is a suitable condition for changing the definitions in the model. This method for determining the angle is very rough and a more universal approach could be an area of future research.

The introduction of this angle means that the definition of the frequency term of the model is altered as the angle of attack changes. The resulting equations are shown in Equation 5.12. The angle α_s, used as a condition for changing the frequency coefficient, is referred to as the shedding angle from this point onward. For angles below this shedding angle, the original frequency definition as provided by Adema is used. For the NACA 4415 airfoil, this angle is set to be 25 degrees as will be discussed later in this section.

$$cf_{20} = \begin{cases} 10(k_s sin(\alpha))^2 \left(1 + 3\Delta C_{l,2}^2\right)\left(1 + 280^2\tau^2\left[\frac{d\alpha}{dt}\right]^2\right) & \text{if } \alpha < \alpha_s \\ 10k_s^2 \left(1 + 3\Delta C_{l,2}^2\right)\left(1 + 280^2\tau^2\left[\frac{d\alpha}{dt}\right]^2\right) + \frac{0.125}{sin^2(\alpha)} & \text{if } \alpha \geq \alpha_s \end{cases} \tag{5.12}$$

Implementing this new frequency term already improves the performance of the adapated dynamic stall model in the comparison to the reference data. This can be clearly seen in Figure 5.6.

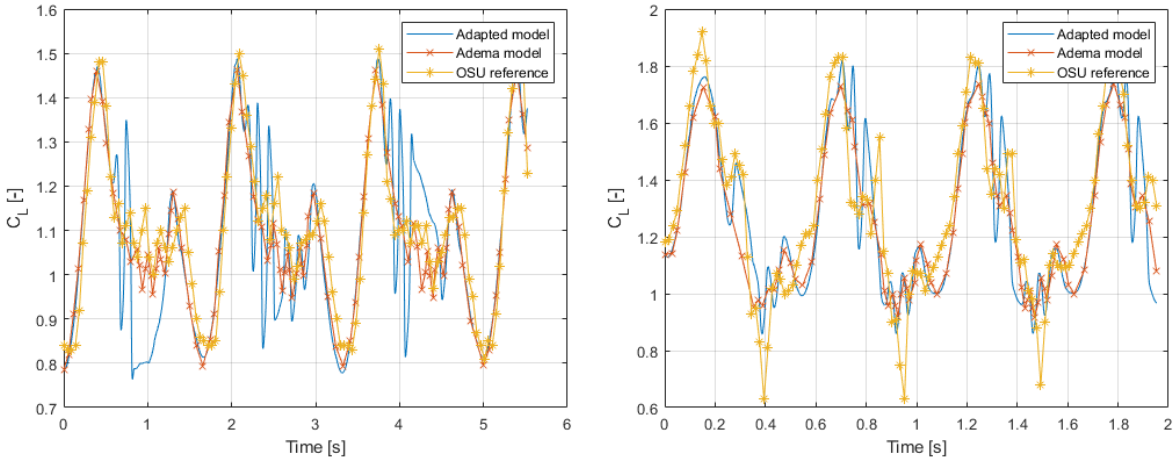

(a) Effect of new frequency, k = 0.0228 with a mean α of 14^o and a variation of 10.5^o

(b) Effect of new frequency, k = 0.0711 with a mean α of 18.4^o and a variation of 10.7^o

Figure 5.6: Effect of new frequency term

However, there is still some undesirable behaviour that can be observed in the results shown in Figure 5.6. For example, at the end of the upstroke the magnitude of the oscillations already become very large. These oscillations continue into the downstroke and take a long time to be damped out. To account for this the damping term also is adapted.

Several adaptations were attempted for improving the behaviour of this model at lower angles of attack. After these iterations the adaptations shown in Equation 5.13 showed promising results that will be presented in this section. On the downstroke a second critical angle is introduced for which the van der Pol damping is replaced with a constant damping, similarly to the IAG model. This angle, $\alpha_{s,2}$ is the angle at which the drag starts to increase significantly and the lift starts to become non-linear. This angle is referred to in Bangga et al. [2020] as the critical angle and generally relates to the onset of stall. For the NACA 4415 this angle was set to be 10 degrees.

The damping on the upstroke is also adapted to be almost identical to the original Adema formulation below the shedding angle. This was required in order to reduce the large oscillations that would occur at relatively low angles of attack. It should be noted that the absolute value of $\Delta C_{L,pot}$ is taken. This is the only adaptation present for these lower angles. The goal of this change is to also allow periodic responses for negative angles of attack.

$$cf_{21} = \begin{cases} 60\tau k_s \left(-0.01(|\Delta C_{l,pot}| + 0.25)^2 + 2\Delta C_{l,2}^2\right) & \text{if } \frac{d\alpha}{dt} > 0 \;\&\; \alpha > \alpha_s \\ 60\tau k_s \left(-0.01(|\Delta C_{l,pot}| - 0.5) + 2\Delta C_{l,2}^2\right) & \text{if } \frac{d\alpha}{dt} > 0 \;\&\; \alpha < \alpha_s \\ 60\tau k_s \left(-0.01(|\Delta C_{l,pot}| + 0.25)^2 + 14\Delta C_{l,2}^2\right) & \text{if } \frac{d\alpha}{dt} \leq 0 \;\&\; \alpha > \alpha_{s,2} \\ 0.2k_s & \text{if } \frac{d\alpha}{dt} \leq 0 \;\&\; \alpha < \alpha_{s,2} \end{cases} \tag{5.13}$$

The described changes allow the model to be more similar to the Adema model at lower angles of attack. This model has been shown to accurately model the dynamic stalling behaviour of airfoils, Adema et al. [2020]. However, at larger angles of attack it uses the

model that was developed in the previous chapter to more accurately predict the shedding frequency of the airfoil. In Figure 5.7 the results on a moving airfoil are compared for this new model as well as the original Adema model.

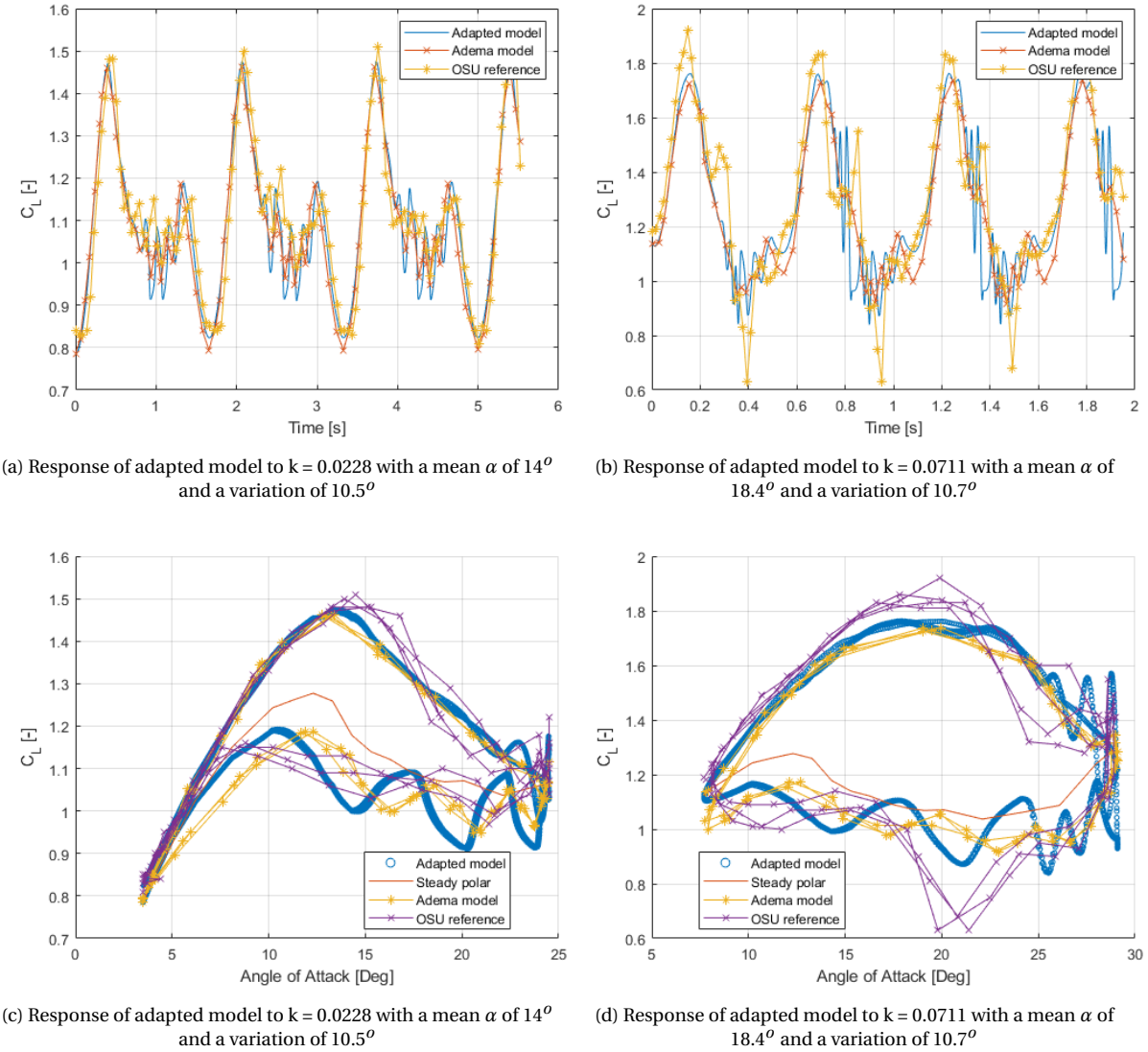

(a) Response of adapted model to k = 0.0228 with a mean α of 14^o and a variation of 10.5^o

(b) Response of adapted model to k = 0.0711 with a mean α of 18.4^o and a variation of 10.7^o

(c) Response of adapted model to k = 0.0228 with a mean α of 14^o and a variation of 10.5^o

(d) Response of adapted model to k = 0.0711 with a mean α of 18.4^o and a variation of 10.7^o

Figure 5.7: Adapted model response to OSU reference conditions

As has been discussed in this section, two new parameters are introduced that depend on the steady airfoil polar. In Figure 5.8 the two angles are indicated for the NACA 4415 airfoil that was used in the time responses shown in this section. The first angle, α_s is the angle at which the model switches to the vortex shedding version, which was created in the previous section. This angle is located at the angle, where the normal and tangential force start to deviate significantly from each other. The second angle, $\alpha_{s,2}$, is similar to the critical angle defined in Bangga et al. [2020]. This angle is found by considering the angle at which the drag starts increasing more rapidly and the linear section of the lift curve comes to an end. For now the same angle is used for the positive and negative side of the polar. For the critical angle this appears to be reasonable. The shedding behaviour might might depend on the direction as was observed in the experimental results. However, for the current ap-

plication, this choice seems to be acceptable based on the airfoil polar. The resulting angles for this airfoil were found to be 25 and 10 degrees for α_s and $\alpha_{s,2}$ respectively.

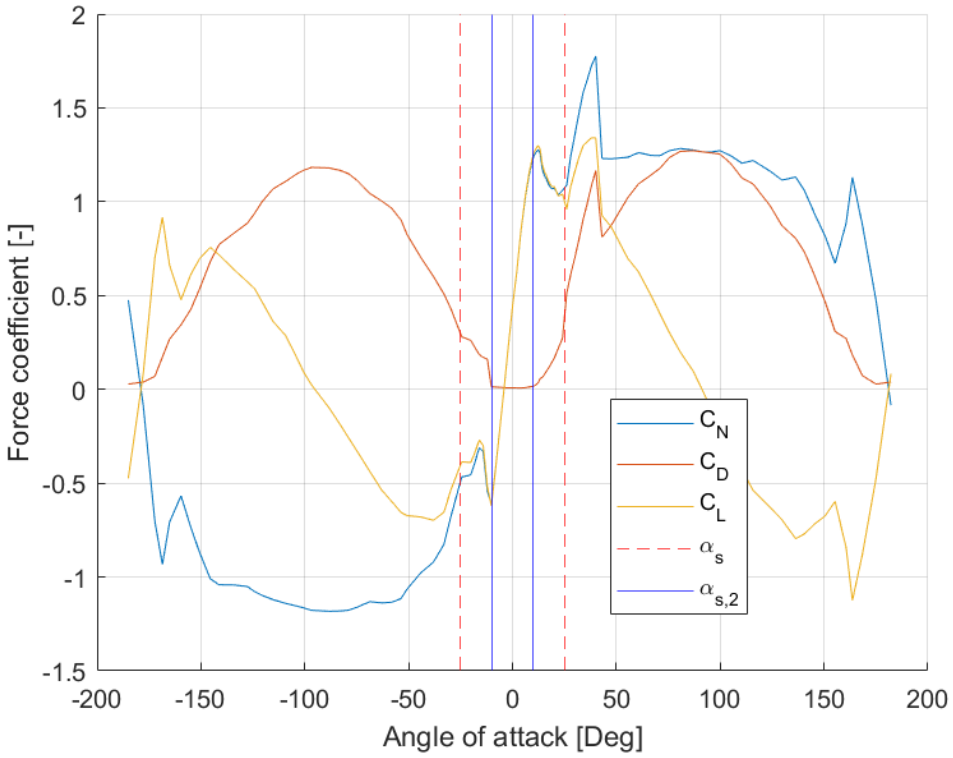

Figure 5.8: Determination of critical and shedding angle for the NACA 4415 airfoil

5.3 Performance adapted model

So far an adapted dynamic stall model has been proposed in this chapter. The changes this model made to the Adema model were supported by a number of visual comparisons to experimental results. In this section a quantitative assessment of the performance of the adapted model will be performed. This assessment will consist of an L_2 norm analysis of several results. These will include both vortex shedding predictions as well as applications to pitching airfoils. For clarity, the definition of the L_2 norm as an error measurement is shown in Equation 5.14.

Firstly, the predicted vortex shedding frequencies are considered. This is done by comparing to the three available experiments that were shown previously to the proposed dynamic stall model. Since only the vortex shedding behaviour is examined here, only deep stall conditions should be considered for these experiments. For example, the analysis of the DNW experiment will only contain measurements related to angles larger than 30 degrees. This angle was found to be the angle at which vortex shedding would occur.

The second part of the analysis contains pitching airfoil cases at more moderate angles of attack of below 30 degrees. This is done through comparing the results to experimental references from OSU database. The combination of both these performance reviews, should allow for a complete assessment of the proposed dynamic stall model.

$$L_2 = \sqrt{\frac{1}{N}\sum_{i}^{N}\left(x_{i,experiment} - x_{i,simulation}\right)^2} \tag{5.14}$$

The first considered parameter is the predicted shedding frequency for the deep stall conditions of each airfoil. The errors for each of the angles which are included were combined using Equation 5.14. This resulted in the errors shown in Table 5.1. From these results, it is clear that the errors prediction of the vortex shedding frequency is greatly improved. This is in line with the changes observed in the previous sections.

It should be noted that the two adapted models are included in this table. The first is the model purely based on the frequency predictions which was presented in section 5.1. The second is the blended model that was presented in section 5.2. These models are expected to be identical for these cases as the shedding angle, α_s, is close to 25 degrees for the considered airfoils. Therefore, the model presented in the previous chapter and the one which includes the blending produce the same results in terms of shedding frequency.

Table 5.1: Comparison of L_2 errors for the considered models in terms of predicting the shedding frequency

Models	TU Delft experiment	DNW experiment	NACA 4412 experiment
Snel	0.1626	0.2044	0.1778
Adema	0.1036	0.1604	0.0783
Frequency based	0.0184	0.0307	0.0277
Blended	0.0184	0.0307	0.0277

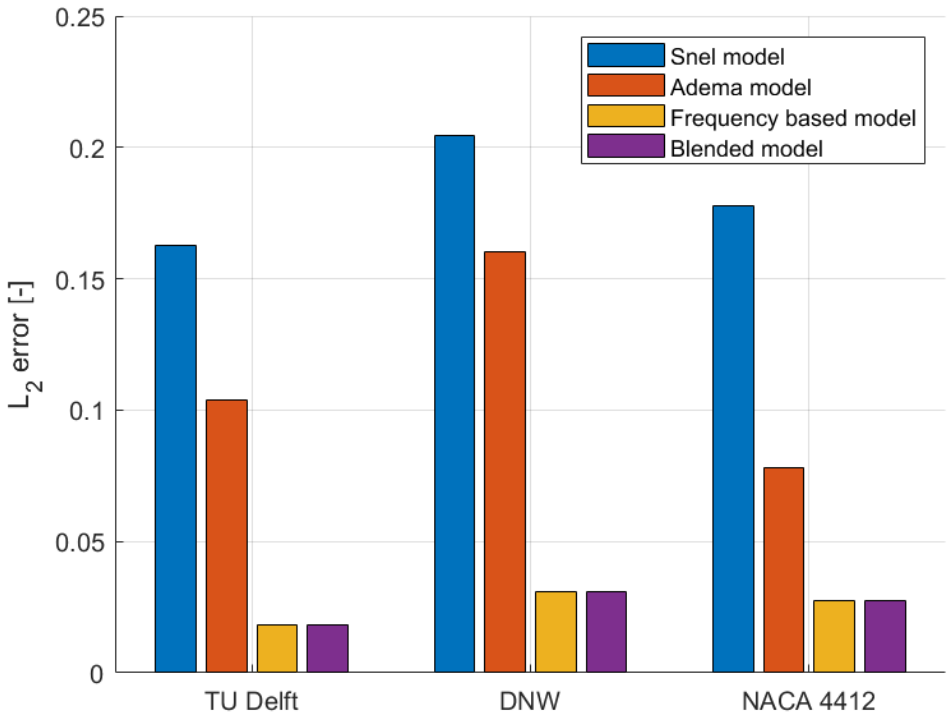

Figure 5.9: Error comparison of different model in terms of shedding frequencies

Next, the comparison of the error on a pitching airfoil for several models is considered. As a reference, both the original Snel and Adema models are considered. The IAG model was not used as the model results were not exactly replicated during the verification, appendix B. Once again, the two adapted models presented in this chapter are considered in this analysis initially. It should be noted that the errors that are presented here are based on the same OSU references that were used in the verification of both the Snel and Adema model on a NACA 4415 airfoil (appendix B). The relevant cases and errors are shown in Table 5.2.

Table 5.2: Comparison of L_2 errors for the considered models applied to a moving NACA 4415 airfoil

Model	k = 0.0228, $\bar{\alpha} = 14^o, \Delta\alpha = 10.5^o$	k = 0.0711, $\bar{\alpha} = 18.4,^o, \Delta\alpha = 10.7^o$
Snel	0.1134	0.177
Adema	0.0639	0.1305
Frequency based	0.0954	0.1573
Blended	0.0652	0.1594

Based on these results, it was also found that when the frequency based model was applied to the moving airfoil cases, the error increased. Therefore, the need for the blending introduced in the previous section is also supported by the errors that the different models produce.

It should be noted that this did not eliminate the increased error in both cases shown here. However, as shown previously in this section, this blending does remove a lot of the oscillatory behaviour from these cases. Therefore, a visual comparison of the results should also be considered in addition to the error.

Based on these observations, it is suggested that a comparison of the frequency spectra could be a good addition to the error analysis of such models. However, for this research, the L_2 error as well as a visual comparison were deemed sufficient.

Thirdly, the blended model produces worse results when compared to the Adema model for the pitching airfoil cases. However, only two cases are considered here. To investigate if this result also extends to other airfoils and operating conditions more data from the OSU database will be used. For this purpose all the reference cases that were used to calibrate the Adema model can be considered, Adema et al. [2020].

These cases consider two airfoils and a variety of movements for both airfoils. The airfoils are a NACA 4415 airfoil and a S809 airfoil. These airfoils have a 15% and 21% thickness to chord ratio respectively. The NACA 4415 airfoil is more strongly cambered, with a 4% maximum camber, while the S809 airfoil only has a maximum camber of 1%. Therefore, the use of both of these airfoils provides information on two different geometries. The used operating conditions are shown in Table 5.3. These resulted in the comparisons shown in Figure 5.10 and Figure 5.11.

Table 5.3: Operating conditions used for all references in OSU database

S809	Case number	1	2	3	4	5	6	7	8	9
	Mean [Deg]	8	8	8	14	14	14	20	20	20
	Variation [Deg]	10	10	10	10	10	10	10	10	10
	k [-]	0.02	0.04	0.064	0.02	0.042	0.062	0.021	0.04	0.062
NACA 4415	Case number	11	12	13	14	15	16	17	18	19
	Mean [Deg]	8	8	8	14	14	14	20	20	20
	Variation [Deg]	10	10	10	10	10	10	10	10	10
	k [-]	0.02	0.04	0.064	0.02	0.042	0.062	0.021	0.04	0.062

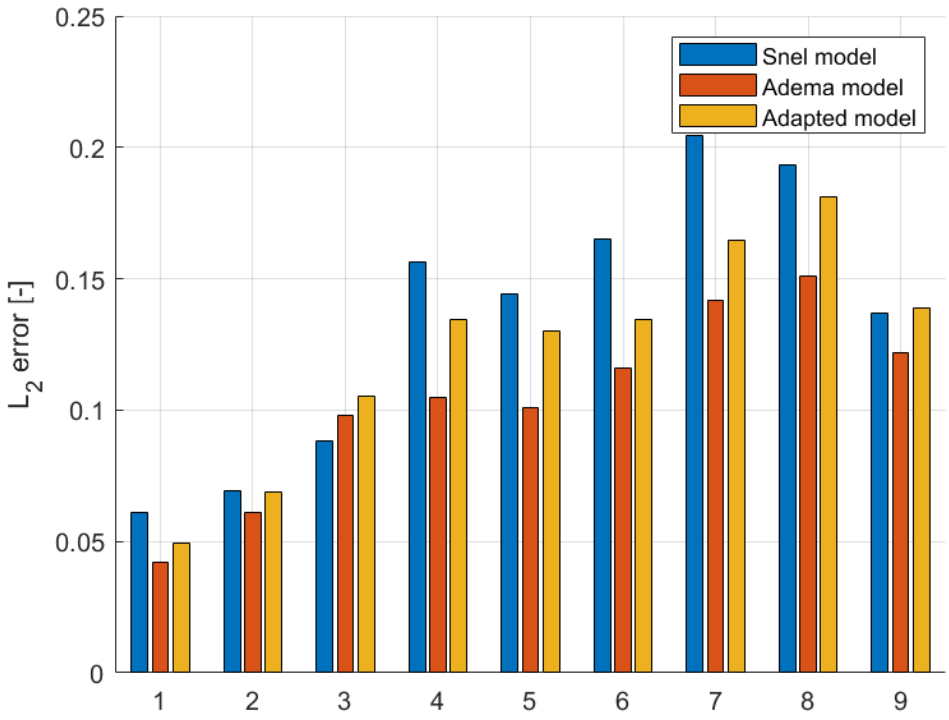

Figure 5.10: Error comparison of different model for a moving S809 airfoil

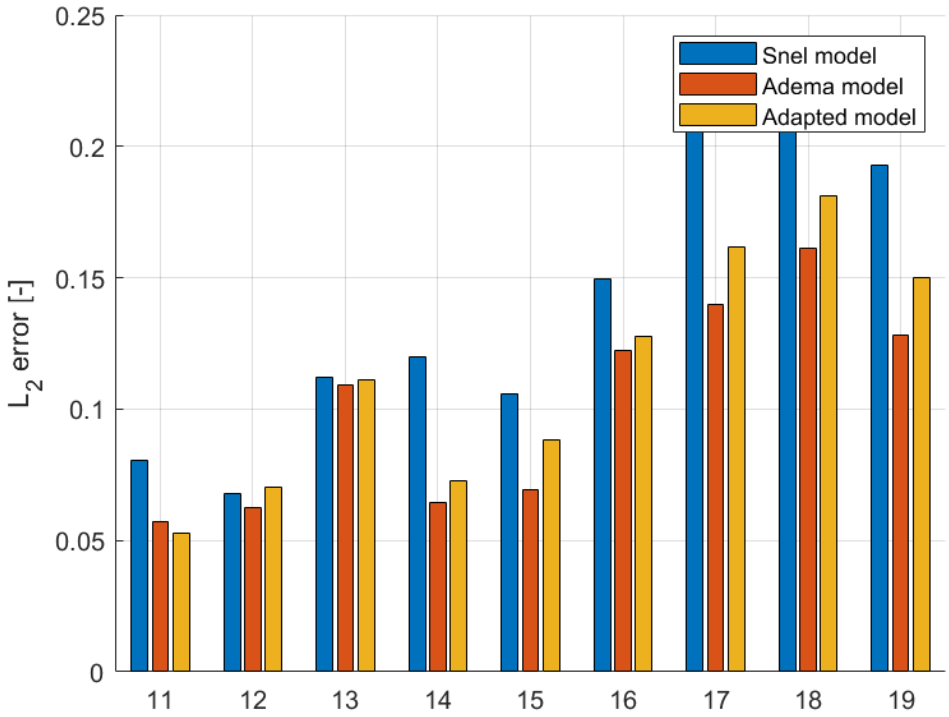

Figure 5.11: Error comparison of different model for a moving NACA 4415 airfoil

From these comparisons it can be concluded that the blended model that has been created performs worse compared to the Adema model for almost all cases. However, this is to be expected to an extend as the Adema model was calibrated specifically for these cases.

Interestingly, the blended model does still perform better than the Snel model for almost all cases. This shows that the introduction of the two critical angles has allowed to the model to maintain a portion of the accuracy of the Adema model. Despite this, there is still possibilities for further improving the adapted model as is discussed in this section.

It should be noted that the blending approach used in this section is a very rudimentary approach. A more sophisticated method could produce better results and allow for a more general application. For example the discontinuity introduced in the definitions of the coefficients could be removed. This could be achieved by using a region of angles of attack over which a combination of each definition is used. The goal of this would be to remove the very sudden onset of oscillations at the larger angles in the OSU cases, which is observed in many of these results, for example in Figure 5.7.

In addition to removing the discontinuity, a more exact definition of the critical angles could improve the results. It has been observed that the shedding behaviour can become dominant at relatively high angles of attack, Fallahpour et al. [2022]. Therefore, the current selection criterion might result in a premature introduction of the adapted model. This once again could reduce the sudden oscillations observed in the results at larger angles.

Therefore, a more detailed approach might be beneficial for determining which definition of the model coefficients to use. Such a methods could for example try to include the an estimate of the base pressure coefficient based on a simple solution method. This ap-

proach could use the observation that at angles far beyond stall the pressure coefficient on the suction side is relatively constant. Additionally, the pressure side does not experience separation and therefore could perhaps be modelled using simple methods. Combining an estimate of the pressure on the pressure side with the steady lift coefficient could potentially give an approximate value of the base pressure coefficient.

An implementation of this approach using a potential method for a flat plate as the model for the pressure side was implemented. However, this method was found to deviate too significantly from the observed pressure distribution on the pressure side. Therefore, including the shape of the airfoil in this method might be able to provide a sufficiently accurate representation.

In conclusion, the presented model was found to greatly improve the prediction the shedding frequency for all three experiments. When traditional pitching airfoil cases were considered, the model did lose some accuracy compared to the Adema model. It is expected this could be corrected by an improved blending approach. However, the current work will focus on further improving the predictions of the shedding frequencies presented here.

Chapter 6

Model calibration using uncertainty quantification tool

In the previous chapter an adapted dynamic stall model was proposed. This model was obtained based on several adaptation that were made by hand to match the results of the dynamic stall model to experimental results. In this section the parameters used in this dynamic stall model are examined more closely. This is done by first performing a sensitivity analysis on the parameters to determine which are influential in predicting the vortex shedding frequencies. Next, a calibration is performed using a Bayesian inversion approach. Finally, several calibrations are presented based on the previously presented experiments.

6.1 Sensitivity analysis

TO better understand the created model, a sensitivity analysis cam be performed. The goal of this analysis is to identify which parameters are most influential on the predicted values of the shedding frequencies. This information can be used to more effectively calibrate the model and potentially eliminate some parameters from the calibration. Additionally it can provide insight into the relative influence of the model parameters, which is useful information for future adaptations of the model.

The sensitivity analysis is performed using the uncertainty quantification tool UQLAB, Marelli and Sudret [2014]. Generally, to perform the analysis a probability distribution is defined for each model parameter that are used as input. Next, each of the distributions is sampled in order to obtain a large number of combinations. For each sample the output is computed by evaluating the model, in this case the dynamic stall model presented in the previous chapter. Finally, the individual effects of the parameters can be extracted by correlating the changes in the output of the model to the changes in the input. The method for defining the correlation parameter is shown by Equation 6.1. This equation is applied to each input parameter contained in X and output Y to obtain the correlations shown later in this section. When this process is completed, the relative influence of each input on each output is known.

$$\rho_i = \frac{\mathbb{E}\left[(X_i - \mu_i)(Y - \mu_Y)\right]}{\sigma_i \sigma_y} \tag{6.1}$$

To determine the coefficients considered for the calibration, the model definition shown in Equation 6.2 and Equation 6.3. Firstly, some coefficients can be excluded from the sensitivity analysis from the start. The forcing term does not have an effect on the predicted shedding frequency and therefore none of these parameters are included in the sensitivity study. Secondly, since this calibration is aimed at the prediction of the shedding frequency, the definitions used below α_s are also not considered. Additionally, any term applied to a time derivative is irrelevant for this analysis as a stationary airfoil is considered. Therefore, only one of the damping definition will be used in the sensitivity study and calibration.

Considering the exclusion of the discussed parameters, only six parameters remain to be analysed in terms of their sensitivity. These parameters are labelled P_1 to P_6 in Equation 6.2 and Equation 6.3. The value of 60 in the damping equation is not chosen as a calibration parameter as any change in this term can be obtained by changes in the other parameters in this equation.

$$cf_{20} = \begin{cases} 10(k_s sin(\alpha))^2 \left(1 + 3\Delta C_{l,2}^2\right)\left(1 + 280^2\tau^2\left[\frac{d\alpha}{dt}\right]^2\right) & \text{if } \alpha < \alpha_s \\ P_1 \cdot 10k_s^2 \left(1 + P_2\Delta C_{l,2}^2\right)\left(1 + 280^2\tau^2\left[\frac{d\alpha}{dt}\right]^2\right) + \frac{P_6}{sin^2(\alpha)} & \text{if } \alpha \geq \alpha_s \end{cases} \tag{6.2}$$

$$cf_{21} = \begin{cases} 60\tau k_s \left(-0.01(|\Delta C_{l,pot}| + 0.25)^2 + 2\Delta C_{l,2}^2\right) & \text{if } \frac{d\alpha}{dt} > 0 \;\&\; \alpha > \alpha_s \\ 60\tau k_s \left(-0.01(|\Delta C_{l,pot}| - 0.5) + 2\Delta C_{l,2}^2\right) & \text{if } \frac{d\alpha}{dt} > 0 \;\&\; \alpha < \alpha_s \\ 60\tau k_s \left(P_3(|\Delta C_{l,pot}| + P_4)^2 + P_5\Delta C_{l,2}^2\right) & \text{if } \frac{d\alpha}{dt} \leq 0 \;\&\; \alpha > \alpha_{s,2} \\ 0.2k_s & \text{if } \frac{d\alpha}{dt} \leq 0 \;\&\; \alpha < \alpha_{s,2} \end{cases} \tag{6.3}$$

Having which parameters should be considered in this analysis, the next step is to define the variations of each parameter. This is required in order to determine the space which will be sampled. In Table 6.1 the definitions of each model parameter distribution is shown. Since all model parameters do not have an physical interpretation, the variation of these parameters is difficult to determine. The presented distributions were selected based on the observed effects of each parameter in the shedding frequency response. The variations were selected such that the vortex shedding frequencies for each experiment would remain bound to reasonable values, producing projected Strouhal number between 0.1 and 0.2 approximately. However, the variation within these bounds was maximised in order to ensure a sufficiently large variation in the output. Several iterations of these probability distributions were used in this process before the shown distributions were selected.

Table 6.1: Description of parameters for sensitivity analysis

Parameter	P1	P2	P3	P4	P5	P6
Distribution	Gaussian	Gaussian	Gaussian	Uniform	Gaussian	Gaussian
Description	μ = 1 σ = 0.15	μ = 3 σ = 0.3	μ = -0.01 σ = 0.0025	Lower = -0.7 Upper = 0.7	μ = 14 σ = 4	μ = 0.125 σ = 0.05

The final consideration for the sensitivity analysis is the definition of the output. Two options were considered for this purpose. Both methods use the projected Strouhal number produced by the dynamic stall model. Since each experiment has a different number

of data points, the first option aimed to reduce the number of outputs to the same number for each experiments. Therefore, the output was chosen to be the averages of the projected Strouhal number for several ranges of angles of attack. The purpose of these ranges is to identify the effect of each parameter on the predicted frequencies at low, middle and high angles of attack.

Unfortunately, this first approach caused some issues. The introduction of an additional operation after the simulation of the dynamic stall model was found to have a negative effect on the convergence of the surrogate models. These models will be discussed in more detail in the next section. Additionally, the operation of averaging might remove some effects that are present. For example an increase in slope on a section could result in the same average and therefore not seem relevant at all. Therefore, this option for the output was discarded.

The second option for the output was thus selected. In this case, no additional operations are applied to the output of the dynamic stall model. Instead, to reduce the number of data points, the output is sampled based on the angle of attack. After some trial and error an interval of 15 degrees was selected for the DNW and TU Delft experiment. Since the NACA 4412 experiment has fewer data points a finer sampling approach of 5 degrees was selected for that experiment. These values were deemed to produce a sufficiently fine sampling to accurately assess the performance of the calibration without increasing the computational cost too much. In future calibrations it might be beneficial to consider a finer sampling of the output.

Having defined both the input and output parameters, the sensitivity analysis can be performed. This was done with the correlation approach implemented in UQLAB, Marelli et al. [2022a]. This approach allows for a determination of which parameter is more sensitive. Additionally, the direction in which the parameter influences each output signal can also be obtained from this method.

The results of the correlation parameter, ρ, are shown in Figure 6.1a to Figure 6.1f for several amounts of samples. The magnitude of the correlation parameter determines how significant the correlation is and the sign indicates the direction. Both of these results can be useful for future adaptations of the model.

To ensure the obtained correlation parameters are representative for the actual model results, the number of samples taken to perform the analysis was varied. From these images it is clear that the main correlations are not changing significantly with the number of samples after 500 samples. Therefore, 600 samples were considered in the sensitivity analysis to ensure an accurate representation of the influence of each parameter.

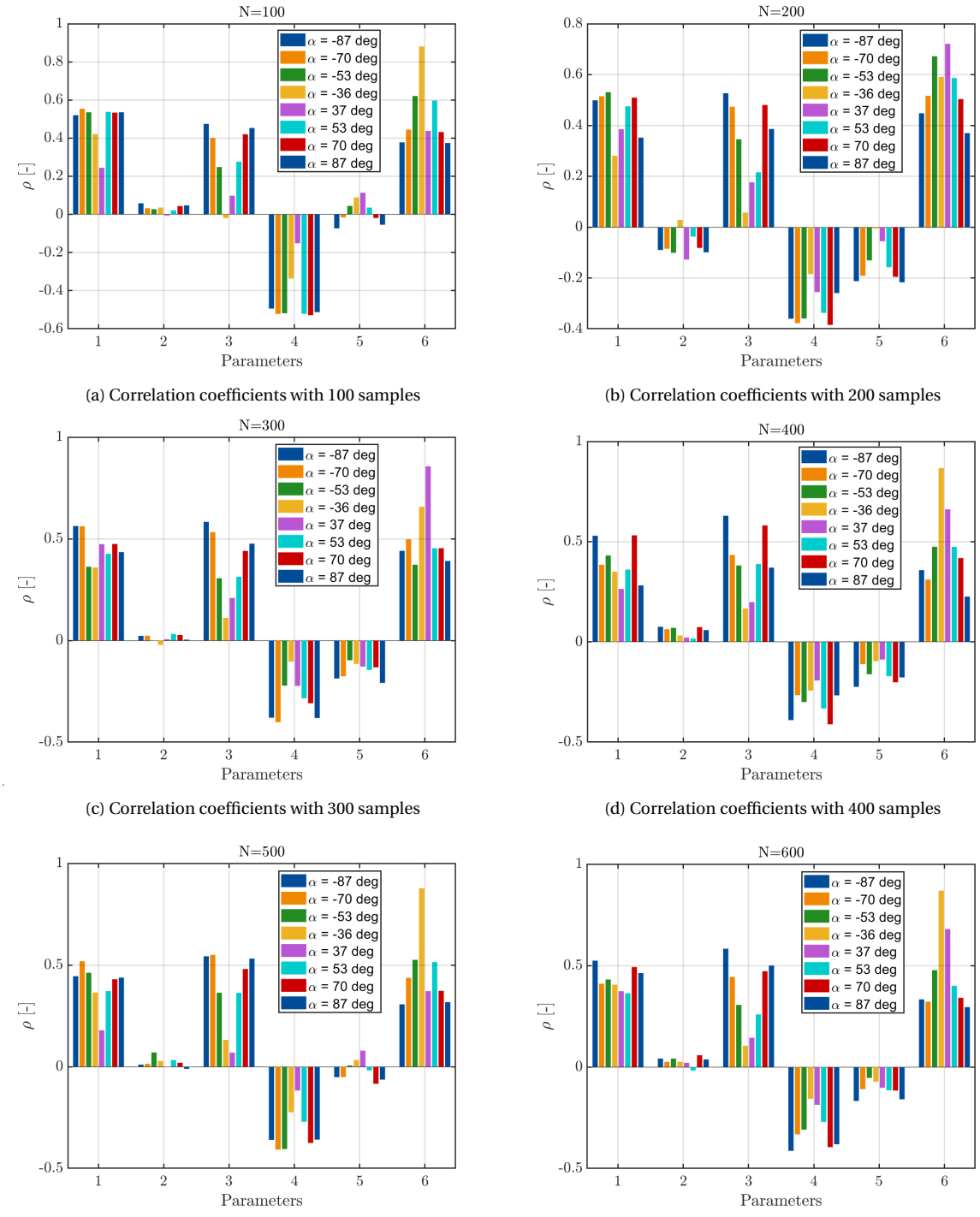

(a) Correlation coefficients with 100 samples

(b) Correlation coefficients with 200 samples

(c) Correlation coefficients with 300 samples

(d) Correlation coefficients with 400 samples

(e) Correlation coefficients with 500 samples

(f) Correlation coefficients with 600 samples

Figure 6.1: Correlation coefficients for the DNW experiment using varying amounts of samples

In Figure 6.1 the correlation between each of the parameters and outputs is shown. Based on this it can be determined that some parameters are more critical than other. Firstly, most of the selected parameters show a noticeable correlation at the considered angles. Especially parameters 1, 3, 4, and 6 can be identified as the most influential. It can also be shown that the influence of each of these parameters varies with angles of attack. For example, the third parameter clearly has a more significant influence at larger angles

of attack. However, the sixth parameter has a larger impact on the shedding frequency at lower angles of attack. These conclusions can be useful for any further adaptation of such a model.

Additionally, it can be observed that some parameters are not as important for the predicting of the shedding frequency. For example, the second parameter has a very limited influence on the predicted frequency. The fifth parameter also has generally lower correlation coefficients compared to the other parameters. Based on this, these parameters could be excluded from the calibration to reduce the computational effort. However, it was deemed that the small increase in freedom in adapting the model was worth the computational expense. As such, these parameters were still included in the calibration in the coming sections.

As has been outlined earlier in this report, several experiments are considered. Therefore, the sensitivity of these other experiments should also be investigated. The purpose of this is to determine if the different airfoils produce different correlations for the same input. In Figure 6.2 the correlation parameters of each of the experiments is shown. In the TU Delft experiment the same sampling approach was considered as for the previously presented DNW case. However, since the NACA 4412 experiment only considers a single sided spectrum, the distance between samples was decreased to 5 degrees.

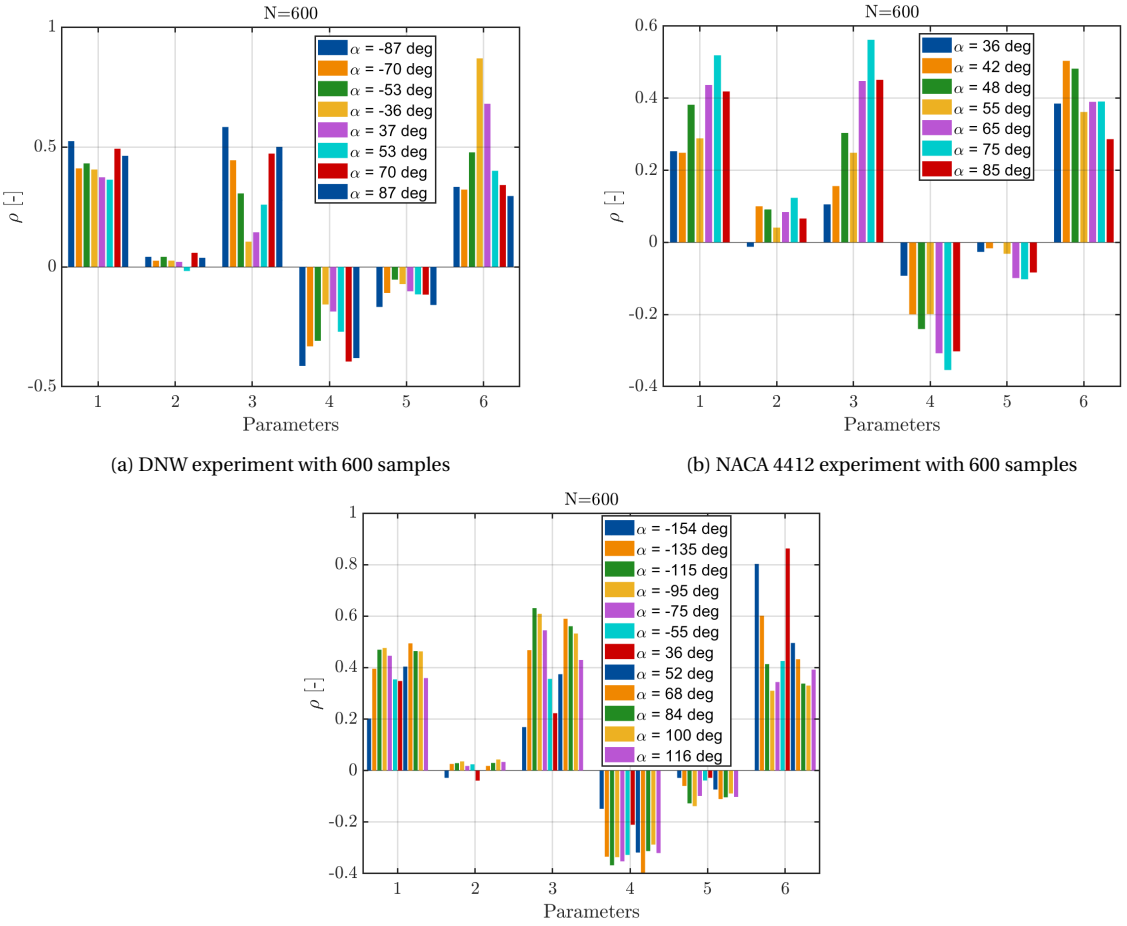

(a) DNW experiment with 600 samples

(b) NACA 4412 experiment with 600 samples

(c) TU Delft experiment with 600 samples

Figure 6.2: Sensitivity analysis comparison between experiments

Based in the comparison of the correlation coefficients shown in Figure 6.2, several conclusions can be drawn. Firstly, one should consider that due to the chosen output, the number of outputs for each experiment varies. However, the effect of each parameter for different angles of attack can still be considered. In this discussion, low angles are considered to be angles close to the onset of shedding. High angles on the other hand are described as angles which place the airfoil perpendicular to the flow. Therefore, the angles far beyond 90 degrees should be considered as low angles once again as for the purpose of shedding these angles behave similarly to low angles of attack.

Using this approach the effects of some of the parameters are examined. Firstly, as was already discussed the second and fifth parameter are not as relevant for determining the shedding frequency obtained by the dynamic stall model. The correlation parameter for both parameters is relatively small over the entire range of angles of attack compared to the other parameters. It should be noted that the fifth parameter is slightly more influential than the second, however still significantly less compared to the other parameters.

The second parameter that is considered is P_1. This parameter has quite a strong correlation with the shedding frequency for all angles of attack. This is to be expected as it directly influences the frequency coefficient in the dynamic stall model. Additionally, it can be observed that this parameter has little variation in the correlation parameter with angle of attack. There is a slight increase in influence at larger angles of attack, especially for the TU Delft experiment. However, one can clearly observe that this variation lesser compared to some of the other parameters. Therefore, this parameter would be most suited for adapting the predicted shedding frequency for all angles in the same direction.

Thirdly, two parameters that mainly influence the predictions at large angles of attack are selected. These are P_3 and P_4. Both parameters show much stronger correlation at larger angles of attack compared to smaller angles. The reason for this correlation can immediately be explained in the case of P_3, as this parameter is used in a multiplication with $\Delta C_{l,pot}$. The potential difference is significantly larger at high angles of attack. Therefore this parameter is expected to be most influential there. The strong correlation of P_4 is not as directly explained. However, since it is included in the same term as the potential difference as well, a similar reason for the correlation is expected. Hence, these two parameters can be used to influence the shedding frequency specifically at higher angles of attack.

Finally, the sixth parameter is examined. This parameter was observed to have an opposite effect compared to the previously discussed pair. This parameter appears to be especially influential for the shedding frequency at lower angles. The final parameter was newly introduced in this model and is scaled by dividing by $sin(\alpha)$. Therefore, it is to be expected that this parameter is specifically influential at the lower angles of attack.

6.2 Calibration procedure

In the previous section, the relative influence of each model parameter was determined. The next step is to calibrate them based on the experimental results. Several steps have to be taken in the selected calibration process. To perform the calibration procedure using a Bayesian inversion, a Markov-chain is constructed. This approach can require a large amount of model evaluations. Therefore, a surrogate model is used to reduce the computational effect. In this section the construction of this surrogate model is described. Additionally, the other steps required to perform the calibration are outlined.

6.2.1 Surrogate modelling

The calibration considers the predicted frequencies at the same selection of inflow angles that were used in the sensitivity analysis. To obtain these directly from the dynamic stall model is quite time consuming. Therefore, a surrogate model is constructed. This surrogate model must be a sufficiently accurate representation of the response of the actual model in order for the calibration to be valid.

Several steps are taken in the contraction of such a surrogate model. Firstly, the selected input parameters, shown in the sensitivity study, are varied based on their probability distribution. After selecting a number of samples from each of the model coefficients, the dynamic stall model is evaluated for each condition. Finally, the output of each of these evaluations is used to create a surrogate model using polynomial chaos expansion, Marelli et al. [2022b]. This step creates an approximation of the response through a combination of a large number of polynomials. As a result, the surrogate model is able to return an estimate of the output of the dynamic stall model very quickly. Therefore, the surrogate can be effectively used in the calibration.

Some limitations were imposed in the selection of the samples used in the surrogate model. Samples which produced projected Strouhal numbers above 0.21 or below 0.05 at any of the sampled locations were excluded. These values were considered to be outliers and would greatly affect the accuracy of the surrogate model in other locations. This is due to the global nature of the chaos expansion. Since the experimental values that are used for the calibration are also located very far from these bounds, the exclusion of these samples is not expected to negatively impact the calibration itself.

As discussed previously, the surrogate model must be sufficiently accurate for the calibration to work. To investigate the accuracy of the surrogate model, the Leave-One-Out (LOO) error is considered. This error is defined as is shown in Equation 6.4 and uses cross-validation to prevent over-fitting, Marelli et al. [2022b]. As the number of samples that is used to construct the model increases, the accuracy is also expected to increase. After some investigation an LOO-error in the range of 10^{-3} was deemed acceptable for this application. This was done by considering the average error in the projected Strouhal number for a number of cases. For this error, the average error would be in the order of 0.001, which was deemed to be sufficient.

In Figure 6.3 the convergence of the LOO-error is shown for the outputs related to the DNW experiment. This image shows the expected convergence for all angles that are considered. Since none of the outputs can be inaccurately modelled, which line corresponds to which output is not relevant for the current calibration.

$$\epsilon_{LOO} = \frac{\sum_i^N \left(\frac{\mathcal{M}(x^i) - \mathcal{M}^{PC}(x^i)}{1-h_i} \right)^2}{\sum_i^N \left(\mathcal{M}(x^i) - \hat{\mu}_Y \right)^2} \tag{6.4}$$

In Figure 6.3 it can be observed that the LOO-error decreases consistently with the number of samples. Therefore, selecting a larger number of samples increases the accuracy as would be expected. Finally, a surrogate model using 1000 samples was used for the DNW experiment. A larger number of samples could also be used. However, this would greatly increase the computational cost for a limited gain in terms of accuracy.

In addition to the number of samples, the selection of the input variables is also an important component of the surrogate model. The selection is done by creating proba-

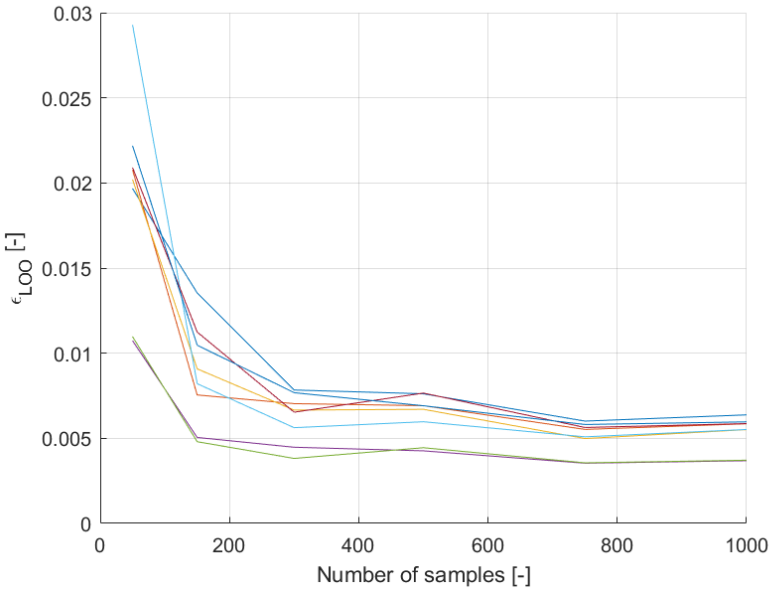

Figure 6.3: Convergence of the surrogate models for the DNW experiment

bility distributions for each parameter and sampling those. Therefore, these distributions should be reasonable compared to the original parameter. A large variation in the parameters also causes a large variation of the output, as such making it harder to construct a model. However, choosing an insufficiently large variation causes the range of the model to be too small. This would result in only very small changes to the parameters in the calibration. For this purpose the variations used in the sensitivity analysis, Table 6.1, were also used in the creation of the surrogate models.

Apart from the DNW experiment, the two other discussed experiments can also be considered in this calibration. For this purpose, surrogate models for these experiments were also constructed. The sampling of the output as well as the input parameters are identical to the previously described approaches for these experiments. In Figure 6.4 the convergence of the other surrogate models is shown. Based on these plots, the TU Delft and NACA 4412 experiment both use 1000 samples for their final surrogate models as well.

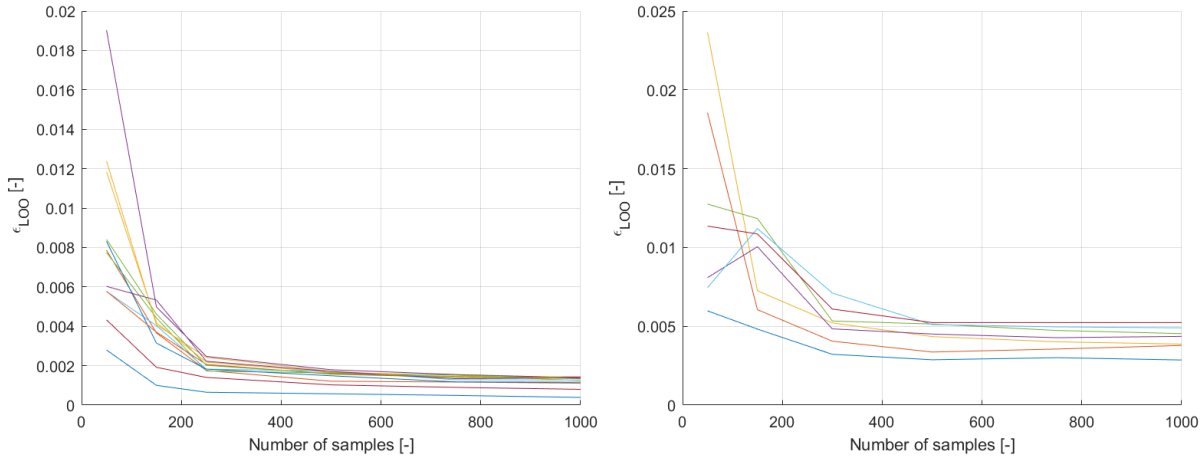

(a) TU Delft surrogate model convergence

(b) NACA 4412 experiment surrogate model convergence

Figure 6.4: Convergence of the surrogate models for the other experiments

6.2.2 Calibration settings

The calibration procedure is performed using UQLAB. Within this software there are several options available for the calibration such as the solver or the number of steps. Different settings were considered, until a configuration was found which provided good convergence for all different experiments. The final settings are shown in Table 6.2. The steps and number of chains represent the number of samples that are taken in the Markov chain in order to produce the sampling of the posterior. The uncertainty is the assumed variation of the data, as was shown in section 2.6. The solver represents the method used to perform the calibration, in this case Markov-chain Monte Carlo. Finally, the solver affects the method by which samples in the chain are accepted or rejected. As was discussed in section 2.6, this should not affect the solution only the convergence rate. The selected sampler is the Affine Invariant Ensamble Algorithm.

Table 6.2: Settings for calibration procedure UQLAB

Calibration setting	Solver	Sampler	Steps	Number of chains	Uncertainty
Value	MCMC	AIES	20000	20	$1 \cdot 10^{-7}$

Apart from the settings used in the calibration procedure, a prior distribution also has to be defined for all model parameters. This distribution is representative of an initial guess for the design space of the input parameters. Changing the prior allows the user to limit the domain in which the calibration takes place. Therefore, the prior must be used to constrain the solution to regions where the surrogate model is valid. The surrogate model is constructed based on previously described probability distributions. Hence, the prior distributions at least have to be contained within the distributions used to create the surrogate models. Additionally, the prior distributions might be used to limit the domain in which the model is calibrated further. This could be done to for example improve the convergence of the model, if the calibration entered regions for which the surrogate model was not as accurate.

The prior distribution that was used is shown in Table 6.3. The distributions used in this prior have lower variations compared to the ones used in the surrogate model and sensitivity analysis. This was done to promote solutions that remained within the applicable range of the surrogate models. The accuracy of the surrogate models was found to decrease further away from the prescribed mean values of the input parameters. In those cases, the correlation between the surrogate model result and the actual result of the dynamic stall model is not guaranteed. Therefore, a reduction in the variations of the prior was found to be required. The selected variations were based on a number of iterations in which the variations were slightly reduced and the results assessed. It is possible that the calibration is still moved towards to edges of the applicable range of these surrogate models. In this case more iterations with surrogate models centred at new values could be used to further improve the results.

Additionally, it should be noted that the values of the model coefficients were limited through more than the prior distribution. To ensure a good correlation between the surrogate and the actual model, the variations had to be limited to three times the standard deviation for most parameters. This was required as the normal distribution approaches zero but never actually takes that value. As a result, solutions could be accepted that were far from the applicable range of the surrogate models. The uniform parameter did not consider this limitation as this distribution is already limited at the upper and lower bound.

Table 6.3: Description of prior used for the Bayesian inversion

Parameter	P1	P2	P3	P4	P5	P6
Distribution	Gaussian	Gaussian	Gaussian	Uniform	Gaussian	Gaussian
Description	$\mu = 1$ $\sigma = 0.1$	$\mu = 3$ $\sigma = 0.3$	$\mu = -0.01$ $\sigma = 0.002$	Lower = -0.7 Upper = 0.7	$\mu = 14$ $\sigma = 2$	$\mu = 0.125$ $\sigma = 0.02$

6.3 Calibration results individual experiments

In this chapter all the steps required to perform a calibration have been presented. These are first applied to each of the available experiments individually. The goal of this is to investigate if the different data sets tend to produce similar values in terms of model parameters. In addition to that, the effectiveness of the calibration method can be examined this way.

For each of the experiments the calibration converged to a unique solution. The convergence was assessed using the multivariate potential scale reduction factor implemented in Wagner et al. [2022b]. This parameter approaches one for each of the shown calibrations, indicating that the calibration process has converged. The results of each of the calibrations are shown in the images below.

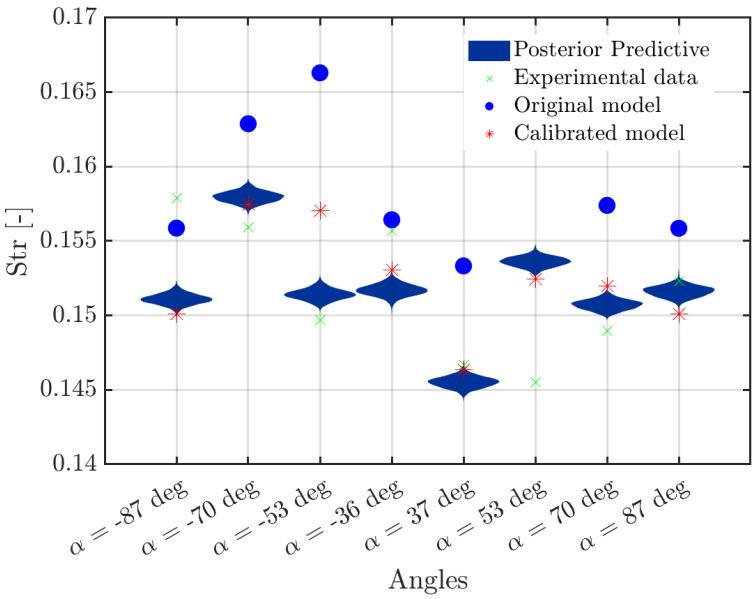

Figure 6.5: Calibration results for the DNW experiment

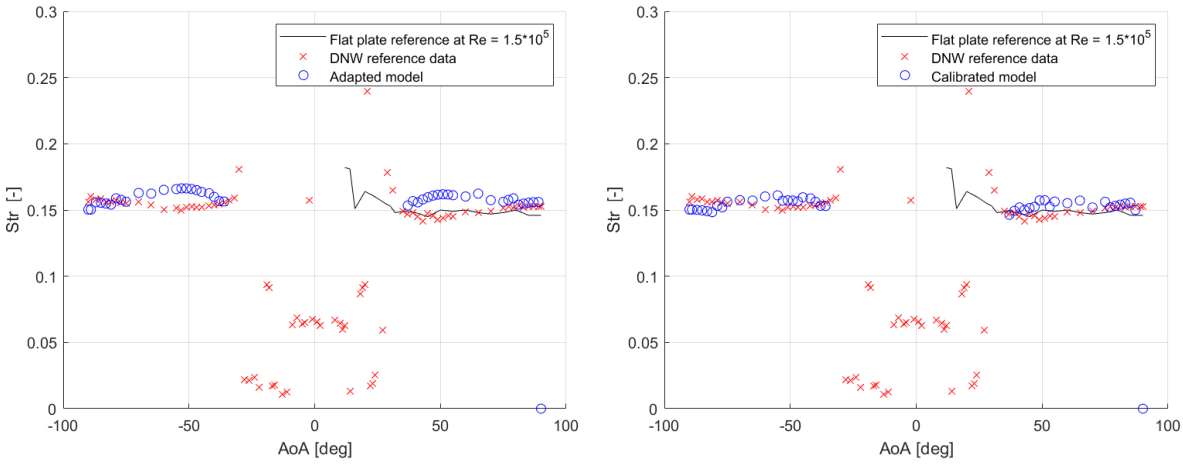

(a) DNW comparison before calibration

(b) DNW comparison after calibration

Figure 6.6: Effect of calibration on DNW experiment

In Figure 6.5, the results of the angles that are considered in the calibration are shown. These are the angles that were used to tune the model parameters. In this image, the probability distribution of the posterior is shown as well as the experimental results. Additionally, the predicted projected Strouhal number for both the original and calibrated model are shown. These values were obtained by evaluating the dynamic stall model for the corresponding model parameters.

From these results, it can be concluded that generally the calibration has improved the prediction of the shedding frequency. Only in 2 cases, -87 and -36 degrees, the prediction is worse. For all other angles the prediction is improved. This improvement is quite small as the original model already was located very close to the experimental values.

In addition to the angles considered in the calibration, the calibrated model can be ap-

plied to the entire range. This is done in Figure 6.6, where all angles in the calibration range (above 35 degrees) are compared to the experiment. This range was selected to exclude the strong variation that is still present around 30 degrees and only include the constant range of projected Strouhal numbers in the calibration. From these images it appears that the overall prediction of the projected Strouhal number is slightly improved by the calibration. The calibrated model also shows slightly less variation with angle of attack, which is desirable in this case.

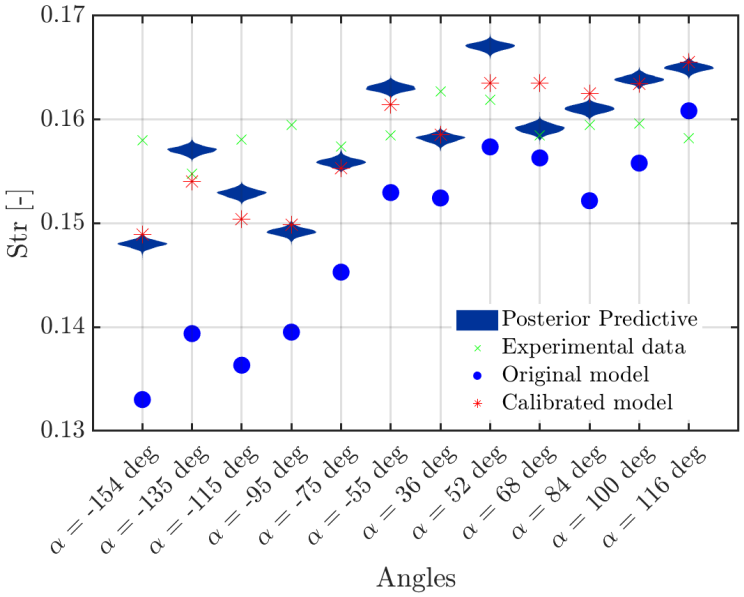

Figure 6.7: Calibration results for the TU Delft experiment

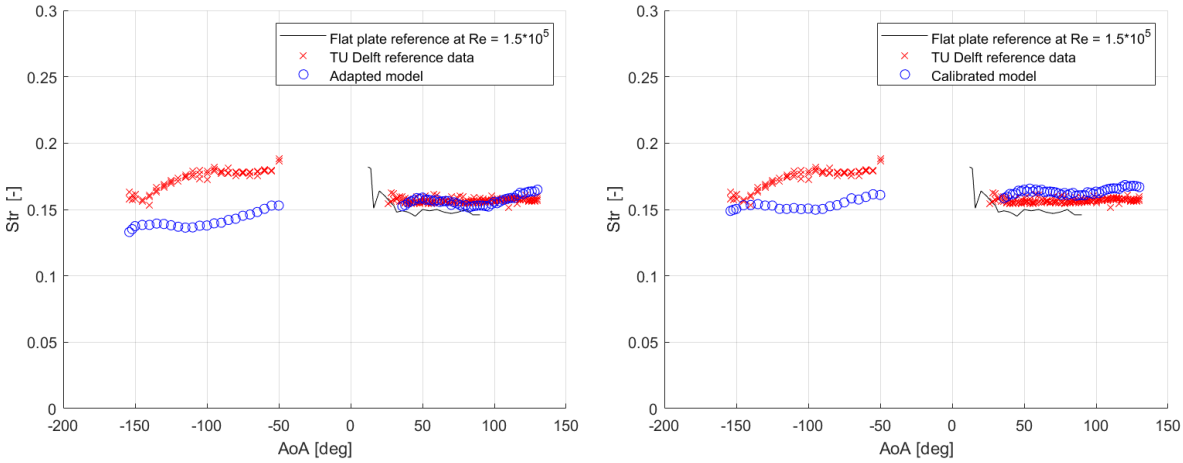

(a) TU Delft comparison before calibration

(b) TU Delft comparison after calibration

Figure 6.8: Effect of calibration on TU Delft experiment

Similarly to the DNW case, the experiment from TU Delft is also considered in Figure 6.7 and Figure 6.8. In terms of the calibration angles, the first of these images shows that for most cases the prediction of the model is improved. This is especially true for the negative

angles of attack, where the original model deviated quite substantially from the experiment. The calibrated model shows much better performance in this area.

This conclusion also applies to the entire range of angles shown in Figure 6.8. There it is shown that for negative angles of attack, the shedding frequency is increased significantly. Additionally, the downward trend with decreasing angle of attack has been reduced on this side. This results in a much more constant selection of projected Strouhal numbers for negative angles of attack.

The prediction of the calibrated model on the positive side of this image does appear to have suffered slightly. However, the prediction of the model in this range still seems very much adequate.

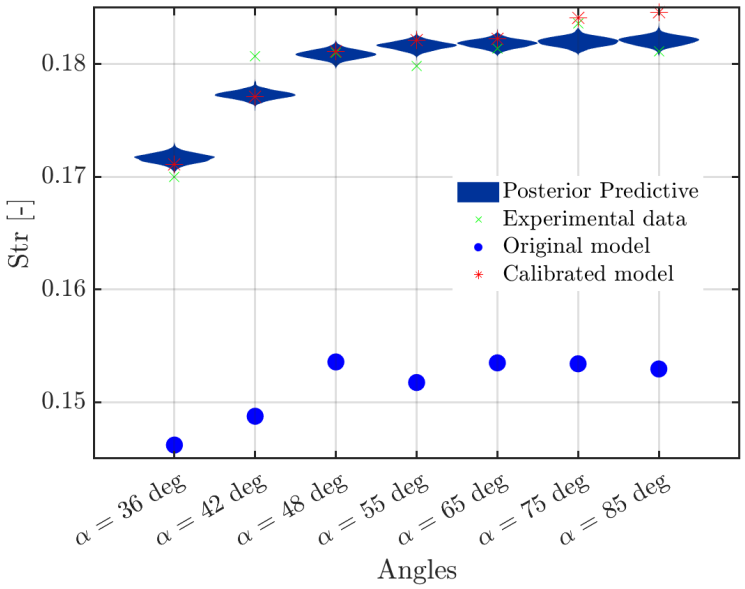

Figure 6.9: Calibration results for the NACA 4412 experiment

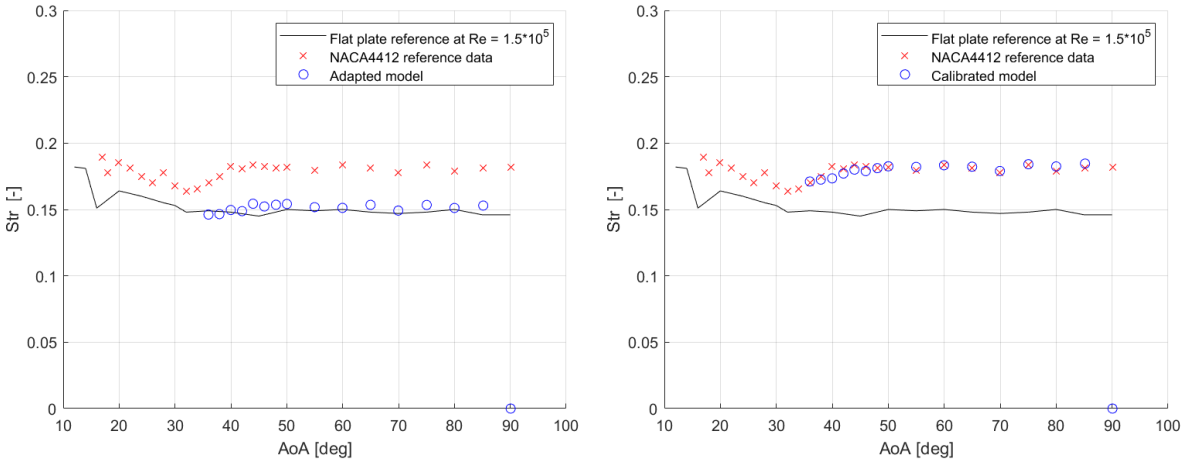

(a) NACA 4412 experiment comparison before calibration

(b) NACA 4412 experiment comparison after calibration

Figure 6.10: Effect of calibration on NACA 4412 experiment

Finally, the calibration of the NACA 4412 airfoil can also be considered. The results of this calibration are shown in Figure 6.9. In this experiment the experimental data varies more from the original model compared to the other experiments. In Figure 6.9 it is shown that it is possible to move the results of the dynamic stall model to the experimental values using the proposed calibration method.

In Figure 6.10 the shedding frequencies are compared for all higher angles. From this it is evident that the results are greatly improved by the calibration. It should be noted that this experiment only considers positive angles of attack. Therefore, any asymmetric effect of changing the parameters is not considered. This could mean that the provided calibrated result is not valid for the same airfoil at negative angles of attack. However, more experimental data would be required to draw that conclusion.

Based on the calibrations shown in this section, new model parameters can be defined for each experiment. This is done by considering the Maximum-a-Posteriori (MAP) estimate for each parameter. This refers to the value for each model parameter that has the highest probability after assessing the chains resulting from the calibration. The results for each experiment are shown in Table 6.4. The calibration containing both the DNW and the TU Delft result is presented in the next section.

Table 6.4: MAP estimate for each of the experiments

	P_1	P_2	P_3	P_4	P_5	P_6
DNW	1.4497	3.7527	-0.0160	0.7000	12.2609	0.1084
TU Delft	0.5662	3.1720	-0.0048	0.6997	9.5010	0.1850
NACA	0.9508	3.2713	-0.0082	-0.0071	12.6575	0.1850
DNW and TU Delft	0.55	2.6392	-0.0044	0.7000	16.6822	0.1727

From the MAP estimates for each of the experiments, it appears that the different calibrations do not converge to the same model parameters. Some possible implications of this will be discussed next.

The first possible reason for this observation is simply that some of the model parameters are dependent on the airfoil shape. It was already observed in previous chapters that the shape of the airfoil does appear to influence the shedding behaviour in deep stall conditions. Therefore, it could be possible that to accurately model this behaviour some parameters should be changed based on the airfoil. The effect of the different steady polars is already included in the model definition through $\Delta C_{l,pot}$. However, it might be the case that more airfoil specific tuning is required. This discussion relates to changing the model parameters through some other results, similarly to the ONERA model.

Another possibility is simply that the model has several combinations of parameters that are able to reduce the error to similar degree. For example, it appears that if P_1 is large in the MAP estimate, P_3 is also increased in magnitude. This could suggest that these parameters are linked in the calibration. This is also supported by the correlation matrix matrix produced by the calibration. These matrices do produce entries in the range of 0.1 to 0.5 for several parameters. Therefore, the resulting values of many of the parameters are linked. If in addition to this, several combination of the model parameters produce similar errors, it is possible that the calibration of the model converges to very different results for each experiment.

The final consideration for the difference in the calibrated results is the fact that each calibration only considered one experiment. As such, the optimal value for the calibrated model might be overtuned for this specific data set. Therefore, the next section will consider more than one experiment in the calibration.

6.4 Final calibration

For the final calibration the same procedure is used as for the individual calibrations. It also uses the same surrogate models and prior distributions. The only difference is the number of data sets considered in the procedure as more than one experiment will be used.

To select the experiments the purpose of this calibration should be considered. The goal is to produce a more generally applicable model for predicting the vortex shedding frequencies present at larger angles of attack. For this purpose one would want to consider as many experiments as possible. However, these experiments should be completely representative of the range of applications. The NACA 4412 experiment considered here only includes positive angles of attack. Hence, it is possible that including it in the combined calibration provides a false sense of security at negative angles of attack. This is also supported by the fact that some parameters were observed to have an asymmetric effect. As a result, including a one-sided experimental reference could skew the result of these parameters unjustifiably. Therefore, only the experiments which include both positive and negative angles are considered. These are the DNW and TU Delft experiment.

Before the results of the calibration are presented, the applicability of the result should be considered. Only two experiments will be used to obtain this model. Therefore, no guarantee that the result is applicable to more situations can be provided. However, both airfoils used are quite similar in terms of geometry. Hence, it might be possible to produce a model that can be applied to other similar airfoils.

Based in the selected experiments and procedure, the calibration was performed for the DNW and TU Delft experiment combined. This calibration also converged for the same settings as were used in the individual calibrations. The results of this calibration are shown in Figure 6.4.

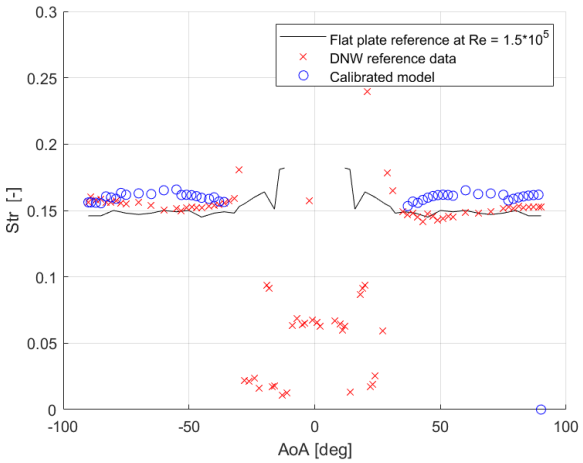

(a) Combined calibration applied to DNW experiment

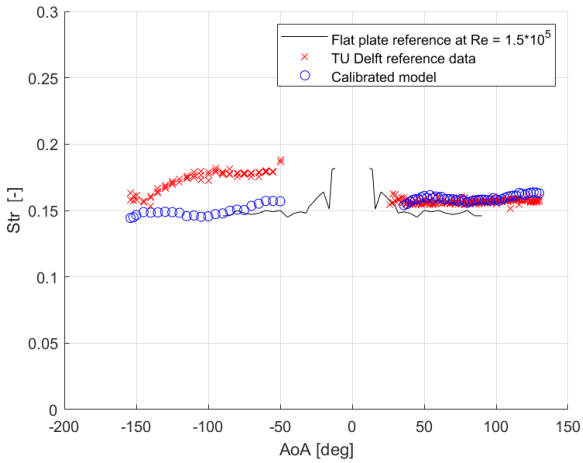

(b) Combined calibration applied to TU Delft experiment

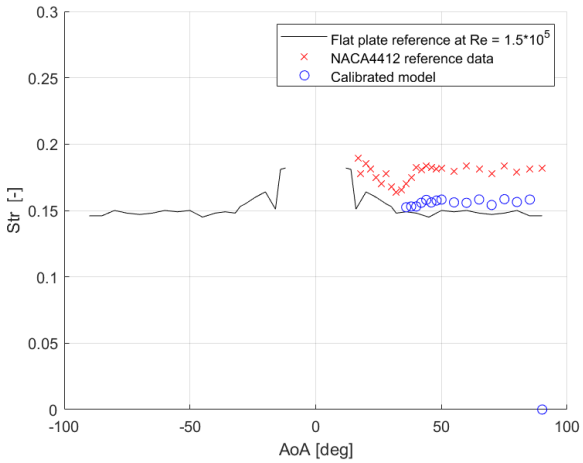

(c) Combined calibration applied to NACA 4412 experiment

Figure 6.11: Application of the combined calibration to all experiments

In the images shown in Figure 6.4 it can be observed that the combined calibration has altered the results of the model. This change is obtained by altering the coefficients to the ones shown in Table 6.4. Typically, this appears to be an improvement from the original formulation. The calibrated results appear to be quite close to the results from the TU Delft calibration, especially for P_1, P_4, and P_6. Since these are 3 out of the 4 influential parameters that were identified in the sensitivity analysis, the results indeed are similar to the TU Delft calibration.

Having shown the results of the different calibrations, it is important to also consider the performance of the different models based on their errors. For this purpose the L_2 errors are considered for all cases. The results of this are shown in Table 6.5. Once again only the higher angles of attack, above 35 degrees, are considered in this analysis.

Based on the errors shown in the table, several observations can be made. Firstly, the individual calibrations perform the best for each of the experiments. This is to be expected, as in those cases only the data from that specific experiment was considered in the calibration.

In the combined calibration it can be observed that the performance in the case of the

Table 6.5: Errors produced by different version of the adapted model

Experiment	DNW	TU Delft	NACA 4412
Adapted model	0.0251	0.0186	0.0534
Individual calibration	0.0238	0.0130	0.0455
Combined calibration	0.0251	0.0141	0.0511

TU Delft experiment is still improved significantly. This is the result of the calibration converging towards a definition more similar to the one obtained in the individual TU Delft calibration. However, for the DNW experiment it performs similarly to the original formulation. The improvements made in the TU Delft case are apparently sufficiently large to justify the lack of improvement in the DNW experiment.

The shedding frequencies of combined calibration and DNW calibration are similar. However, their model definitions appear to be vastly different. This is supportive of the idea that the construction of this model allows for obtaining very similar results through a variety of parameter combinations. This observation makes it difficult to determine if any of the parameters are airfoil dependent. If one of the parameters is airfoil dependent, it could be possible that a different combination of parameters would obtain a similar result. Therefore, it is not possible to identify any parameters as airfoil dependent as of now.

The fourth observation that can be made is the fact that the calibrations appear to move towards to limits imposed on the model parameters is several cases. This could indicate that a more suitable definition of the model could exist. Unfortunately, the further improvement of this specific model definition is deemed to be outside of the scope for this project.

Additionally, when the combined model applied to the NACA 4412 experiment as well, the error is also reduced. The fact that this calibrated model is also more suitable for the experiment that was not used in it's creation is promising for the general applicability of this model. This is especially true considering that the NACA 4412 airfoil is very different from the two other considered airfoils.

In conclusion, the model presented in this section is based of two different experiments. Using the presented calibration method, the prediction of the vortex shedding frequencies was generally improved. This was also the case when the model was applied to the experiment that was not included in the calibration. Therefore, this model is suggested to be a potentially suitable model for the prediction of shedding behaviour in airfoils. However, some more validation should still be performed to ensure the validity of the model. Especially for airfoils with a very different geometry from the ones used in the DNW and TU Delft experiments.

Chapter 7

Conclusions and recommendations

The goal of the presented research was to investigate the applicability of current dynamic stall models to vortex shedding on airfoils. This behaviour would occur for stationary airfoils in deep stall conditions. Several dynamic stall models were tested against such conditions in three experiments. Additionally, an adapted model was proposed to model this behaviour. In this process several conclusions were drawn and steps for future work were identified. In this chapter these are both presented.

Conclusions

In the presented research three wind tunnel experiments were considered that examined the behaviour of airfoils in deep stall. These were performed in wind tunnels from DNW, Tu Delft, and the AmirKabir University of Technology. For these experiments, the vortex shedding at constant inflow angle and velocity was the main area of interest. In their results the frequency of this shedding behaviour was analysed.

Before the frequency could be examined, the effect of the blockage created by the different wind tunnels was explored. From this, it was found that, at large blockage ratios, the effect on the shedding frequency can be significant. In those cases corrections are required. Therefore, some experiments were corrected based on the blockage ratio. This allowed for vortex shedding frequencies that matched the expected results from literature in all experiments. However, the TU Delft data was not corrected as the blockage ratio was relatively low. This experiment had a maximum blockage ratio of 12%, compared to the 25% found in for example the DNW experiment. Two reasons were provided for this exception. Firstly, no blockage corrections are typically required below 10%. Additionally, the uncorrected results already show good correspondence with expected results based on literature. Therefore, no blockage correction appeared to be needed in this experiment.

The first step after obtaining the results from the experiments was to compare the three different results. This was done by examining the projected Strouhal number. From this it was concluded that the different airfoils showed a near constant shedding frequency at higher angles of attack. High angles in this context refer to angles for which the airfoil is placed in deep stall conditions and the shedding behaviour becomes dominant. For the experiments considered in this report this referred to angles of attack larger than 30 degrees. The constant response was an expected result based on literature. However, it was

found that the value of this constant result varied between 0.15 to 0.18 for the different experiments. Therefore, it is suggested that airfoil shape or operating conditions can still have an influence on the shedding behaviour of an airfoil. The different facilities and test setups could also have affected the results. It should be noted that the variation between the experiments was contained within values that are expected based on literature.

After the results of the experiments had been considered, they were compared to the predictions made by commonly used dynamic stall models. Three models were selected for this comparison, the Snel, Adema, and IAG models. These models were included as they are suitable for modelling second order effects like vortex shedding. The predicted shedding frequencies for each these models varied greatly. The Snel model provided a non-periodic response for all considered cases. This meant that the Snel model definition is not at all suitable for predicting vortex shedding behaviour on stationary airfoils. The IAG model did provide some periodicity in the response. However, this was quickly damped after a couple of seconds for most inflow angles. Hence, this model did also not represent the observed behaviour. Finally, the Adema model did provide a periodic response that remained undamped for most positive angles of attack. However, this response contained vastly different frequencies compared to the experiments. Additionally, the Adema model did not provide a periodic response for negative angles of attack. Therefore, none of the considered dynamic stall models were able to predict the vortex shedding frequencies with a reasonable accuracy.

Therefore, adaptations were proposed which aimed to improve the prediction of the shedding frequencies using a new definition for a dynamic stall model. Despite some major differences with the experimental results, the Adema model was considered to be the most suitable basis for this. Using the model definition presented by Adema, the frequency and damping coefficients used in the differential equations were altered to improve the performance. Several options were explored in order to better match the predicted shedding frequency to the experiments. These new options firstly altered some of the model coefficients, while maintaining the original formulation. Additionally, new terms were added to the original description of the model to further improve the results. These changes allowed for a much more constant range of projected Strouhal numbers for all simulated angles of attack. Hence, a model definition was proposed that was able to predict the shedding frequencies with much higher accuracy.

However, dynamic stall models are often applied to pitching airfoils at more moderate angles, between 10 to 30 degrees. For such cases, the adapted model performed very poorly compared to the original formulation. To assess the performance, several cases from the OSU database were considered. Based on this comparison, a blended model was introduced. This model would use the newly proposed definition at in deep stall conditions, while maintaining the original Adema definition at lower angles of attack. The combination allowed for only a small decrease in accuracy for the pitching airfoil cases from the OSU database. However, at the larger angles the improvements for predicting the shedding frequency were maintained. This approach showed promising results for creating a single model that could be applied to the different operating ranges. When applied this method allows the proposed model to function as an extension, which can be applied when dominant aerodyamic behaviour changes.

The blending of the model has been defined through a single, airfoil dependent angle. This angle was determined based on the steady polar of each airfoil. The currently used

definition was set to the angle at which the normal and lift coefficient start to deviate significantly in the steady airfoil polar. However, some undesirable oscillations are not eliminated using this approach. Hence, a more accurate method from changing the definitions should still be investigated.

Based on the proposed model a sensitivity study was performed which considered the prediction of the shedding frequencies. This is done using the uncertainty quantification tool UQLAB. The sensitivity module in this tool allowed for an automated assessment of the relative influence of the model parameters. These results were analysed and presented. From this analysis, four parameters were identified as being significantly more influential for adapting the vortex shedding frequencies predicted by the model. These parameters showed different effects at specific angles of attack. This information should provide a good basis for any future adaptations of the model.

Next, the proposed model was calibrated using a Bayesian inversion approach. The uncertainty quantification tool UQLAB was once again used for this. The calibration allowed for an increase in accuracy for the predicted vortex shedding frequencies for the airfoils in deep stall conditions. For each of the experiments an individually calibrated model was presented. The TU Delft and DNW experiments were also combined to create a calibration based on two data sets. This calibration increased the overall accuracy of the dynamic stall model in terms of the vortex shedding predictions. These calibrations also provide a numerical basis for the selection of the coefficient values used in the equations.

During the calibration procedure it was observed that different combinations of model parameters could produce similar results in terms of shedding behaviour. This indicates that a change in one model parameter can be compensated by altering another parameter. Hence, a similar error is achieved through a variety of model parameter combination. As a result, a large variation in model parameters was found, with a limited variation in errors. Hence, the definition of this model could be difficult to perform in a general sense in the future. Additionally, it is possible that some of the parameters in the model are actually dependent on the airfoil shape. This would also be supported by the observed differences in shedding behaviour between the experiments.

The presented calibrated model considered two experiments. One experiment was excluded, as it did not include measurements for positive and negative angles of attack. Because of the limited number of experiments, it is not possible to present and use the model as a general method at this stage. However, the presented method based on UQLAB could be used to produce a general calibration, if more experiments are available.

Additionally, both airfoils used in the combined calibration are similar in terms of camber and thickness. Hence, this gives the model more validity in predicting the vortex shedding frequencies of other similar airfoils. Unfortunately, another validation experiment should be included to be certain of the accuracy for this approach.

In conclusion, based on three experiments the prediction of vortex shedding frequencies using dynamic stall models was considered. Current dynamic stall models were found to not be suitable for predicting these frequencies. Therefore, an adapted model was constructed and calibrated based on experimental results. This models greatly improves the prediction of vortex shedding frequencies. The accuracy when applied to pitching airfoils at moderate angles of attack was decreased slightly. The validity of this model for more airfoils remains to be investigated. However, the approach outlined in this research has been shown to provide promising results for creating such a model.

Future work

Based on the information presented in this report, some areas of future research were identified. These are outlined at various stages throughout the report and are recapped in this section.

The first topic that warrants further attention is the development of the newly presented dynamic stall model. In this report several steps have been taken to improve the prediction of the vortex shedding frequencies. These included changes to the structure of the model, as well as adapting the values of the model parameters. Both of these areas could be further explored in an attempt to improve the predictions of the vortex shedding frequencies. Some structural changes were considered in the creation of the presented model. However, it is possible that a more suitable definition could be found. Additionally, the calibration of the model parameters could be continued. This could be done by for example including more experiments or by covering a large design space of the input variables.

In addition to continuing to improve the prediction of the shedding frequency, the time response of the model in vortex shedding scenarios could be considered. In this report the shedding time response has not been included in the creation of the dynamic stall model directly. However, it was observed that the changes to the model parameters also affected the magnitudes of the oscillations. For the model to be applied in structural simulations, these could be of importance. Therefore, including some further analysis of the time domain could be a good addition to the process of developing an improved dynamic stall model.

The third aspect of the model that can be investigated in more detail is the blending with the original model. In the current model this is done with a sudden change in definition at a defined angle of attack. The goal of this shift is to use the original definition at moderate angles of attack and the adapted model in deep stall conditions. This angle was determined based on a limited set of experiments and as such might not be a suitable method for general application. Other methods of blending the models could also be explored. For example, blending the model over a range of angles or blending the definitions based on the movement of the airfoil could be more suitable options. This second option could be a viable option as the frequencies observed in the moving airfoil cases were lower compared to the stationary cases. Including such observations in the blending approach could be beneficial.

Fourthly, the general applicability of the model is identified as an area of future research. In this report a limited number of experiments were considered. Therefore, before applying this model in more cases, the performance of the model should be compared to a larger number of data sets. This would greatly improve the number of cases the adapted model could be applied to with confidence. The presented calibrated model only considered two airfoils of fairly similar shape. Including different airfoils in this analysis would be beneficial for the general validity of the model. However, it should be noted that the presented model still performed quite well for the third experiment. This does indicate some potential present in the current definition.

In addition to the lack of available validation data, the variation between the different experiments could also be considered. In this report three different experiments of vortex shedding airfoils were considered. All of these provided different results in terms of the shedding frequencies. Typically, it is considered that airfoils at large angles of attack

behave as flat plates. However, the differences between the airfoils considered could be a reason to explore a link between airfoil geometry and vortex shedding in more detail. This exploration could also prove beneficial for the validation of the dynamic stall model as the presented model provided less variation between the different airfoils.

Apart from research into the presented dynamic stall model, several other areas of research were also identified in the process. The first of these was outlined during the analysis of the results of the DNW experiment. In this chapter it was found that the onset of vortex shedding appeared to be predicted by the base pressure coefficient. When this parameter becomes larger than 1.4 for both positive and negative angles, the onset of vortex shedding appears to take place. A similar result has been observed for another airfoil experiment and for cylinders in the past. Therefore, it could be worthwhile to investigate if this conclusion is generally applicable to more shapes. This could potentially even be used in the blending of the proposed dynamic stall model.

Another area of research that was identified in the process, is the effect of blockage in a wind tunnel on the vortex shedding behaviour. In the DNW experiment the blockage was found to have a significant effect that required a correction. However, the TU Delft experiment appeared to not need a correction. This was explained by the difference in blockage ratio between the two experiments. To assist in the design and analysis of vortex shedding experiments it could be worthwhile to further investigate under which conditions a correction is required.

Appendices

Appendix A

Other results DNW experiment

A.1 Unsteady balance data analysis

In order to compare the response of the loading coefficients in time, the force balance data has to be extracted from the provided data. This data contains the voltage measurements for all 6 of the strain gauges. To obtain force data from these a calibration matrix is used, Figure A.1. Apart from the aerodynamic loading, the balance measurements also contain the loading as a result of the weight of the model. This weight was found to be 254.5 N when wind off measurements were performed.

	X1 [V]	Z1 [V]	Z2 [V]	X2 [V	Z3[V]	Z4[V
Range	+/- 490 N	+/- 981 N	+/- 981 N	+/- 490 N	+/- 981 N	+/- 981 N
X [N]	-50.8745	-1.18292	0.662886	50.6845	-0.312009	0.850318
Z [N]	-0.165609	98.9848	98.4784	0.186838	98.6464	97.9918
m [Nm]	-0.0220932	-11.281	11.382	0.015238	-11.7335	11.614

Figure A.1: Calibration matrix from DNW experiment

For verification of the extraction of the balance measurements, the averages of the time resolved signal can be compared to the provided average force coefficients in the data. For this it should be noted that the uncorrected data will be used as the results from the balance also do not contain wind tunnel corrections.

As a first step, the correct definition for X an Z that are used in the force balance had to be examined. This was done by first examining the averages of voltages measured by the strain gauges. In Figure A.2, the resulting averages are shown for each angle of attack. From the image it is clear that all strain gauges in Z direction are generally increasing in magnitude with angle of attack. Since each of the gauges has a positive calibration coefficient, this would suggest that the force in Z direction keeps climbing with angle of attack. This behaviour is characterise of the normal force, as is seen in Figure 3.4. Additionally, since a negative signal is measured at positive angles of attack it would seem that the balance Z axis is located downwards from the model when placed at zero angle of attack. Having defined the Z axis used in the force balance, the X axis can now also be found. Using a similar approach it is found that this axis is placed along the airfoil, from leading to trailing edge.

This definition of the axes of the force balance means that the axes rotate with the airfoil as the angle of attack changes. As the force balance is described as being contained within the turntable used in the experiment this is deemed a reasonable result.

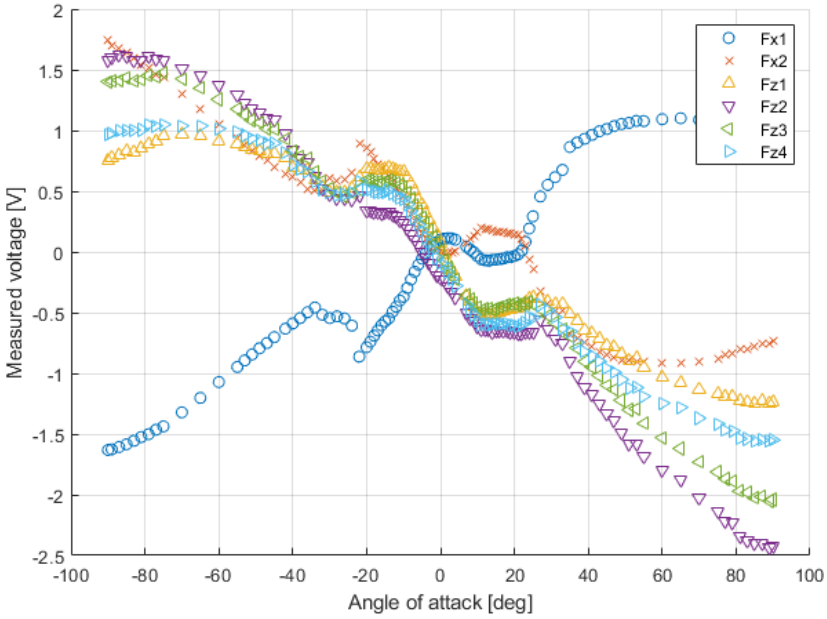

Figure A.2: Average voltage from each of the strain gauges

Having defined a direction for the measurements obtained from the balance readings and the weight force of the airfoil. These can be combined in order to obtain the aerodynamic loading from the data. In the pre-processing of the data a "Zero Value" is subtracted from the measured voltages. This value is obtained at zero angle of attack and without any airflow. Therefore, it contains the weight of the airfoil at these conditions. As a result the weight correction has to contain the difference between this correction and the actual contribution of the weight force. This gives a correction scaling with $sin(\alpha)$ in the tangential direction. Additionally, the correction in the perpendicular direction scales with $1-cos(\alpha)$. As a result, no correction is performed at zero angle of attack, as this should already be contained in the subtracted "Zero Value". When this process was initially performed the difference between the average loading obtained with this method and the loading provided was quite significant, Figure A.3a and Figure A.3b.

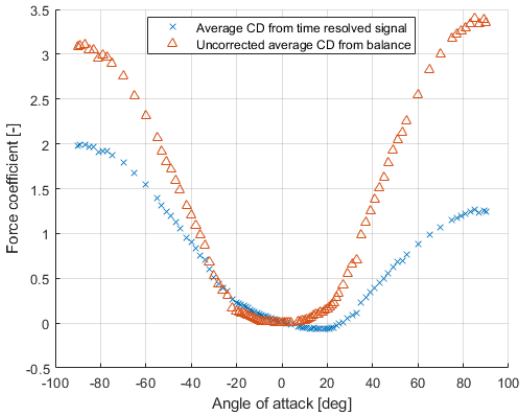

(a) Initial comparison of drag coefficient

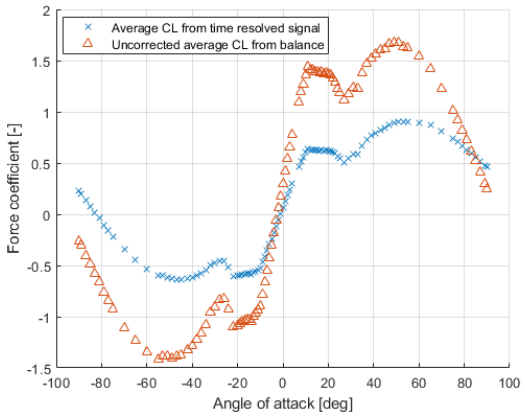

(b) Initial comparison of lift coefficient

Figure A.3: Initial comparison of extract CL and CD

However, the results obtained from the balance signal are still vastly different compared to the provided average coefficients. This difference can largely be attributed to a voltage divider that was used in the lines of the data acquisition system. This divider was required as the range of the dynamic data acquisition system was half of that of the standard system. Unfortunately the presence of this system was not discussed in the documentation of the experiment. Instead the information was obtained by contacting someone who contributed to performing the experiment. Based on this observation, the voltages obtained from the balance signal should be multiplied by 2 before being considered in the calibration matrix. When this is done the agreement between the time resolved balance signal and the provided coefficients is much greater as shown in Figure A.4a and Figure A.4b.

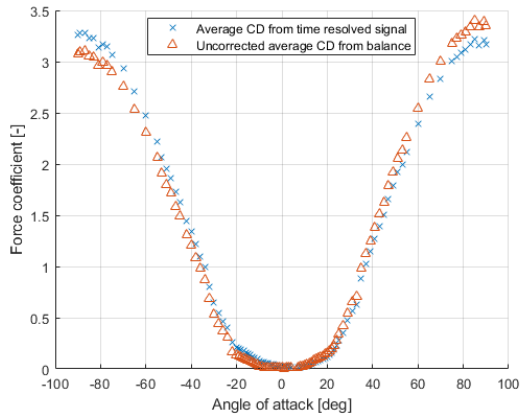

(a) Comparison of drag coefficient after doubling voltage signal

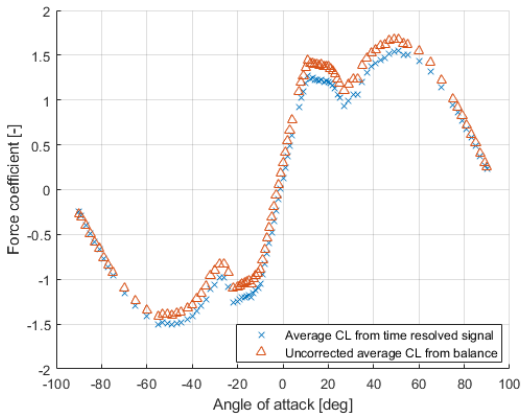

(b) Comparison of lift coefficient after doubling voltage signal

Figure A.4: Lift and drag coefficient

Despite the better agreement, the resulting loading coefficients are still different. To investigate the reason for this difference, the normal and tangential coefficient were also compared to the provided coefficients. This resulted in Figure A.5a and Figure A.5b. In these images the difference between the average coefficients obtained from the time signal and provided in the data of the experiment is also shown. From these images it can be concluded that a constant shift is present in terms of normal and tangential coefficients.

This shift could be attributed to a slight difference in the assumed value of the "Zero value" that is subtracted from the voltage signal based on the initial value of each sensor. This assumption is supported by the fact that the difference is almost constant for all angles of attack, as such suggesting a origin not related to the loading of the airfoil as this varies drastically.

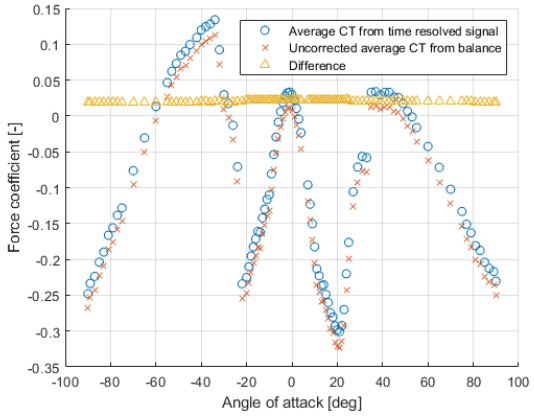

(a) Comparison of tangential coefficient after doubling voltage signal

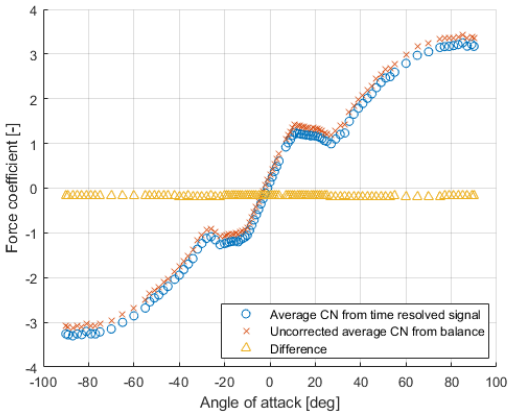

(b) Comparison of normal coefficient after doubling voltage signal

Figure A.5: Normal and tangential coefficient comparison

This shift does not appear to depend on angle of attack and remains constant at a value of around 0.1766 for the normal coefficient and 0.021 for the tangential coefficient. These values will be used to correct the time dependent loading for the DNW in the rest of this report.

Wind tunnel corrections

The time resolved balance measurements contain a direct voltage signal from the strain gauges. Therefore, before comparing the resulting force to the results of the simulations, some corrections have to be applied as a result of the wind tunnel interference. These corrections are based on the effect the presence of the walls have on the flow at the location of the airfoil. The influence on the velocity at the centerline of the tunnel section is shown by Equation A.1 and Equation A.2. Using these equations the correction in the flow direction, which changes the dynamic pressure, and normal direction, which affects the inflow angle. To determine the correction in flow direction, the average is taken of the interference velocities at the leading and trailing edge of the airfoil. The correction on the inflow angle is analysed by evaluating the velocity at the quarter chord point.

$$u_m^i = \frac{1}{2\pi}\int_{-\infty}^{\infty} \frac{(u_t + u_b)\frac{H}{2}}{(\xi - x)^2 + \frac{H}{2}^2} d\xi \tag{A.1}$$

$$v_m^i = \frac{1}{2\pi}\int_{-\infty}^{\infty} \frac{(u_t - u_b)(\xi - x)}{(\xi - x)^2 + \frac{H}{2}^2} d\xi \tag{A.2}$$

In order to verify the implementation of the wind tunnel correction, the described process was applied to the uncorrected data from the DNW experiment. The resulting values

can then be compared to the corrected values that are also provided with the experimental data. The results are shown in Figure A.6. From this the values appear to match quite closely to the expected values.

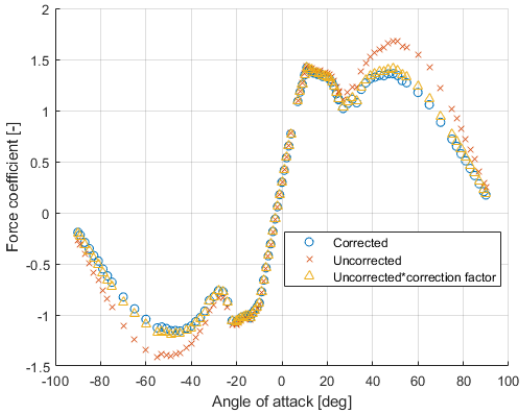

(a) Effect of wind tunnel corrections on the lift coefficient

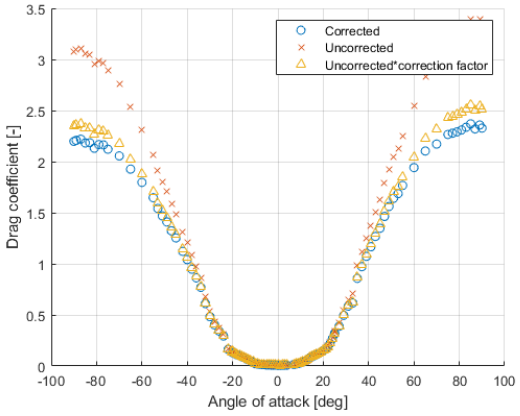

(b) Effect of wind tunnel corrections on the drag coefficient

Figure A.6: Verification of the wind tunnel correction

Appendix B

Verification dynamic stall models

In this chapter, the implementation of several dynamic stall models is discussed. These implementations are verified against other simulations. The definitions of the models can be found in the literature review. The goal of this section is purely to verify the implementation of the dynamic stall model and as such, no comparison to experimental data is performed.

B.1 Original Snell model

The first model that is considered is the original Snell model as presented by Truong [1993a]. To verify this model the simulation results from Adema et al. [2020] were used as a reference. This allowed for the comparison at both low and high reduced frequency. The airfoil used in this report is a NACA4415 airfoil with length 0.457 metres.

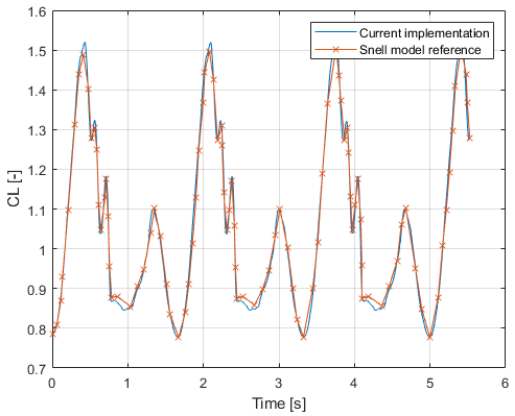

(a) Model implementation at k = 0.0228 with a mean AoA of 14^o and a variation of 10.5^o

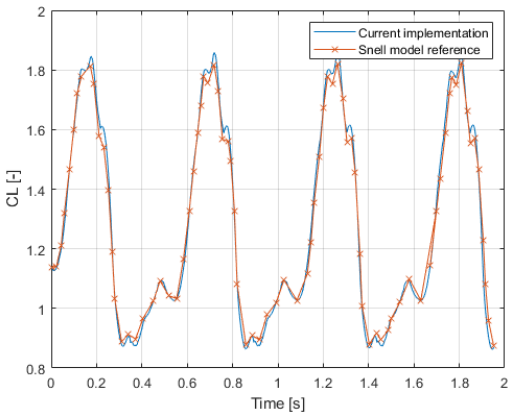

(b) Model implementation at k = 0.0711 with a mean AoA of 18.4^o and a variation of 10.7^o

Figure B.1: Original Snell model verification

In Figure B.1a and Figure B.1b the time response of the implementation of the dynamic stall model is compared to the values obtained by Adema et al. [2020]. From this comparison it can be concluded that the implementation of the Snell dynamic stall model is indeed correct and can be used later on in the project.

Apart from the comparison the other simulation results, the variation around the steady polar can also be examined, this is shown in Figure B.2a and Figure B.2b. In these images a variation similar to the one observed in literature can be seen. This once again help verify the implementation of the stall model when compared to the steady data.

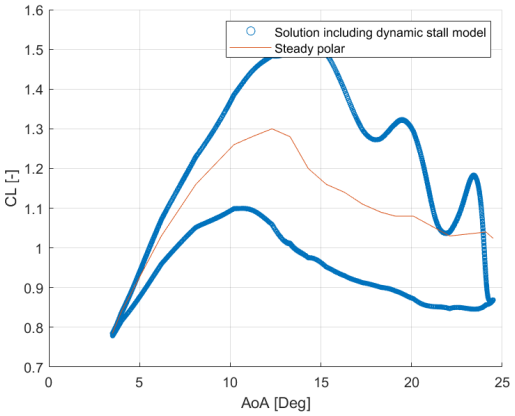

(a) Variation around polar at k = 0.0228 with a mean AoA of 14^o and a variation of 10.5^o

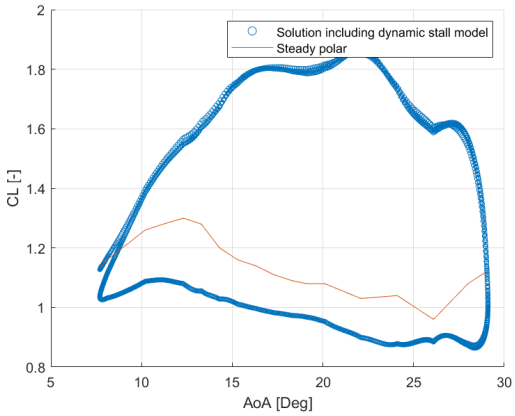

(b) Variation around polar at k = 0.0711 with a mean AoA of 18.4^o and a variation of 10.7^o

Figure B.2: Variations of original Snell model around steady polar

B.2 Improved Snell model

The second model whose implementation should be verified is the improved Snell model presented by Adema et al. [2020]. For this model the same operating conditions can once again be compared in Figure B.3a and Figure B.3b.

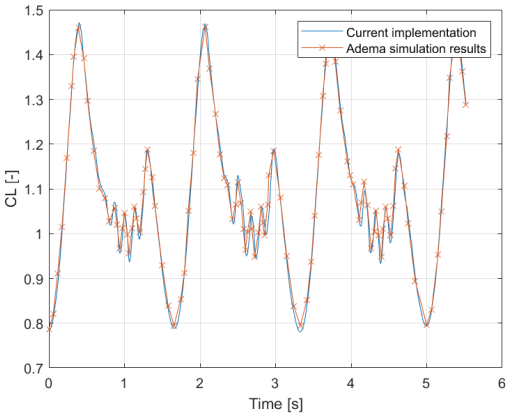

(a) Model implementation at k = 0.0228 with a mean AoA of 14^o and a variation of 10.5^o

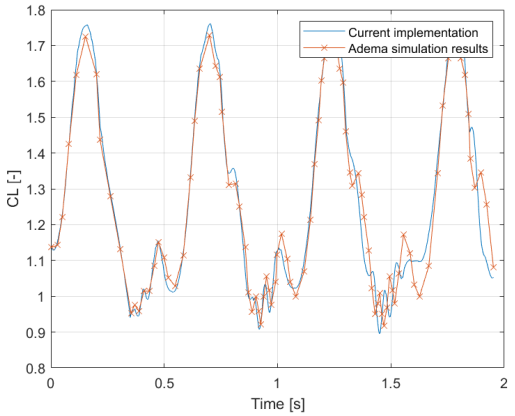

(b) Model implementation at k = 0.0711 with a mean AoA of 18.4^o and a variation of 10.7^o

Figure B.3: Improved Snell model verification

From Figure B.3a it can be concluded that the first operating condition is matched almost exactly. Therefore, the implementation of the model would seem to be correct. However, the differences between the two models shown in Figure B.3b are more significant

despite using the same models. When the code used by Adema et al. [2020] to generate the results was examined, a different definition of the forcing was found, Equation B.1. When this definition was used, the results of the second case were matched much more accurately as shown by Figure B.4b. However, the results of the first case were no longer matched, Figure B.4a.

$$f\,t_2 = 0.1 k_s \left(-0.08 \Delta C_{l,pot} + 1.5\tau \frac{d\Delta C_{l,pot}}{dt} \right) \qquad \text{if } \frac{d\alpha}{dt} > 0 \tag{B.1}$$

$$f\,t_2 = 0 \qquad \text{else}$$

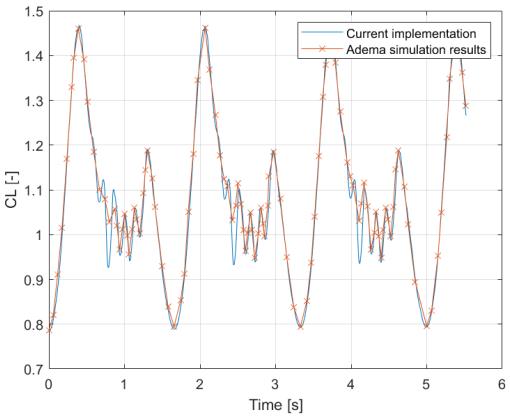

(a) Adapted model implementation at k = 0.0228 with a mean AoA of 14^o and a variation of 10.5^o

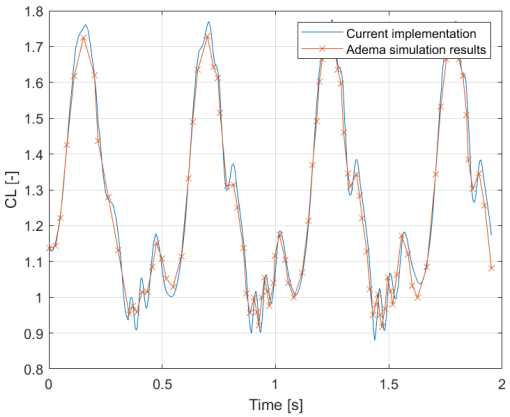

(b) Adapted model implementation at k = 0.0711 with a mean AoA of 18.4^o and a variation of 10.7^o

Figure B.4: Comparison of adapted Adema model to reference implementation

Based on those comparisons it is expected that the settings used to generate the results for the second operating condition (k=0.0711) were different from the ones presented in the paper. However, as the results could be replicated with reasonable accuracy the implementation of the model is expected to be correct. Additionally, it should be noted that in future the definition presented in the paper is used as this is expected to be intended definition. Additionally, the results of both definitions were compared to data used in the construction of the model. As shown in Figure B.5a and Figure B.5b, the definition presented in the paper also produced better results when compared to the reference data.

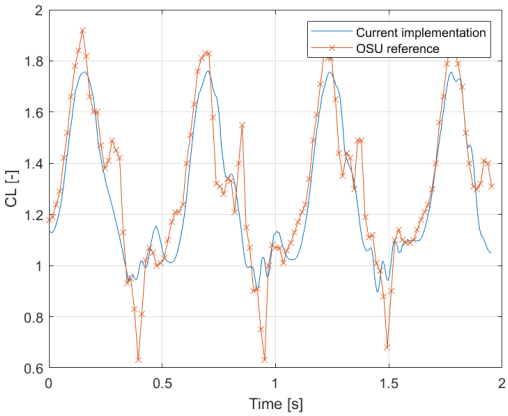

(a) Comparison to reference data using forcing definition from paper

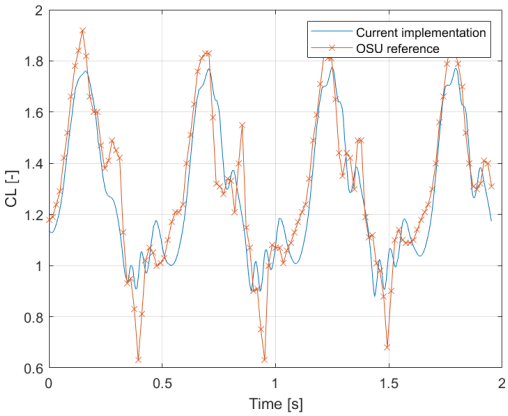

(b) Comparison to reference data using forcing definition from code

Figure B.5: Comparison of the two versions of the Adema model to reference data (k = 0.0711 with a mean AoA of 18.4^o and a variation of 10.7^o)

B.3 IAG model

The final model that is to be verified is the model presented in Bangga et al. [2020]. This model uses a similar second order correction to the Adema model. The main differences being the fact that the equations are normalised and the selected coefficient altered. The first order correction of this model is based on the Beddoes-Leishman model.

To try to verify the model, the results for several airfoils have been provided. This data only contains the final results of the model, combining both corrections. An approximation of the separate effects was obtained by extracting data from a plot in Bangga et al. [2020], where the two corrections are shown separately for the S801 airfoil. Some small error is introduced because of the manual extraction. However, the resulting data should still be feasible to be used for comparison.

In Figure B.6a the first order correction is implemented and compared to the results obtained from Bangga et al. [2020]. From the original comparison it can be seen that the lift coefficient is predicted relatively accurately, except for the end of the upstroke. This difference is likely caused by the inviscid lift curve slope that is used in the model. The exact value that is used in the reference is not known. However, if the value obtained from an inviscid XFOIL simulation is increased by 13% the obtained results are almost identical as is shown in Figure B.6b. Therefore, the discussed inaccuracy is likely caused by this difference in inviscid lift curve slope. In all further discussions the adapted value is used.

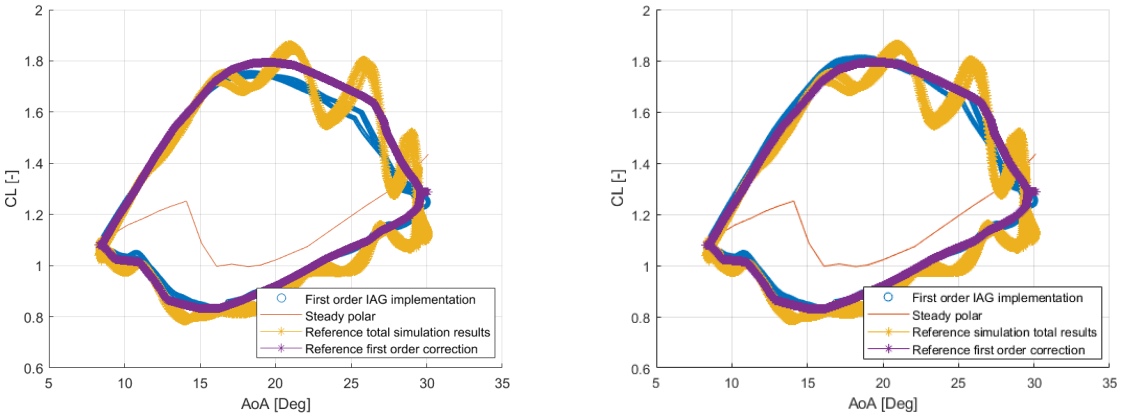

(a) First order correction original

(b) First order IAG correction with higher slope

Figure B.6: Effect of increasing the inviscid lift curve slope

After implementing the second order correction as well, the results of the complete model can be compared for this case. As is shown in Figure B.7a this implementation does show some differences. The main difference is the frequencies that are observed in the response, with the implementation presented here showing slightly higher frequencies in the response.

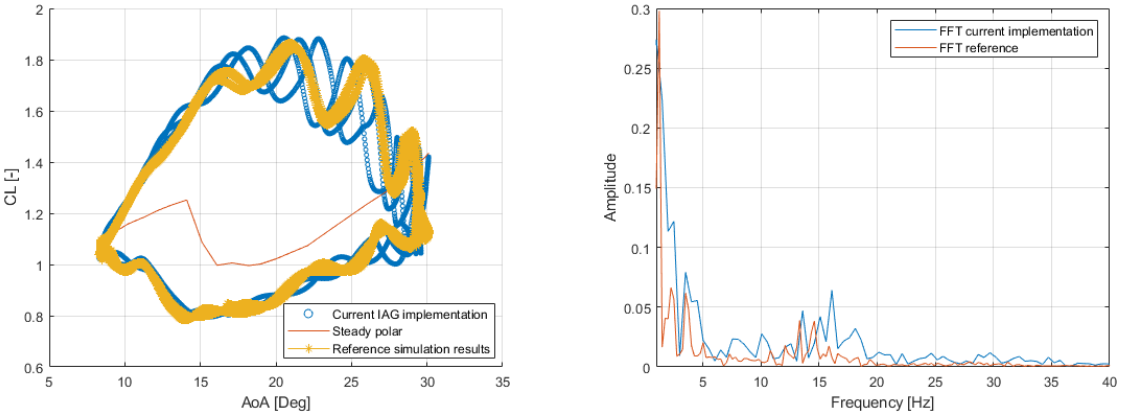

(a) Comparison total correction

(b) Frequency spectrum comparison of current implementation

Figure B.7: Comparison IAG implementation to reference

To study the reason for these differences the original author of the IAG model was contacted. From this discussion it was suggested that difference in the frequencies could originate from the time stepping scheme used in either implementation. In the reference a single time-step solver is used, while the original implementation used a variable time-step. Therefore, the effect of changing this scheme is examined in Figure B.3. Unfortunately, the effect of changing the solver does not seem to affect the results much at all. This likely is the result of the time-step being relatively small already and as such the total error having been reduced significantly already.

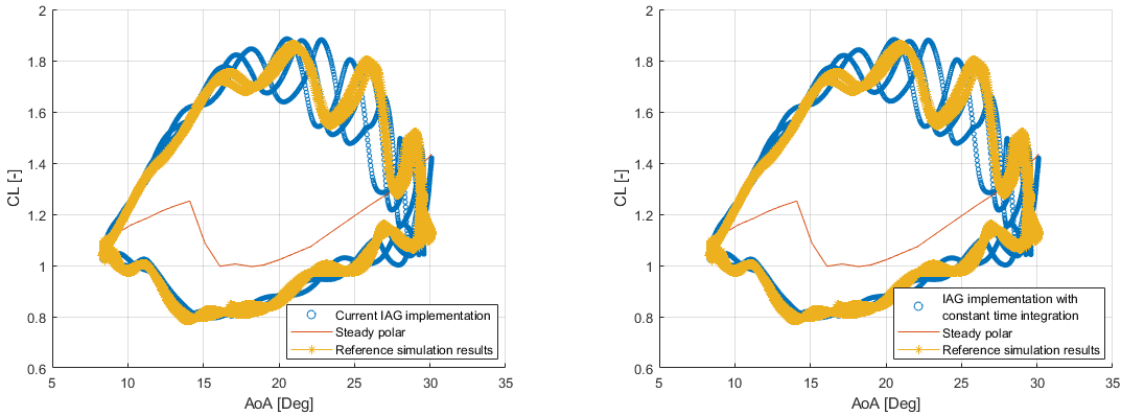

(a) Comparison total correction original integration

(b) Comparison total correction with single time step solver

Figure B.8: Comparison different time integration methods

At this point no further differences between the two implementations have been found. This is largely caused by no intermediate results, reference polar data or source code being available for comparison. Unfortunately this means that the results presented in Bangga et al. [2020] could not be exactly replicated as was the case with the other dynamic stall models. However, the response of the model is similar as was also observed by the author of Bangga et al. [2020]. Therefore, the implementation will be used as a reference for a dynamic stall model which is non-dimensionalised in future comparisons. Although it should be noted that the model could not be completely verified.

Appendix C

Adapting the Adema model, an alternative option

As has been discussed in chapter 5, there are two main differences when the data from the Adema model is compared to the experimental results. The first is the lack of shedding frequencies at the negative frequencies. The second is the large variation of the Strouhal number with angle of attack which is not observed in the data once the shedding behaviour is started. Apart from the adaptation presented in the report and alternative adaptation was also considered. In this chapter, this adaptation is presented.

The alternative option aims to make as few structural changes to the model as possible. This is defined as reducing the amount of terms that are changed or introduced. The chosen definition of the frequency and damping terms are shown in Equation C.2 and Equation C.3.

$$ft_2 = 0.01 k_s \left(-0.04 \Delta C_{l,pot} + 1.5 \tau \frac{d \Delta C_{l,pot}}{dt} \right) \tag{C.1}$$

$$cf_{20} = \begin{cases} 10(k_s sin(\alpha))^2 \left(1 + 3\Delta C_{l,2}^2\right) \left(1 + 280^2 \tau^2 \left[\frac{d\alpha}{dt}\right]^2\right) & \text{if } \alpha < \alpha_s \\ 6\left(\frac{k_s}{sin(\alpha)}\right)^2 \left(1 + 3\Delta C_{l,2}^2\right) \left(1 + 280^2 \tau^2 \left[\frac{d\alpha}{dt}\right]^2\right) & \text{if } \alpha \geq \alpha_s \end{cases} \tag{C.2}$$

$$cf_{21} = \begin{cases} 60\tau k_s \left(-0.01(|\Delta C_{l,pot}| + 0.5) + 2\Delta C_{l,2}^2 \right) & \text{if } \frac{d\alpha}{dt} \geq 0 \ \& \ \alpha > \alpha_s \\ 60\tau k_s \left(-0.01(|\Delta C_{l,pot}| - 0.5) + 2\Delta C_{l,2}^2 \right) & \text{if } \frac{d\alpha}{dt} \geq 0 \ \& \ \alpha < \alpha_s \\ 60\tau k_s \left(-0.01(|\Delta C_{l,pot}| + 0.5) + 14\Delta C_{l,2}^2 \right) & \text{if } \frac{d\alpha}{dt} < 0 \end{cases} \tag{C.3}$$

The first major change is in the frequency definition. Instead of multiplying the Strouhal number with $sin(\alpha)$, a division is used. This greatly increases the frequencies predicted by the dynamic stall model. The choice for this change is based on the definition of the projected Strouhal number, where the frequency is multiplied by $sin(\alpha)$. As was shown in the previous section, the definition of the frequency term in the model directly related to the frequency in the response. Therefore, if this term is divided by a sin the expected

frequency in terms of projected Strouhal number is expected to be relatively constant. It should be noted that the introduction of this division would introduce an instability in the model as for an angle of zero the frequency would be undefined. This is resolved by only using this definition for larger angles of attack. The onset of shedding behaviour at larger angles of attack is also observed in the experimental data.

The second structural change this definition changes the potential difference used in the damping terms as is shown in Equation C.3. Taking the absolute value of the potential difference. The purpose of this change is to have a periodic response for negative angles of attack. For these angles of attack, the potential difference changes sign and as such changes the damping coefficient sufficiently to remove the periodicity from the response. In the definition of the damping term, the change to this new definition is once again only introduced for larger angles of attack. This is done to keep the changes consistent with the frequency term.

The next change is the final structural change introduced in this option and relates to the condition used in the damping coefficient. The definition of this coefficient is dependent on if the angle of attack is increasing or decreasing. Therefore, the change of the definition is located exactly at zero. It was found that using the statement as is shown in Equation C.3. resulted in a more constant result in terms of projected Strouhal number. This is the result of the opposite contribution of the $\Delta C_{l,pot}$ and $\Delta C_{l,2}$ terms being better matched over the range of angles of attack. Therefore, the upper definition was used for stationary angles of attack.

Finally, it can be observed that the values of the coefficients used in the equations have been changed slightly from their original definition. These changes were made to better match the results to the experimental results. The structural changes discussed previously required some more calibration to match those results. This was done through trial and error during which the deviation from the experimental results at larger angles of attack was observed.

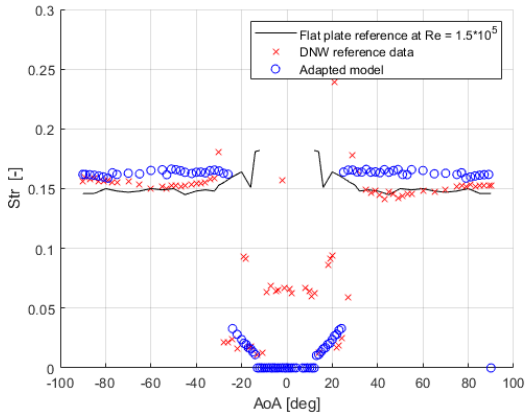

(a) DNW experiment

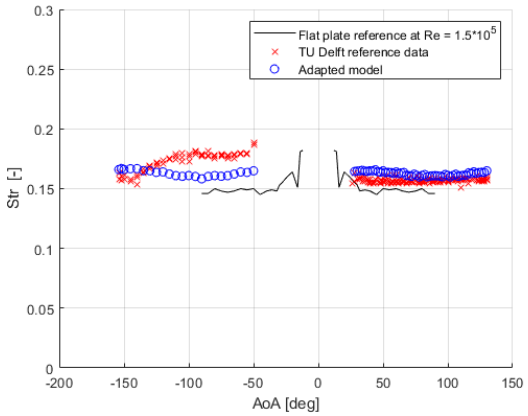

(b) TUD experiment

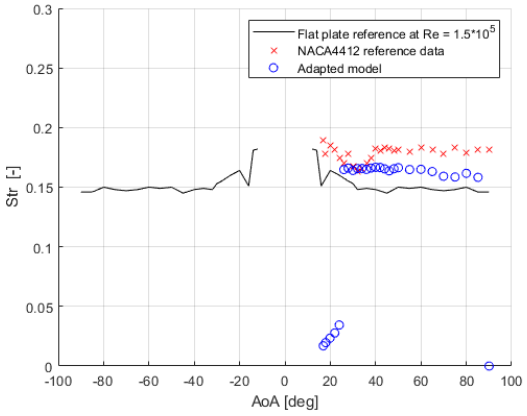

(c) NACA4412 experiment

Figure C.1: Shedding frequencies from the first option of the adapted model

In Figure C.1 it can be seen that the new model definition indeed produces projected Strouhal number in a very constant range. This is to be expected due to the changes made to the frequency component. However, one can also observe that the different airfoils produce almost identical results for all angles of attack. This is the result of the relative size of the frequency component, cf_{20} compared to the damping component, cf_{21}. Since, the frequency term has been increased significantly and the damping term is largely unaffected in terms of magnitude, the balance has shifted. This results in a very similar response for all airfoil cases. Since the responses of the different airfoils have been found to vary, this is not a desirable property.

Appendix D

CFD comparison for stationary airfoil

So far experimental results have been used to compare to the predictions of the model. However, simulations are also often used to predict the aerodynamic performance of airfoils. In this chapter a simulation result is compared to the outcomes of the experiments and the predictions of the dynamic stall model. For this purpose the results of the CFD analysis of a stalling airfoil are used.

D.1 CFD

For this research a CFD simulation applied to a range of stationary operating conditions is required. However, in research CFD is often used for a single angle of attack as is done in for example Skrzypiński et al. [2014] or a moving airfoil as is considered in Meskell and Pellegrino [2019]. Such investigations however do not cover a range of stationary operating conditions as is required. Therefore, no large amount of reference data could be found.

However, in Pellegrino and Meskell [2013] the shedding behaviour of the S809 airfoil is considered using an unsteady RANS simulation. This is done for a range of angles of attack as is shown in Figure D.1. These results could be used in the further validation of the produced dynamic stall model.

In the comparison to the CFD simulation, the projected Strouhal number is once again considered. Using this parameter the CFD results are compared to the calibrated model that was presented in the previous chapter. The results of which are shown in Figure D.2.

From the comparison of the projected Strouhal number it is clear that the results from the presented calibrated model deviate significantly from the CFD data. This could be attributed to the fact that this research has not been included in the development of the model. Therefore, these results might indicate the proposed model is not generally applicable to more airfoils.

However, another option could potentially explain this discrepancy. The CFD results used in this comparison are not validated against experimental results themselves. As a result, a deviation from the expected value could also be introduced in the CFD results. This could also be supported by the fact that the CFD results produce lower projected Strouhal numbers compared to the reference of a flat plate as well as other experiments. The values associated with the CFD are actually lower than the ranges proposed by literature, which predict projected Strouhal numbers between 0.15 and 0.2 at most.

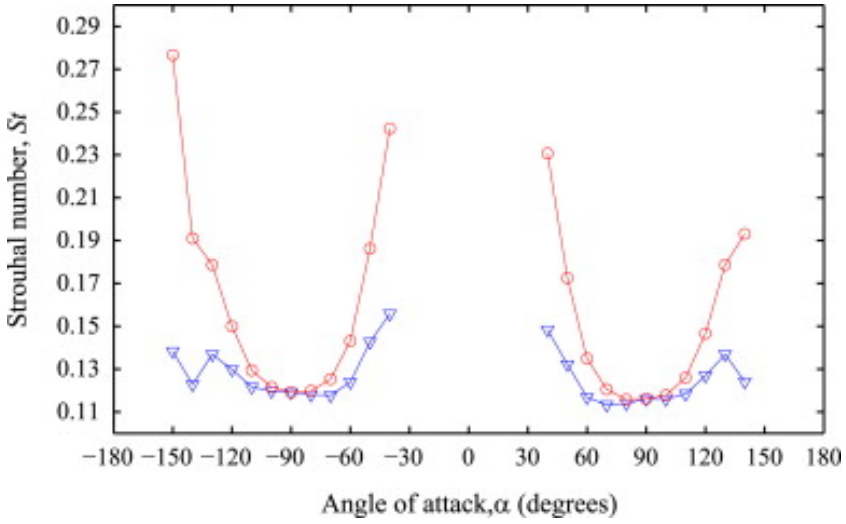

Figure D.1: Simulated Strouhal number (circles) and projected Strouhal number (triangles) for the S809 airfoil, Pellegrino and Meskell [2013]

As of now it is unclear which reason is the cause for the large deviation between the two simulations. Therefore, this could be investigated in the future.

In addition to the discrepancy between the two simulations, the dynamic stall model produces a larger variation of projected Strouhal numbers. In this application the polar obtained from the CFD was used for the dynamic stall model. This polar creates a response with quite some variation in shedding frequency. Therefore, it can be concluded that the polar selected for the airfoil still has a significant influence on the shedding prediction of the dynamic stall model. This behaviour is to be desired as the shedding behaviour of different airfoils has been observed to vary between geometries.

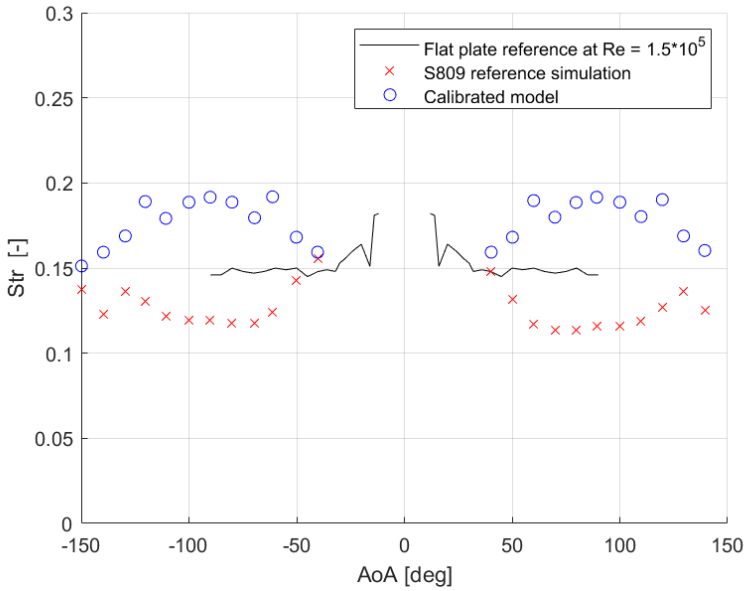

Figure D.2: Comparison of the proposed dynamic stall model to CFD results from Pellegrino and Meskell [2013]

Bibliography

N. Adema, M. Kloosterman, and G. Schepers. Development of a second-order dynamic stall model. Wind Energy Science, 5(2):577–590, 2020. doi: 10.5194/wes-5-577-2020. URL https://wes.copernicus.org/articles/5/577/2020/.

H.B Awbi. Wind-tunnel-wall constraint on two-dimensional rectangular-section prisms. Journal of Wind Engineering and Industrial Aerodynamics - J WIND ENG IND AERODYN, 3:285–306, 12 1978. doi: 10.1016/0167-6105(78)90034-X.

G. Bangga, T. Lutz, and M. Arnold. An improved second-order dynamic stall model for wind turbine airfoils. Wind Energy Science, 5(3):1037–1058, 2020. doi: 10.5194/wes-5-1037-2020. URL https://wes.copernicus.org/articles/5/1037/2020/.

Fanny M Besem, Joshua D Kamrass, Jeffrey P Thomas, Deman Tang, and Robert E Kielb. Vortex-induced vibration and frequency lock-in of an airfoil at high angles of attack. Journal of Fluids Engineering, 138(1), 2016.

Gunjit Bir and Jason Jonkman. Aeroelastic instabilities of large offshore and onshore wind turbines. Journal of Physics: Conference Series, 75:012069, jul 2007. doi: 10.1088/1742-6596/75/1/012069. URL https://doi.org/10.1088/1742-6596/75/1/012069.

Rosario Ceravolo, Alessio Faraci, and Gaetano Miraglia. Bayesian calibration of hysteretic parameters with consideration of the model discrepancy for use in seismic structural health monitoring. Applied Sciences, 10(17), 2020. ISSN 2076-3417. doi: 10.3390/app10175813. URL https://www.mdpi.com/2076-3417/10/17/5813.

Chuan Chen, Jing wei Zhou, Fengming Li, and Endi Zhai. Stall-induced vibrations analysis and mitigation of a wind turbine rotor at idling state: Theory and experiment. Renewable Energy, 187:710–727, 2022. doi: 10.1088/1742-6596/753/4/042019. URL https://doi.org/10.1016/j.renene.2022.01.078.

Jerry M. Chen and Yuan-Cheng Fang. Strouhal numbers of inclined flat plates. Journal of Wind Engineering and Industrial Aerodynamics, 61(2):99–112, 1996. ISSN 0167-6105. doi: https://doi.org/10.1016/0167-6105(96)00044-X. URL https://www.sciencedirect.com/science/article/pii/016761059600044X.

Chang-Koon Choi and Dae Kun Kwon. Wind tunnel blockage effects on aerodynamic behavior of bluff body. Wind and Structures An International Journal, 1:351–364, 09 1998. doi: 10.12989/was.1998.1.4.351.

Arthur Fage, F. C. Johansen, and Horace Lamb. On the flow of air behind an inclined flat plate of infinite span. Proceedings of the Royal Society of London. Series A, Containing Papers of a Mathematical and Physical Character, 116(773):170–197, 1927. doi: 10.1098/rspa.1927.0130. URL https://royalsocietypublishing.org/doi/abs/10.1098/rspa.1927.0130.

Niosha Fallahpour, Mahmoud Mani, and Mohadese Lorestani. Experimental investigation of vortex shedding of an airfoil at post-stall incidences. Proceedings of the Institution of Mechanical Engineers, Part G: Journal of Aerospace Engineering, 0(0), 2022. doi: 10.1177/09544100221112718. URL https://doi.org/10.1177/09544100221112718.

H. Glauert. Airplane Propellers, pages 169–360. Springer Berlin Heidelberg, Berlin, Heidelberg, 1935. ISBN 978-3-642-91487-4. doi: 10.1007/978-3-642-91487-4_3. URL https://doi.org/10.1007/978-3-642-91487-4_3.

Sandeep Gupta and J. Gordon Leishman. Dynamic stall modelling of the s809 aerofoil and comparison with experiments. Wind Energy, 9(6):521–547, 2006. doi: https://doi.org/10.1002/we.200. URL https://onlinelibrary.wiley.com/doi/abs/10.1002/we.200.

S Hauptmann, M Bülk, L Schön, S Erbslöh, K Boorsma, F Grasso, M Kühn, and P W Cheng. Comparison of the lifting-line free vortex wake method and the blade-element-momentum theory regarding the simulated loads of multi-MW wind turbines. Journal of Physics: Conference Series, 555:012050, dec 2014. doi: 10.1088/1742-6596/555/1/012050. URL https://doi.org/10.1088/1742-6596/555/1/012050.

Joachim C. Heinz, Niels N. Sørensen, Frederik Zahle, and Witold Skrzypiński. Vortex-induced vibrations on a modern wind turbine blade. Wind Energy, 19(11):2041–2051, 2016. doi: https://doi.org/10.1002/we.1967. URL https://onlinelibrary.wiley.com/doi/abs/10.1002/we.1967.

Sabrina Henne, Agastya Parikh, Julien Deparday, and Karen Mulleners. Dynamic stall vortex shedding and associated load fluctuations. In 19th International Symposium on the Applications of Laser and Imaging Techniques to Fluid Mechanics, 07 2018.

J.G. Holierhoek, J.B. de Vaal, A.H. van Zuijlen, and H. Bijl. Comparing different dynamic stall models. Wind Energy, 16(1):139–158, 2013. doi: https://doi.org/10.1002/we.548. URL https://onlinelibrary.wiley.com/doi/abs/10.1002/we.548.

S. G. Horcas, T. Barlas, F. Zahle, and N. N. Sørensen. Vortex induced vibrations of wind turbine blades: Influence of the tip geometry. Physics of Fluids, 32(6):065104, 2020. doi: 10.1063/5.0004005. URL https://doi.org/10.1063/5.0004005.

Nicholas Jenkins, A Burton, D Sharpe, and E Bossanyi. Wind Energy Handbook. John Wiley & Sons Ltd, United Kingdom, 2001. ISBN 0-4714-8997-2.

Muhammad A. Khan, Carlos Simão Ferreira, Gerard J. Schepers, and Niels N. Sørensen. Spectral analysis of new mexico standstill measurements to investigate vortex shedding in deep stall. Wind Energy, 23(1):31–44, 2020. doi: https://doi.org/10.1002/we.2409. URL https://onlinelibrary.wiley.com/doi/abs/10.1002/we.2409.

Muhammad Arsalan Khan. Dynamic stall modeling for wind turbines. Master's thesis, Delft University of Technology, 2018.

J. G. Leishman and T. S. Beddoes. A semiempirical model for dynamic stall. Journal of the American Helicopter Society, 34(3):3–17, 1989. ISSN 2161-6027. doi: doi: 10.4050/JAHS.34.3.3. URL https://www.ingentaconnect.com/content/ahs/jahs/1989/00000034/00000003/art00001.

J. Gordon Leishman. Challenges in modelling the unsteady aerodynamics of wind turbines. Wind Energy, 5(2-3):85–132, 2002. doi: https://doi.org/10.1002/we.62. URL https://onlinelibrary.wiley.com/doi/abs/10.1002/we.62.

Xiong Liu, Cheng Lu, Shi Liang, Ajit Godbole, and Yan Chen. Vibration-induced aerodynamic loads on large horizontal axis wind turbine blades. Applied Energy, 185:1109–1119, 2017. ISSN 0306-2619. doi: https://doi.org/10.1016/j.apenergy.2015.11.080. URL https://www.sciencedirect.com/science/article/pii/S0306261915015305. Clean, Efficient and Affordable Energy for a Sustainable Future.

S. Marelli, C. Lamas, K. Konakli, C. Mylonas, P. Wiederkehr, and B. Sudret. UQLab user manual – Sensitivity analysis. Technical report, Chair of Risk, Safety and Uncertainty Quantification, ETH Zurich, Switzerland, 2022a. Report UQLab-V2.0-106.

S. Marelli, N. Lüthen, and B. Sudret. UQLab user manual – Polynomial chaos expansions. Technical report, Chair of Risk, Safety and Uncertainty Quantification, ETH Zurich, Switzerland, 2022b. Report UQLab-V2.0-104.

Stefano Marelli and Bruno Sudret. UQLab: A Framework for Uncertainty Quantification in Matlab, pages 2554–2563. University of Liverpool, 2014. doi: 10.1061/9780784413609.257. URL https://ascelibrary.org/doi/abs/10.1061/9780784413609.257.

K. W. Mcalister, Olivier Lambert, and D. Petot. Application of the onera model of dynamic stall. In NASA technical report, 1984. URL https://ntrs.nasa.gov/citations/19850004554.

W.J. McCroskey. The Phenomenon of Dynamic Stall. Defense Technical Information Center, 1981. URL https://books.google.nl/books?id=I-JCAQAAIAAJ.

Craig Meskell and Alberto Pellegrino. Vortex shedding lock-in due to pitching oscillation of a wind turbine blade section at high angles of attack. International Journal of Aerospace Engineering, 95:6919505, 2019. doi: https://doi.org/10.1155/2019/6919505. URL https://downloads.hindawi.com/journals/ijae/2019/6919505.pdf.

Karen Mulleners and M. Raffel. The onset of dynamic stall revisited. Experiments in Fluids, Vol. 52:779–793, 03 2011. doi: 10.1007/s00348-011-1118-y.

Terukazu Ota, Yasunori Okamoto, and Hiroyuki Yoshikawa. A Correction Formula for Wall Effects on Unsteady Forces of Two-Dimensional Bluff Bodies. Journal of Fluids Engineering, 116(3):414–418, 09 1994. ISSN 0098-2202. doi: 10.1115/1.2910292. URL https://doi.org/10.1115/1.2910292.

Ceyhan Ozlem, Pires Oscar, and Munduate Xabier. AVATAR HIGH REYNOLDS NUMBER TESTS ON AIRFOIL DU00-W-212, April 2017. URL https://doi.org/10.5281/zenodo.439827.

Alberto Pellegrino and Craig Meskell. Vortex shedding from a wind turbine blade section at high angles of attack. Journal of Wind Engineering and Industrial Aerodynamics, 121: 131–137, 2013. ISSN 0167-6105. doi: https://doi.org/10.1016/j.jweia.2013.08.002. URL https://www.sciencedirect.com/science/article/pii/S016761051300175X.

David A. Peters. Toward a unified lift model for use in rotor blade stability analyses. Journal of the American Helicopter Society, 30(3):32–42, 1985. ISSN 2161-6027. doi: doi: 10.4050/JAHS.30.3.32. URL https://www.ingentaconnect.com/content/ahs/jahs/1985/00000030/00000003/art00004.

Tristan Revaz and Fernando Porté-Agel. Large-eddy simulation of wind turbine flows: A new evaluation of actuator disk models. Energies, 14(13), 2021. ISSN 1996-1073. doi: 10.3390/en14133745. URL https://www.mdpi.com/1996-1073/14/13/3745.

V. Riziotis, S. Voutsinas, Evangelos Politis, and P.K. Chaviaropoulos. Stability analysis of parked wind turbine blades using a vortex model. In Science of making torque from the wind, 06 2010. URL https://www.researchgate.net/publication/280527933_Stability_analysis_of_parked_wind_turbine_blades_using_a_vortex_model.

B. Sanderse, V. V. Dighe, K. Boorsma, and G. Schepers. Efficient bayesian calibration of aerodynamic wind turbine models using surrogate modeling. Wind Energy Science, 7 (2):759–781, 2022. doi: 10.5194/wes-7-759-2022. URL https://wes.copernicus.org/articles/7/759/2022/.

J. Schepers. An engineering model for yawed conditions, developed on basis of wind tunnel measurements. In 37th Aerospace Sciences Meeting and Exhibit, 1999. doi: 10.2514/6.1999-39. URL https://arc.aiaa.org/doi/abs/10.2514/6.1999-39.

J.G. Schepers. Engineering models in wind energy aerodynamics. Development, implementation and analysis using dedicated aerodynamic measurements. PhD thesis, Delft University of Technology, 2012.

Scott Schreck. Spectral content and spatial scales in unsteady rotationally augmented flow fields. In Journal of Physics Conference Series, volume 75 of Journal of Physics Conference Series, page 012024, July 2007. doi: 10.1088/1742-6596/75/1/012024.

Esmatullah Maiwand Sharify, Hiroki Saito, Hiromoto Harasawa, Shun Takahashi, and Norio Arai. Experimental investigation of flow past a confined bluff body: Effects of body shape, blockage ratio and reynolds number. JSEM, 13:7–12, 2013. URL https://www.jstage.jst.go.jp/article/jjsem/13/Special_Issue/13_s7/_pdf.

Witold Skrzypiński, Mac Gaunaa, Niels Sørensen, Frederik Zahle, and Joachim Heinz. Vortex-induced vibrations of a du96-w-180 airfoil at 90° angle of attack. Wind Energy, 17, 10 2014. doi: 10.1002/we.1647.

M Stettner, M J Reijerkerk, A Lünenschloß, V Riziotis, A Croce, L Sartori, R Riva, and J M Peeringa. Stall-induced vibrations of the AVATAR rotor blade. Journal of Physics: Conference Series, 753:042019, sep 2016. doi: 10.1088/1742-6596/753/4/042019. URL https://doi.org/10.1088/1742-6596/753/4/042019.

C T Tran and D Petot. Semi-empirical model for the dynamic stall of airfoils in view to the application to the calculation of responses of a helicopter blade in forward flight. Vertica, 5(1):35–52, 1980. ISSN 03605450.

Khiem Truong. Conference proceedings: A 2-d dynamic stall model based on a hopf bifurcation. In 19th European rotorcraft forum, 09 1993a.

V. K. Truong. A 2-d dynamic stall model based on a hopf bifurcation. In In 19th European Rotorcraft Forum, 1993b.

Axelle Viré, Adriaan Derksen, Mikko Folkersma, and Kumayl Sarwar. Two-dimensional numerical simulations of vortex-induced vibrations for a cylinder in conditions representative of wind turbine towers. Wind Energy Science, 5(2):793–806, June 2020. ISSN 2366-7443. doi: 10.5194/wes-5-793-2020.

P.-R. Wagner, J. Nagel, S. Marelli, and B. Sudret. UQLab user manual – Bayesian inversion for model calibration and validation. Technical report, Chair of Risk, Safety and Uncertainty Quantification, ETH Zurich,Switzerland, 2022a. Report UQLab-V2.0-113.

P.-R. Wagner, J. Nagel, S. Marelli, and B. Sudret. UQLab user manual – Bayesian inversion for model calibration and validation. Technical report, Chair of Risk, Safety and Uncertainty Quantification, ETH Zurich, Switzerland, 2022b. Report UQLab-V2.0-113.

K. Wang, V. A. Riziotis, and S. G. Voutsinas. Aeroelastic stability of idling wind turbines. Wind Energy Science, 2(2):415–437, 2017. doi: 10.5194/wes-2-415-2017. URL https://wes.copernicus.org/articles/2/415/2017/.

Xikun Wang, Jiaqi Chen, Bo Zhou, Yajie Li, and Qingjiang Xiang. Experimental investigation of flow past a confined bluff body: Effects of body shape, blockage ratio and reynolds number. Ocean Engineering, 220:108412, 2021. ISSN 0029-8018. doi: https://doi.org/10.1016/j.oceaneng.2020.108412. URL https://www.sciencedirect.com/science/article/pii/S0029801820313196.

Guanqun Xu, Wei Yu, Andrea Sciacchitano, and Carlos Ferreira. An experimental study of the unsteady aerodynamics of a du91-w2-250 airfoil at large angles of attack. Wind Energy, 2023. doi: underreview.

W. W. H. YEUNG. On pressure invariance, wake width and drag prediction of a bluff body in confined flow. Journal of Fluid Mechanics, 622:321–344, 2009. doi: 10.1017/S0022112008005247.

Steven Yon and Joseph Katz. Study of the unsteady flow features on a stalled wing. AIAA Journal, 36:305–312, 01 1998. doi: 10.2514/3.13821.

Mohamed Zakaria, Moustafa Ibrahim, Saad Ragab, and Muhammad R. Hajj. A computational study of vortex shedding from a naca-0012 airfoil at high angles of attack. Int. J. Aerodynamics, 6:1, 01 2018. doi: 10.1504/IJAD.2018.10010814.

Tong Zhou, Earl Dowell, and Shun shan Feng. Computational investigation of wind tunnel wall effects on buffeting flow and lock-in for an airfoil at high angle of attack. Aerospace Science and Technology, 95:105492, 2019a. ISSN 1270-9638. doi: https://doi.org/10.1016/j.ast.2019.105492. URL https://www.sciencedirect.com/science/article/pii/S1270963819313902.

Yicheng Zhou, Zhenzhou Lu, Kai Cheng, and Yan Shi. An expanded sparse bayesian learning method for polynomial chaos expansion. Mechanical Systems and Signal Processing, 128:153–171, 2019b. ISSN 0888-3270. doi: https://doi.org/10.1016/j.ymssp.2019.03.032. URL https://www.sciencedirect.com/science/article/pii/S0888327019302092.